

**Limit on the  $B_s^0\bar{B}_s^0$  Oscillation Frequency from  $p\bar{p}$  Collision Data at**

$$\sqrt{s} = 1.8 \text{ TeV}$$

**A Dissertation**

**Presented to**

**The Faculty of the Graduate School of Arts and Sciences**

**Brandeis University**

**Department of Physics**

**Craig Blocker, Advisor**

**In Partial Fulfillment  
of the Requirements for the Degree  
Doctor of Philosophy**

**by**

**Hongquan Niu**

**February 2003**

UMI Number: 3073892

**UMI<sup>®</sup>**

---

UMI Microform 3073892

Copyright 2003 by ProQuest Information and Learning Company.

All rights reserved. This microform edition is protected against  
unauthorized copying under Title 17, United States Code.

---

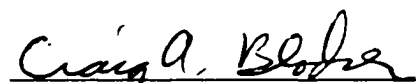
ProQuest Information and Learning Company  
300 North Zeeb Road  
P.O. Box 1346  
Ann Arbor, MI 48106-1346

This dissertation, directed and approved by Hongquan Niu's Committee, has been accepted and approved by the Graduate Faculty of Brandeis University in partial fulfillment of the requirements for the Degree of:

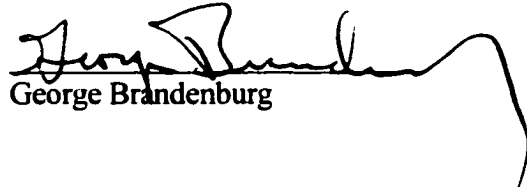
**DOCTOR OF PHILOSOPHY**

  
Dean, Arts and Sciences

**Dissertation Committee**

  
Craig Blocker, Chair

  
Lawrence Kirsch

  
George Brandenburg

## **DEDICATION**

**This thesis is dedicated to my wife Huabin Wang and my daughter Wenny Niu.**

## **ACKNOWLEDGMENTS**

I would like to thank my advisor Craig Blocker for his guidance and support. I'm also very grateful to Petar Maksimović for his generous help and guidance throughout my thesis analysis at CDF, Fermilab.

I am deeply appreciative of the support given by Owen Long, Kevin Pitts and Philippe Canal.

Many thanks to Mike Kirk for his help and being a great classmate, office mate and colleague.

Finally, I would like to thank all of the people who make Fermilab such a unique and nice environment for the graduate students doing their research.

## ABSTRACT

Limit on the  $B_s^0 \bar{B}_s^0$  Oscillation Frequency from  $p\bar{p}$  Collision Data at  $\sqrt{s} = 1.8$  TeV

A dissertation presented to the Faculty of the  
Graduate School of Arts and Sciences of Brandeis  
University, Waltham, Massachusetts

by Hongquan Niu

This thesis presents a limit on the  $B_s^0 \bar{B}_s^0$  oscillation frequency from  $p\bar{p}$  collision data at  $\sqrt{s} = 1.8$  TeV at CDF. The data sample used is the inclusive electron and muon trigger data of approximately  $90 \text{ pb}^{-1}$  collected during the 1993-1995 run. The  $B_s^0$  meson is reconstructed as  $B_s^0 \rightarrow \nu \ell D_s$ , where  $D_s \rightarrow \phi \pi$  or  $K^{*0} K$ . The initial flavor of the  $B_s^0$  meson is determined from the decay products of the other  $b$ -hadron in the event, using opposite-side jet charge and soft lepton tagging methods. When combined with CDF previous measurements, a lower limit of  $\Delta m_s > 6.3 \text{ ps}^{-1}$  is determined.

# Contents

<b>1</b>	<b>Introduction</b>	<b>1</b>
<b>2</b>	<b>Theoretical Background</b>	<b>6</b>
2.1	Leptons, Quarks and the Standard Model . . . . .	6
2.1.1	Leptons and Quarks . . . . .	6
2.1.2	History of CKM matrix and the Charged Weak Interaction . . . . .	8
2.1.3	The CKM Matrix . . . . .	11
2.2	$B^0$ Mixing in the Standard Model . . . . .	14
<b>3</b>	<b>The Experimental Apparatus</b>	<b>21</b>
3.1	The Accelerator . . . . .	21
3.2	The CDF detector . . . . .	24
3.2.1	The Overview . . . . .	24
3.2.2	Tracking . . . . .	29
3.2.3	The Central Calorimeters . . . . .	38

3.2.4	The Central Muon Detectors . . . . .	39
3.2.5	Triggers . . . . .	41
<b>4</b>	<b>Data Selection</b>	<b>45</b>
4.1	Data Sample . . . . .	45
4.2	Reconstruction of $B_s^0 \rightarrow \nu \ell D_s$ Decays . . . . .	47
4.2.1	Selection Cuts For $B_s^0 \rightarrow \ell D_s, D_s \rightarrow \phi \pi$ Mode . . . . .	48
4.2.2	Selection Cuts For $B_s^0 \rightarrow \ell D_s, D_s \rightarrow K^{*0} K$ Mode . . . . .	49
4.2.3	$D_s$ Mass Fit Result . . . . .	50
4.2.4	Estimating the Contribution of $D^-$ to the $D_s \rightarrow K^{*0} K$ Decay mode . . . . .	52
<b>5</b>	<b>Flavor Tagging</b>	<b>56</b>
5.1	Introduction . . . . .	56
5.1.1	Dilution . . . . .	57
5.1.2	Dilution Calibration . . . . .	59
5.1.3	The Raw Dilution . . . . .	60
5.2	The Secondary Vertex . . . . .	62
5.2.1	The Primary Vertex . . . . .	62
5.2.2	Track-Based Jets . . . . .	63
5.2.3	Secondary Vertex Finding . . . . .	63
5.3	Opposite Side Jet Charge Flavor Tagging . . . . .	69

5.3.1	$b\bar{b}$ Production Topologies . . . . .	70
5.3.2	Opposite Jet Secondary Vertex Tagged(JST) and JQT . . . . .	72
5.3.3	Jet Charge Distributions and Dilutions . . . . .	73
5.3.4	Testing of JQT . . . . .	78
5.4	Opposite Side Soft Lepton Flavor Tagging . . . . .	80
5.4.1	Conversion Soft Electron Removal . . . . .	80
5.4.2	SLT Selection Criteria and Parameterization . . . . .	81
5.5	The Dilution Normalization $N_D$ . . . . .	85
<b>6</b>	<b>The Fitting Method</b>	<b>86</b>
6.1	K-factor Distribution . . . . .	86
6.2	Fitting Function . . . . .	92
6.2.1	Lifetime Probability Density Function . . . . .	92
6.2.2	Mixing P.D.F and the Unbinned Likelihood Function . . . . .	94
6.3	Test of the Fitters . . . . .	97
<b>7</b>	<b>Determination of the Lower Limit on <math>\Delta m_s</math></b>	<b>101</b>
7.1	$B_s^0$ Lifetime Fit . . . . .	101
7.1.1	$\phi\pi$ Mode Lifetime Fit . . . . .	102
7.1.2	$K^{*0}K$ Mode Lifetime Fit . . . . .	103
7.2	$B_s^0$ Amplitude Fit . . . . .	106
7.2.1	The Sensitivity . . . . .	106

7.2.2	Amplitude Fit Result of $\phi\pi$ and $K^{*0}K$ . . . . .	109
7.3	The Systematic Errors . . . . .	111
<b>8</b>	<b>Conclusion</b>	<b>117</b>
	<b>Appendix A Combining Errors</b>	<b>119</b>
	<b>Bibliography</b>	<b>122</b>

# List of Figures

1.1	$B_s^0$ mixing box diagram. . . . .	1
2.1	Box diagrams for $K^0 \rightarrow \mu^+ \mu^-$ decay. . . . .	9
2.2	Charged weak interaction . . . . .	12
2.3	The Bjorken Triangle . . . . .	14
2.4	$B_s^0$ mixing box diagrams. . . . .	15
3.1	A schematic diagram of the accelerator at Fermilab. The CDF experiment is also shown. . . . .	23
3.2	An isometric view of the CDF detector. . . . .	25
3.3	Quarter-view of the CDF detector. The detector has forward and backward symmetry around the interaction point as well as azimuthal symmetry. The interaction point is at the lower left of the figure. The z axis points to the east, the y axis points up, and the x axis points into the page. . . . .	26

3.4	Diagram of the 5 tracking parameters from a side-view and end-view of the CTC which describe a charged particle traveling in a magnetic field following a helical trajectory. . . . .	29
3.5	The schematic drawing of one of the SVX barrel. . . . .	31
3.6	The schematic drawing of a SVX ladder . . . . .	32
3.7	Diagram of the Central Tracking Chamber (CTC) end-plate showing the location of the wire planes. . . . .	35
3.8	The wire positions for an axial super-layer cell of CTC . . . . .	36
3.9	A CEM wedge. . . . .	40
4.1	A general diagram of the decay mode $B \rightarrow \nu \ell D$ . Here $B$ can be $B_s^0$ and $D$ be $D_s$ , where $D_s \rightarrow \phi \pi$ , $\phi \rightarrow KK$ or $D_s \rightarrow K^{*0} K$ , $K^{*0} \rightarrow K \pi$ . The flavor tag is obtained from the decay on the opposite side; if the decay of the opposite side $b$ -hadron is semileptonic, and the lepton is found, its charge is used as the flavor tag. Otherwise the charge of the $b$ -jet (weighted by transverse momentum) is used. . . . .	46

4.2	The $KK\pi$ invariant mass distribution for the $\ell^+D_s^-$ decay channel, where $D_s^- \rightarrow \phi\pi$ . We fit the mass distribution with a single Gaussian that describes the $D_s$ signal, and with an exponential that describes the shape of the combinatorial background. The fit is superimposed on top of the data points. The dashed histogram represents events where lepton and $D_s$ have the same charge. . . . .	51
4.3	The $KK\pi$ invariant mass distribution for the $\ell^+D_s^-$ decay channel, where $D_s^- \rightarrow K^{*0}K^-$ . We fit the mass distribution with a single Gaussian that describes the $D_s$ signal, the $M_{B^0}(m)$ function that describes the $B^0$ reflection and an exponential that describes the shape of the combinatorial background. The scaled $B^0$ reflection histogram with the fitted function (the horizontal scale is enlarged) and the single Gaussian are also in the plot. . . . .	55
5.1	The plot on the top is the cluster and true $P_t$ distributions for the Run 1b electron Monte Carlo data from Reference [21]. The plot on the bottom is the $P_t$ distribution from our Run 1b electron Monte Carlo data. . . . .	61

5.2	The ordering hierarchy for tracks to be considered in vertexing from Reference [21]. Tracks with high $ d_0/\sigma_{d_0} $ , $P_t$ , and a larger number of good SVX hits are considered first. Tracks in the same class are sorted by the Secondary Sorting variable. . . . .	66
5.3	Representative Feynman diagrams for the three major $b\bar{b}$ production mechanisms. Note that not all possible diagrams are shown. . . . .	71
5.4	Jet charge and $D(raw)$ vs $ Q_{jet} $ distributions for JQT and JST tagged events in the $e$ trigger data from Reference [21]. . . . .	74
5.5	Jet charge and $D(raw)$ vs $ Q_{jet} $ distributions for JQT and JST tagged events in the $\mu$ trigger data from Reference [21] . . . . .	75
5.6	The raw dilution $D(raw)$ , flavor tagging $\epsilon$ and $\epsilon D(raw)^2$ in bins of $ Q_{jet} $ for JQT and JST $e$ trigger events from Reference [21]. . . . .	76
5.7	The raw dilution $D(raw)$ , flavor tagging $\epsilon$ and $\epsilon D(raw)^2$ in bins of $ Q_{jet} $ for JQT and JST $\mu$ trigger events from Reference [21]. . . . .	77
5.8	Testing of Owen's JQT tagging . . . . .	79

5.9	The soft lepton raw dilution as a function of the soft lepton $P_\ell(\text{rel})$ from the analysis of Reference [21]. The data are divided into the 5 soft lepton types for the $e$ and $\mu$ triggers. The negative $P_\ell(\text{rel})$ is for events where the soft lepton is isolated and does not have a $P_\ell(\text{rel})$ measurement. The solid line is used in the event-by-event dilution prediction. The dashed lines are used for the systematic studies. . . .	83
6.1	Monte Carlo generated $K$ -factor distribution for $\phi\pi$ mode, where $K = \frac{p_T(\ell^+ D_s^-)}{p_T(B_s^0)}$ . . . . .	88
6.2	Monte Carlo generated $K$ -factor distribution for $K^{*0}K$ mode. . . . .	89
6.3	Monte Carlo generated $L_{xy}$ pull for $\phi\pi$ mode with a single Gaussian fit superimposed. . . . .	90
6.4	Monte Carlo generated $L_{xy}$ pull for $K^{*0}K$ mode. . . . .	91
6.5	Pull distribution of $B_s^0$ lifetime from a simple toy Monte Carlo. . . . .	97
6.6	Toy Monte Carlo amplitude fit with input $\Delta m_s = 9\text{ps}^{-1}$ , resolution = 0.0012 cm, 10000 events. The dashed line corresponds to $A + 1.645\sigma_A$ with statistical uncertainties. The values of $\Delta m_s$ for which the dashed line is less than one are excluded at 95% confidence level. We can see there is mixing at $\Delta m_s = 9\text{ps}^{-1}$ . . . . .	99

6.7	Toy Monte Carlo amplitude fit with input $\Delta m_s = 20\text{ps}^{-1}$ , resolution = 0.0078 cm, 769 events with the appropriate tagging efficiency and dilution. This is trying to simulate the CDF $\ell D_s$ channel data. . . . .	100
7.1	$B_s^0$ $\phi\pi$ mode lifetime fit result with signal and background overlaid. The shaded area is the background and the lower curve is the signal. The fit yields $B_s^0$ lifetime $474_{-45}^{+50}$ $\mu\text{m}$ . . . . .	104
7.2	$B_s^0$ lifetime fit result for $K^{*0}K$ mode with signal and background overlaid. The shaded area is the background and the lower curve is the signal. The fit yields $B_s^0$ lifetime of $397_{-62}^{+65}$ $\mu\text{m}$ . . . . .	107
7.3	Estimate of the lower limit for $\Delta m_s$ from study of $\ell D_s$ channel at 95% confidence level. The dashed line is from the theoretical estimate of our data. The solid line is from the measurement of the amplitude scan.	108
7.4	The combined theoretical estimate of the sensitivity of CDF current measurement and this analysis. The dot-dashed line is our estimated sensitivity. The dashed line is the estimated sensitivity of the current CDF measurement[35]. The solid line is the combined sensitivity estimate of these two measurements. The combined sensitivity is increased by $0.2\text{ps}^{-1}$ . . . . .	110

7.5	<p><math>\phi\pi</math> mode and <math>K^{*0}K</math> mode combined result of the amplitude scan. The dots with <math>1\sigma</math> error bars are fitted amplitudes with errors. The dashed line corresponds to <math>A + 1.645\sigma_A</math> with statistical uncertainties. The solid line is for statistical + systematic uncertainties. . . . .</p>	112
7.6	<p>The CDF current result of <math>B_s^0</math> mixing amplitude scan. The values of <math>\Delta m_s</math> for which the solid line is less than one are excluded at 95% confidence level. The current CDF limit on <math>\Delta m_s</math> is <math>5.8 \text{ ps}^{-1}</math>. . . . .</p>	113
7.7	<p>The combination of current CDF amplitude scan and ours assuming no correlation between the two analysis when combining the systematic uncertainties. The CDF preliminary new limit would be <math>6.3 \text{ ps}^{-1}</math>. . .</p>	114

# List of Tables

2.1	Various parameters and values in equation 2.26 . . . . .	20
3.1	Some features of CTC. . . . .	34
5.1	Track quality criteria for track clustering from Reference [21]. The CTC exit radius is the radial position at which the track crosses the plane that defines the edge of the CTC in $z$ . . . . .	64
5.2	Jet charge flavor tag $\sum_i \epsilon_i D_{raw}^2$ where the sum is in bins of $ Q_{jet} $ from Reference [21]. . . . .	78
5.3	Tight and loose cuts used in conversion finding from Reference [21]. . . . .	81
5.4	Soft lepton flavor tag $\sum_i \epsilon_i D_i^2(raw)$ where the sum is in bins of soft lepton $P_i(rel)$ from Reference [21]. . . . .	84
5.5	Values for $N_D$ factors, where $\Delta m_d$ has been fixed to the world average ( $0.47 \text{ ps}^{-1}$ ) from Reference [21]. The first error is statistical, the second is systematic. Those numbers are used for our dilution calibration. . . . .	84

7.1	$\phi\pi$ mode lifetime fit result with $B_s^0$ lifetime fixed to world average. . .	102
7.2	$\phi\pi$ mode lifetime fit result. . . . .	103
7.3	$K^{*0}K$ mode lifetime fit result with $B_s^0$ lifetime fixed to world average. . .	106
7.4	$K^{*0}K$ mode lifetime fit result. . . . .	107
7.5	$\phi\pi$ and $K^{*0}K$ modes input parameters for the later amplitude fit . . .	111

# Chapter 1

## Introduction

The phenomenon of mixing, in which a neutral meson transforms into its anti-particle via a flavor-changing second-order weak diagram (Figure 1.1), provides information on elements of the Cabibbo-Kobayashi-Maskawa matrix[1][2].

The oscillation frequency of neutral meson mixing is proportional to the mass difference between its mass eigenstates. For example, in the case of  $B_d^0 \bar{B}_d^0$  mixing, the

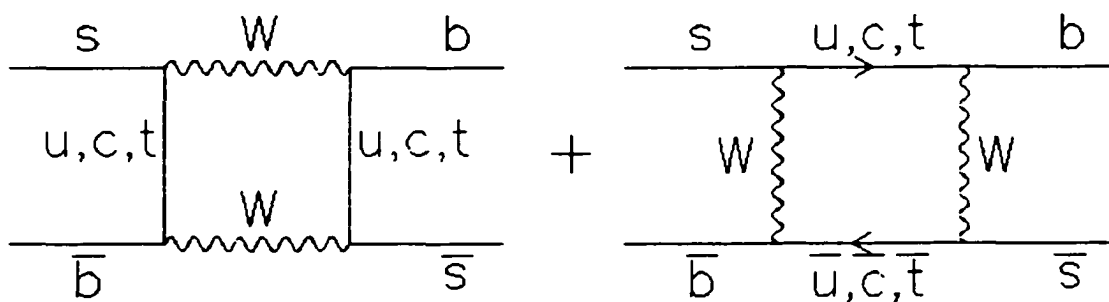


Figure 1.1:  $B_s^0$  mixing box diagram.

oscillation frequency is  $\Delta m_d$ , and these flavor oscillations have been experimentally observed by the LEP, SLD, and CDF experiments.

In the second-order weak ‘box diagram’, the intermediate states contain all three ‘up-type’ quarks ( $u$ ,  $c$  and  $t$ ), but the diagram with the top quark dominates because of its mass. For this reason,  $\Delta m_{B_d^0} \sim |V_{td}V_{tb}^*|^2$ , and, analogously,  $\Delta m_{B_s^0} \sim |V_{ts}V_{tb}^*|^2$ . Therefore, by measuring  $\Delta m_{d,s}$ , we can obtain information on the magnitudes of  $V_{td}$  and  $V_{ts}$ . However, given that the proportionality constant depends directly on QCD factors (the  $B$ -meson decay constant and the bag factor), which have significant uncertainties (20%), a more useful quantity is the ratio  $\Delta m_s/\Delta m_d$ , since it measures  $|V_{ts}/V_{td}|$  with smaller hadronic uncertainties.

Neutral  $B$  mesons are produced by the process  $p\bar{p} \rightarrow b\bar{b} \rightarrow B\bar{B} + X$  where  $B(\bar{B})$  refers to all  $\bar{b}(b)$  flavored hadrons. The flavor states  $|B^0\rangle$  (standing for  $B_s^0$  or  $B_d^0$ ) and  $|\bar{B}^0\rangle$  mix through the weak interactions to form “Light” and “Heavy” mass-eigenstates  $B_L$  and  $B_H$ [3]:

$$|B_L\rangle = p|B^0\rangle + q|\bar{B}^0\rangle \quad (1.1)$$

$$|B_H\rangle = p|B^0\rangle - q|\bar{B}^0\rangle \quad (1.2)$$

The parameters  $p$  and  $q$  are the coefficients which relate the  $B^0$  and  $\bar{B}^0$  to the mass-eigenstates  $B_H$  and  $B_L$ . The Standard Model predicts[4]

$$\left|\frac{q}{p}\right| \approx 1. \quad (1.3)$$

From equations 1.1-1.3, we can get the time evolution of initially unmixed  $B^0$  and  $\bar{B}^0$  as

$$|B^0(t)\rangle = c(t)|B^0\rangle + i\frac{q}{p}s(t)|\bar{B}^0\rangle \quad (1.4)$$

$$|\bar{B}^0(t)\rangle = c(t)|\bar{B}^0\rangle + i\frac{p}{q}s(t)|B^0\rangle \quad (1.5)$$

where

$$c(t) = e^{-i\frac{m_L+m_H}{2}t} e^{-\frac{\Gamma t}{2}} \cos \frac{\Delta m t}{2} \quad (1.6)$$

$$s(t) = e^{-i\frac{m_L+m_H}{2}t} e^{-\frac{\Gamma t}{2}} \sin \frac{\Delta m t}{2} \quad (1.7)$$

Here,  $\Delta m = m_H - m_L$  is the mass difference for the two mass eigenstates. We have assumed that the  $B_L$  and  $B_H$  decay widths are the same, that is,  $\Gamma_L = \Gamma_H = \Gamma$ . From equation (2.20), we see that if the initial state is a pure  $|B^0\rangle$  state, then at time  $t$ , the probability to find it in the same state  $|B^0\rangle$  (denoted as ‘unmixed’ or ‘right sign’) is  $|c(t)|^2$ . The probability to get the state  $|\bar{B}^0\rangle$  (denoted as ‘mixed’ or ‘wrong

sign') is  $|s(t)|^2$ . We get an analogous result for an initially pure  $|\bar{B}^0\rangle$  state. The time-dependent probability to observe a decay of a  $B$  meson at proper time  $t$  which is either 'right-sign' (rs) or 'wrong-sign' (ws) is

$$P^{rs,ws}(t) = \frac{1}{2\tau} e^{-\frac{t}{\tau}} (1 \pm \cos \Delta mt) \quad (1.8)$$

We also need to determine the flavor of  $B_s^0$  both at production and at decay. At decay, the flavor is given by the charge of the lepton. To determine the flavor of  $B_s^0$  at production, we use 'flavor tagging' algorithms. In this analysis we make use of 'opposite-side flavor tagging' (OST) based on the facts that in the  $p\bar{p}$  collisions the  $b$ -quarks are produced in pairs and that identifying the decay flavor of the  $b$ -hadron on the opposite side identifies the *production* flavor of the  $B_s^0$  meson we have reconstructed as  $\ell D_s$ . Since the tagging is not pure, there is a mistag rate  $W$  associated with the determination of the initial flavor of the  $b$ -quark. It is more convenient to express the mistagging via a quantity called dilution, defined as  $D = 1 - 2W$ . Using  $D$ , the probability distribution function (p.d.f.) is now

$$P^{rs,ws}(t) = \frac{1}{2\tau} e^{-\frac{t}{\tau}} (1 \pm D \cos \Delta mt) \quad (1.9)$$

Currently  $\Delta m_d$  is well known[5] (with the uncertainty on the world average of about  $0.008 \text{ ps}^{-1}$ ), while the  $B_s^0 \bar{B}_s^0$  oscillations have not been observed yet and thus

only an upper limit on  $\Delta m_s$  exists. The current CDF limit is  $\Delta m_s > 5.8 \text{ ps}^{-1}$  [6]. As of the Fall of 2002, the world average is  $\Delta m_s > 13.1 \text{ ps}^{-1}$ [5].

In this analysis, we study the  $B_s^0$  oscillations using a sample of  $B_s \rightarrow \ell \nu D_s$  decays followed by  $D_s \rightarrow \phi \pi$  or  $D_s \rightarrow K^{*0} K$ . We use two types of the opposite side tagging: soft lepton tagging (SLT) and jet charge tagging (JQT), which are then combined in the final result. No lower limit is set in this analysis, but it is combined with other CDF analyses.

# Chapter 2

## Theoretical Background

### 2.1 Leptons, Quarks and the Standard Model

#### 2.1.1 Leptons and Quarks

Presently, scientists believe that our universe's elementary components are point-like particles, called quarks ( $q$ ) and leptons ( $\ell$ ), and four types of force-carrying bosons (photon, gluons, Z, W). Leptons and quarks come in three generations of pair of particles as follows[7]:

1	2	3	$Q(e)$
$\begin{pmatrix} u \\ d \end{pmatrix}$	$\begin{pmatrix} c \\ s \end{pmatrix}$	$\begin{pmatrix} t \\ b \end{pmatrix}$	$\frac{2}{3}$
$\begin{pmatrix} \nu_e \\ e \end{pmatrix}$	$\begin{pmatrix} \nu_\mu \\ \mu \end{pmatrix}$	$\begin{pmatrix} \nu_\tau \\ \tau \end{pmatrix}$	$0$
			$-1$

where u(up), d(down), c(charm), s(strange), t(top) and b(bottom) stand for different flavor of quarks. Each flavor has three possible values of a quantum number known as color (having nothing to do with actual colors). All quarks and leptons have their anti-particles. Anti-quarks have anti-colors.

Three quarks form a colorless bound state, which is called baryon, while quark and anti-quark pairs form mesons, which have integral spin. Baryons and mesons are subject to strong interactions and are called hadrons. If one of the quarks in a meson is  $b$  quark, we call it a  $B$  meson. The  $B_s^0 (s\bar{b})$ ,  $\bar{B}_s^0 (\bar{s}b)$ ,  $B_d^0 (d\bar{b})$ ,  $\bar{B}_d^0 (\bar{d}b)$ ,  $B^+(u\bar{b})$  and  $B^-(\bar{u}b)$  mesons are the lowest mass B mesons. An example of a baryon containing a  $b$  quark is  $\Lambda_b^0 (udb)$ .

## 2.1.2 History of CKM matrix and the Charged Weak Interaction

Since the hadrons containing  $s$ ,  $c$ , and  $b$  quarks are not stable, there must be coupling between the quark generations. Cross-generation coupling was first introduced by Cabibbo[1] (rephrased by Gell-Mann[8] in terms of the quark model). That is, the  $u$  quark couples not to the  $d$ , but rather to the superposition  $d \cos \theta_c + s \sin \theta_c$ . In this way, the  $s \rightarrow Wu$  transition occurs. At that time, people only knew of  $u$ ,  $d$  and  $s$  quarks. So the decay rates of strange hadrons could be expressed in terms of  $\sin \theta_c$  ( $\sin \theta_c \approx 0.22$ ). This model was fairly successful, except that the  $K^0 \rightarrow \mu^+ \mu^-$  decay rate was substantially overestimated. Figure 2.1-a shows the Feynman diagram for this decay in the Cabibbo model, giving a decay rate proportional to  $\sin \theta_c \cos \theta_c$ , which is dramatically above the experimental limit.

In 1970, Glashow, Iliopoulos and Maiani [9] predicted the existence of a fourth quark, the charm quark ( $c$  quark) in order to resolve the  $K^0 \rightarrow \mu^+ \mu^-$  decay rate problem. In this model, known as the GIM mechanism, they proposed a 'quark mixing matrix' that rotates the  $d, s$  basis into the  $d', s'$  basis which coupled to the  $u$  and  $c$ .

$$\begin{pmatrix} d' \\ s' \end{pmatrix} = \begin{pmatrix} \cos \theta_c & \sin \theta_c \\ -\sin \theta_c & \cos \theta_c \end{pmatrix} \begin{pmatrix} d \\ s \end{pmatrix}$$

This model introduced a second diagram for the  $K^0 \rightarrow \mu^+ \mu^-$  decay, shown in

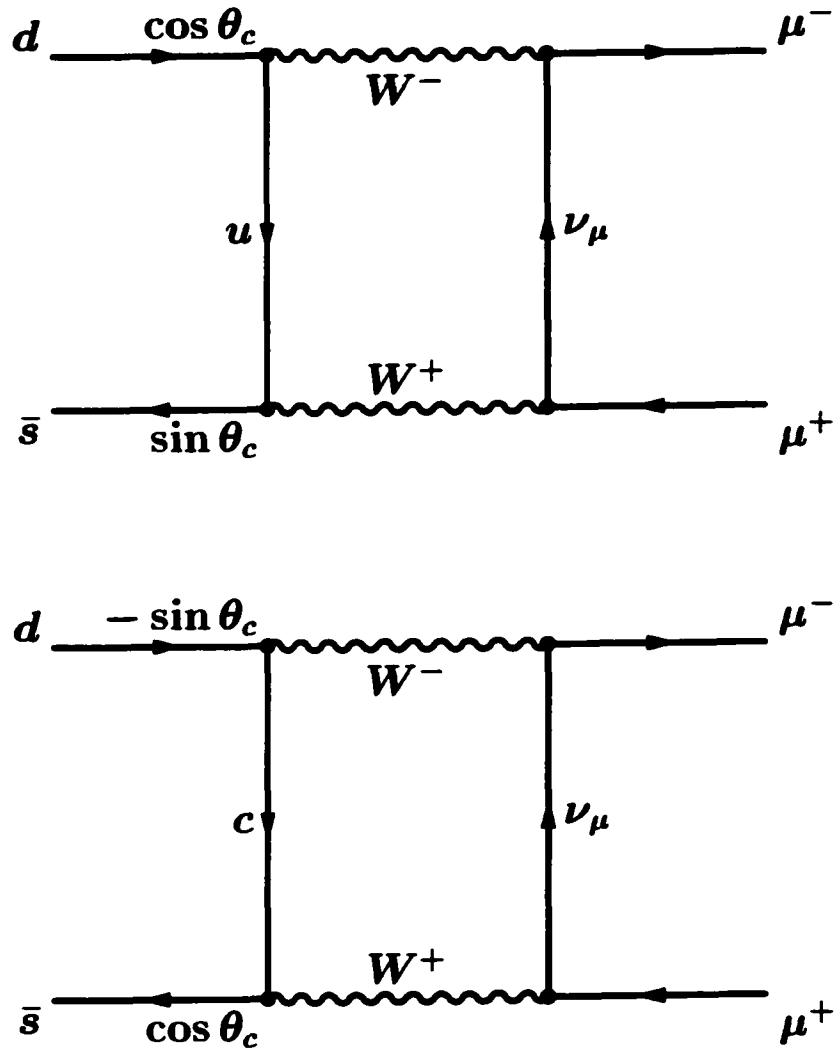


Figure 2.1: Box diagrams for  $K^0 \rightarrow \mu^+ \mu^-$  decay.

Figure 2.1-b. The vertices  $d \rightarrow c + W^-$  and  $s \rightarrow c + W^-$  carry a factor of  $-\sin \theta_c$  and  $\cos \theta_c$ , respectively. These two diagrams would cancel perfectly if  $c$  and  $u$  quarks have the exact same mass. Since their masses are not exactly the same, the new diagram suppressed the decay so that the predicted rate is consistent with the experiment results. In 1974 the  $J/\psi$  ( $c\bar{c}$ ) was discovered, giving direct evidence of the  $c$  quark.

In 1973, one year before the charm quark was discovered, Kobayashi and Maskawa[2] added a third generation of quarks, the top ( $t$ ) and bottom ( $b$ ) quarks, to the two-generation quark model and generalized the GIM mixing matrix to the more general unitary transformation from the flavor states of the down-type quarks to the weak interaction states of down-type quarks. Their motivation was to explain CP violation. They concluded that since a complex phase can always be eliminated by redefining quark phases in a  $2 \times 2$  matrix, one needed a  $3 \times 3$  matrix and thus a third generation of lepton and quarks. This hypothesis was proved by later discoveries of the  $\tau$  lepton in 1975, followed by bottom ( $b$ ) and top ( $t$ ) quarks in 1976 and 1995, respectively.

In general, the quark mass eigenstates are not the same as the weak eigenstates. They are related by the Cabibbo-Kobayashi-Maskawa matrix  $V$ . By convention[5], the three charge  $\frac{2}{3}e$  quarks( $u, c, t$ ) are unmixed, and all the mixing is expressed in terms of a  $3 \times 3$  unitary matrix  $V$  operating on the charge  $-\frac{1}{3}e$  quarks( $d, s, b$ ):

$$\begin{pmatrix} d' \\ s' \\ b' \end{pmatrix} = \begin{pmatrix} V_{ud} & V_{us} & V_{ub} \\ V_{cd} & V_{cs} & V_{cb} \\ V_{td} & V_{ts} & V_{tb} \end{pmatrix} \begin{pmatrix} d \\ s \\ b \end{pmatrix} \quad (2.1)$$

The charged weak interaction is described by the lagrangian term,

$$L_{Wq} = \frac{g}{\sqrt{2}} \bar{\psi}_{q'} (1 - \gamma_5) \gamma_\mu W_\mu^+ V_{q'q} \psi_q + \frac{g}{\sqrt{2}} \bar{\psi}_q (1 - \gamma_5) \gamma_\mu W_\mu^- V_{q'q}^\dagger \psi_{q'} \quad (2.2)$$

where  $q'$  is for  $(u, c, t)$ ,  $q$  for  $(d, s, b)$  and  $V$  is the CKM matrix. Figure 2.2 describes such interactions. The CKM matrix elements are fundamental parameters of the Standard Model and must be measured.

### 2.1.3 The CKM Matrix

A  $3 \times 3$  unitary matrix with complex elements can be written in terms of four independent real parameters, where one of these parameters is a phase factor. Wolfenstein[10] has written the CKM matrix in a form parameterized by three real numbers and one complex phase, given below, which was inspired by the 2 generation matrix introduced by Cabibbo[1] which rotates the  $d$  and  $s$  quarks.

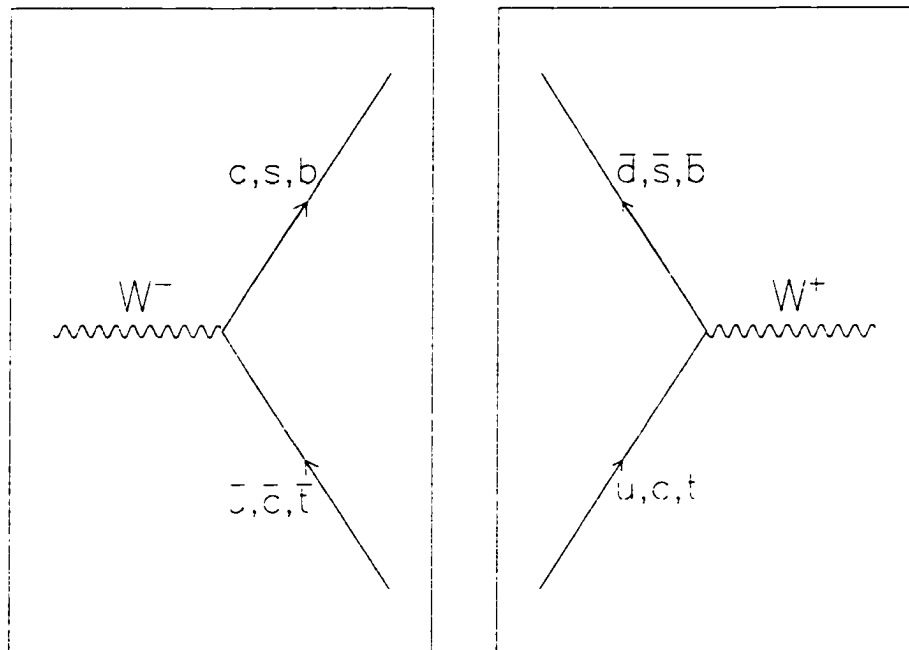


Figure 2.2: Charged weak interaction

$$V = \begin{pmatrix} 1 - \lambda^2/2 & \lambda & A\lambda^3(\rho - i\eta) \\ -\lambda & 1 - \lambda^2/2 & A\lambda^2 \\ A\lambda^3(1 - \rho - i\eta) & -A\lambda^2 & 1 \end{pmatrix} \quad (2.3)$$

Here  $\lambda$  ( $\equiv \sin \theta_c \approx 0.22$ ),  $A$ ,  $\rho$ , and  $\eta$  are real with  $A$  and  $\sqrt{\rho^2 + \eta^2}$  being of order unity. A non-zero value of  $\eta$  gives a complex phase to the CKM matrix and allows for CP violation. Physics beyond the Standard Model could also contribute to CP violation and may become evident with detailed study of the CKM matrix.

Unitarity of the CKM matrix can be represented geometrically in terms of triangles in the complex plane. One important relationship is

$$V_{ud}V_{ub}^* + V_{cd}V_{cb}^* + V_{td}V_{tb}^* = 0$$

since it contains the most poorly known entries in the CKM matrix and all three terms are roughly equal making the triangle almost equilateral.

This triangle is called the Bjorken Triangle (shown in figure 2.3 scaled by  $V_{cd}V_{cb}^*$ ). It can be shown that large angles in the Bjorken Triangle imply a large CP violation. If it is experimentally found that the Bjorken Triangle is not closed, this would also be evidence of new physics. For example, if there are more than 3 generations of leptons and quarks, the associated figure in the complex plane would be a polygon with the number of sides equal to the number of generations.

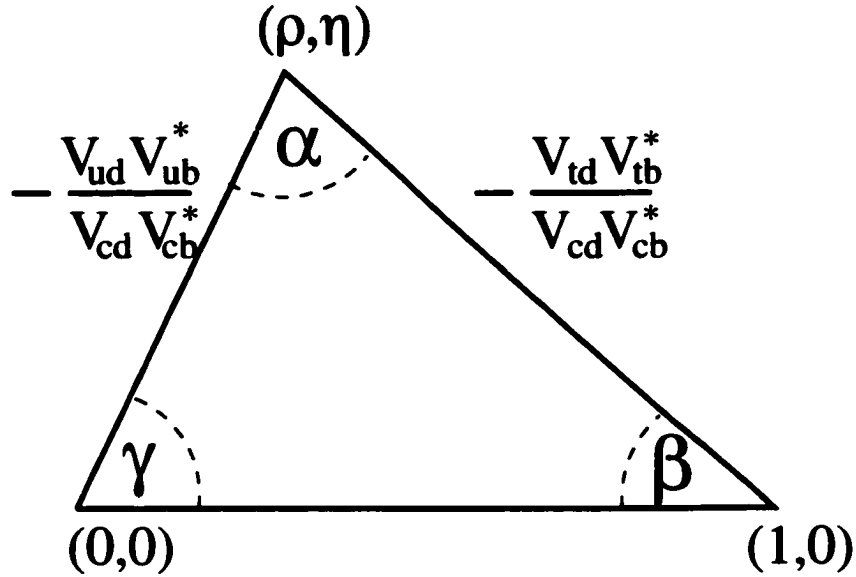


Figure 2.3: The Bjorken Triangle

## 2.2 $B^0$ Mixing in the Standard Model

The neutral  $B$  mesons  $B^0$  ( $B_s^0$  or  $B_d^0$ ) and  $\bar{B}^0$  ( $\bar{B}_s^0$  or  $\bar{B}_d^0$ ) are eigenstates of the strong interaction. However, in weak interactions, the quark flavor is not conserved, thus the  $B^0$  and  $\bar{B}^0$  mix through second order Feynman diagrams (box diagrams). Figure 2.4 shows the box diagram responsible for  $B_s^0$  mixing. The box diagrams for  $B_d^0$  mixing are similar with  $s$  quarks replaced by  $d$  quarks. Although  $u$ ,  $c$ ,  $t$  quark exchanges are all shown in the box diagram, the  $t$  quark process dominates mainly due to its heavy mass since the amplitude of this process grows with the mass of the exchanged quarks.

Since the states of definite flavor ( $B^0$  and  $\bar{B}^0$ ) are not eigenstates of the weak

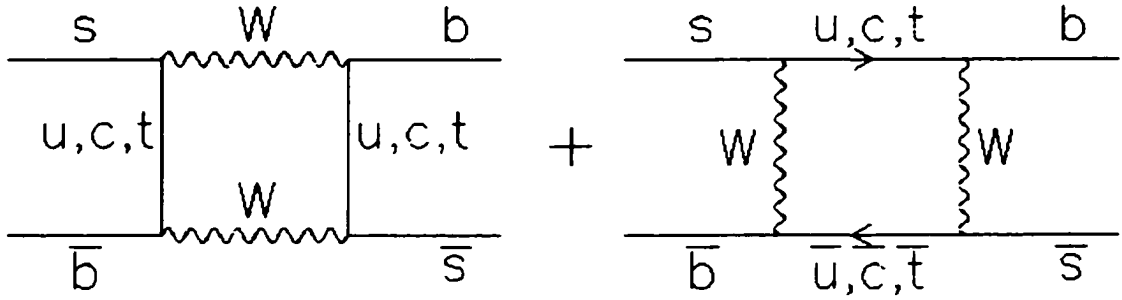


Figure 2.4:  $B_s^0$  mixing box diagrams.

interaction, in the  $|B^0\rangle$  and  $|\bar{B}^0\rangle$  basis, the weak Hamiltonian is

$$H = M - \frac{i}{2}\Gamma \quad (2.4)$$

where the  $2 \times 2$  mass and decay matrices ( $M$  and  $\Gamma$ ) are hermitian. The Hamiltonian equation is given by

$$H \begin{pmatrix} B^0 \\ \bar{B}^0 \end{pmatrix} = \begin{pmatrix} M - \frac{i}{2}\Gamma & M_{12} - \frac{i}{2}\Gamma_{12} \\ M_{12}^* - \frac{i}{2}\Gamma_{12}^* & M - \frac{i}{2}\Gamma \end{pmatrix} \begin{pmatrix} B^0 \\ \bar{B}^0 \end{pmatrix} \quad (2.5)$$

Diagonalization of the Hamiltonian yields the mass eigenstates

$$|B_L\rangle = p|B^0\rangle + q|\bar{B}^0\rangle \quad (2.6)$$

$$|B_H\rangle = p|B^0\rangle - q|\bar{B}^0\rangle \quad (2.7)$$

where

$$p = N \left( M_{12} - \frac{i}{2} \Gamma_{12} \right) = \frac{1}{\sqrt{2}} \frac{1 + \epsilon_B}{\sqrt{1 + |\epsilon_B|^2}} \quad (2.8)$$

$$q = N \sqrt{\left( M_{12} - \frac{i}{2} \Gamma_{12} \right) \left( M_{12}^* - \frac{i}{2} \Gamma_{12}^* \right)} \quad (2.9)$$

$$= \frac{1}{\sqrt{2}} \frac{1 - \epsilon_B}{\sqrt{1 + |\epsilon_B|^2}} \quad (2.10)$$

and  $N = 1/\sqrt{|p|^2 + |q|^2}$ . Note that CP is violated in the mixing if  $\epsilon_B \neq 0$ , which occurs if  $|p/q| \neq 1$ . Standard Model predicts  $|p/q| \approx 1$ .

The eigenvalues are

$$\mu_H = M - \frac{i}{2} \Gamma + Q \quad (2.11)$$

$$\mu_L = M - \frac{i}{2} \Gamma - Q \quad (2.12)$$

with

$$Q = \sqrt{\left( M_{12} - \frac{i}{2} \Gamma_{12} \right) \left( M_{12}^* - \frac{i}{2} \Gamma_{12}^* \right)} \quad (2.13)$$

$$= \frac{1}{2} \left( \Delta m - \frac{i}{2} \Delta \Gamma \right). \quad (2.14)$$

Note that

$$\mu_H - \mu_L = \Delta m - \frac{i}{2} \Delta \Gamma \quad (2.15)$$

and

$$\Delta m = 2\text{Re}\sqrt{(M_{12} - \frac{i}{2}\Gamma_{12})(M_{12}^* - \frac{i}{2}\Gamma_{12}^*)} = m_H - m_L \quad (2.16)$$

$$\Delta \Gamma = 2\text{Im}\sqrt{(M_{12} - \frac{i}{2}\Gamma_{12})(M_{12}^* - \frac{i}{2}\Gamma_{12}^*)} = \Gamma_L - \Gamma_H \quad (2.17)$$

The quantities  $\Delta m$  and  $\Delta \Gamma$  are simply the differences in mass and width between the states  $|B_H\rangle$  and  $|B_L\rangle$ .

The time dependence of the mass eigenstates is

$$|B_L(t)\rangle = e^{-i(M_L - \frac{1}{2}\Gamma_L)t} |B_L(0)\rangle \quad (2.18)$$

$$|B_H(t)\rangle = e^{-i(M_H - \frac{1}{2}\Gamma_H)t} |B_H(0)\rangle, \quad (2.19)$$

from which we can get the time evolution of the flavor eigenstates as

$$|B^0(t)\rangle = e^{-i(m + \frac{\Gamma}{2})t} \left( \cos \frac{\Delta m t}{2} |B^0(0)\rangle + i \frac{q}{p} \sin \frac{\Delta m t}{2} |\bar{B}^0(0)\rangle \right) \quad (2.20)$$

$$|\bar{B}^0(t)\rangle = e^{-(im+\frac{\Gamma}{2})t} \left( i\frac{p}{q} \sin \frac{\Delta mt}{2} |B^0(0)\rangle + \cos \frac{\Delta mt}{2} |\bar{B}^0(0)\rangle \right) \quad (2.21)$$

where  $m = (m_L + m_H)/2$  and  $\Gamma = \Gamma_L \approx \Gamma_H$ .

From equation 2.20, we see that for  $t > 0$  there is a finite probability that an initial  $|B^0\rangle$  ( $|\bar{B}^0\rangle$ ) can be observed as a  $|\bar{B}^0\rangle$  ( $|B^0\rangle$ ). This is the phenomenon known as  $B$  meson “mixing”. The time dependent probability that a  $B^0$  decays in same (right-sign or rs) or opposite (wrong-sign or ws) particle/antiparticle state as generated is given by

$$P^{rs} = |\langle B^0 | \bar{B}^0(t) \rangle|^2 = |\langle \bar{B}^0 | B^0(t) \rangle|^2 \quad (2.22)$$

$$P^{ws} = |\langle B^0 | B^0(t) \rangle|^2 = |\langle \bar{B}^0 | \bar{B}^0(t) \rangle|^2 \quad (2.23)$$

where  $P^{rs}$  ( $P^{ws}$ ) is the probability for the “unmixed” (“mixed”) final decays.

From equation 2.20 we get

$$P^{rs} = \frac{1}{2\tau} e^{-\frac{t}{\tau}} (1 + \cos \Delta mt) \quad (2.24)$$

$$P^{ws} = \frac{1}{2\tau} e^{-\frac{t}{\tau}} (1 - \cos \Delta mt) \quad (2.25)$$

where the approximation  $|p/q| \approx 1$  and  $\Delta\Gamma \approx 0$  are used. From the equation we

can see the frequency of the oscillation is given by  $\Delta m$  and the sum of  $P^{rs}$  and  $P^{ws}$  gives us the time dependent probability of  $B^0$  decay, which is a normalized pure exponential.

Calculation of the  $B$  meson box mixing diagrams for the  $\Delta m$  gives[11]

$$\Delta m_q = \frac{G_F^2}{6\pi^2} \eta_B m_{B_q} \hat{B}_{B_q} f_{B_q}^2 M_W^2 S\left(\frac{m_t}{M_W}\right) |V_{tb} V_{tq}^*|^2 \quad (2.26)$$

Here  $q$  stands for either  $s$  or  $d$  and [12][13]

$$S(m_t/M_W) = 0.784(m_t/M_W)^{2 \times 0.76} \quad (2.27)$$

From equation 2.26 we can determine the  $CKM$  matrix elements  $|V_{tb} V_{tq}^*|^2$  in terms of  $\Delta m_q$  with the uncertainty dominated by the theoretical determination of  $\hat{B}_{B_q}$  and  $f_{B_q}$ . Table 2.1 lists the parameters and their values when  $q = d$ . Solving equation 2.26 for  $|V_{td}|$  when  $q = d$  gives

$$|V_{td}| = 0.0077 \pm 0.0013 \quad (2.28)$$

Precise extraction of  $CKM$  elements from measurements of  $\Delta m_d$  are hampered by theoretical uncertainties. Many of these theoretical uncertainties cancel for the ratio of  $\Delta m_s$  and  $\Delta m_d$  :[18]

Symbol	Explanation	Value	Reference
$G_F$	Fermi constant	$1.166 \times 10^{-5} \text{ GeV}^{-2}$	[14]
$\eta_B$	QCD correction factor	$0.55 \pm 0.01$	[15]
$m_{B_d}$	$B_d^0$ mass	5.28 GeV	[14]
$\hat{B}_{B_d}$	“Bag factor”	$1.30 \pm 0.17$	[16]
$f_{B_d}$	$B_d^0$ decay constant	$200 \pm 30 \text{ MeV}$	[16]
$M_W$	$W$ boson mass	$80.419 \pm 0.056$	[14]
$m_t$	Running Top quark mass	$167 \pm 6 \text{ GeV}$	[17]
$S(m_t/M_W)$	Inami-Lim function	2.46	[12][13]
$\Delta m_d$	$B_d^0$ Mixing parameter	$0.472 \pm 0.017 \text{ } \hbar\text{ps}^{-1}$	[14]

Table 2.1: Various parameters and values in equation 2.26

$$\frac{\Delta m_s}{\Delta m_d} = (1.14 \pm 0.08) \left| \frac{V_{ts}}{V_{td}} \right|^2 \quad (2.29)$$

making  $B_s$  decays an important tool for exploring the physics of the CKM matrix.

# Chapter 3

## The Experimental Apparatus

The  $p\bar{p}$  collision Run Ib data of our analysis comes from the CDF detector, which is located at one of the collision points of the Tevatron. The Tevatron is the final stage of the Fermilab accelerator. This chapter describes the Fermilab accelerator and the CDF detector in detail.

### 3.1 The Accelerator

At the very beginning, the gaseous hydrogen from a pressurized tank is ionized to form  $H_2^-$ . The  $H_2^-$  ions are extracted from the ion source by the Cockroft-Walton electrostatic accelerator and accelerated to 750 keV. The  $H_2^-$  then go through the second stage, the Linac, and are accelerated to 400 MeV where they pass through a carbon foil which removes the electrons, leaving only the protons.

The protons then enter the third stage, the Booster, which is 500 feet in diameter, and accelerates the protons to 8 GeV. Next the protons are injected into the 4 miles circumference Main Ring, accelerated up to 150 GeV, and then injected into the Tevatron.

In order to create the antiprotons, protons in the Main Ring are accelerated to 120 GeV, extracted, and guided to hit a tungsten target. In these collisions, antiprotons are produced among the secondary particles. The newly produced antiprotons are selected and transported to the debuncher ring where the transverse dimension of the antiproton beam is reduced in size by a process known as stochastic cooling. Then the antiprotons are transferred to the accumulator ring for storage.

Finally, when a sufficient number of antiprotons have been produced, the antiprotons are injected into the Main Ring, accelerated to 150 GeV and then passed down into the Tevatron in 6 bunches where the antiprotons are accelerated simultaneously with a counter-rotating beam of 6 bunches of protons to an Energy of 900 GeV. Each proton bunch contains  $\sim 20 \times 10^{10}$  particles, and each antiproton bunch contains  $\sim 5 \times 10^{10}$  particles.

After reaching the energy level of 900 GeV, the proton and antiproton bunches are focused into the narrow beams and produce 1.8 TeV center-of-mass  $p\bar{p}$  collisions every  $3.5 \mu\text{s}$ . B0 and D0 are two of the interaction sections, where CDF and D0 detectors are geometrically centered around the interaction regions and the beam. Figure 3.1

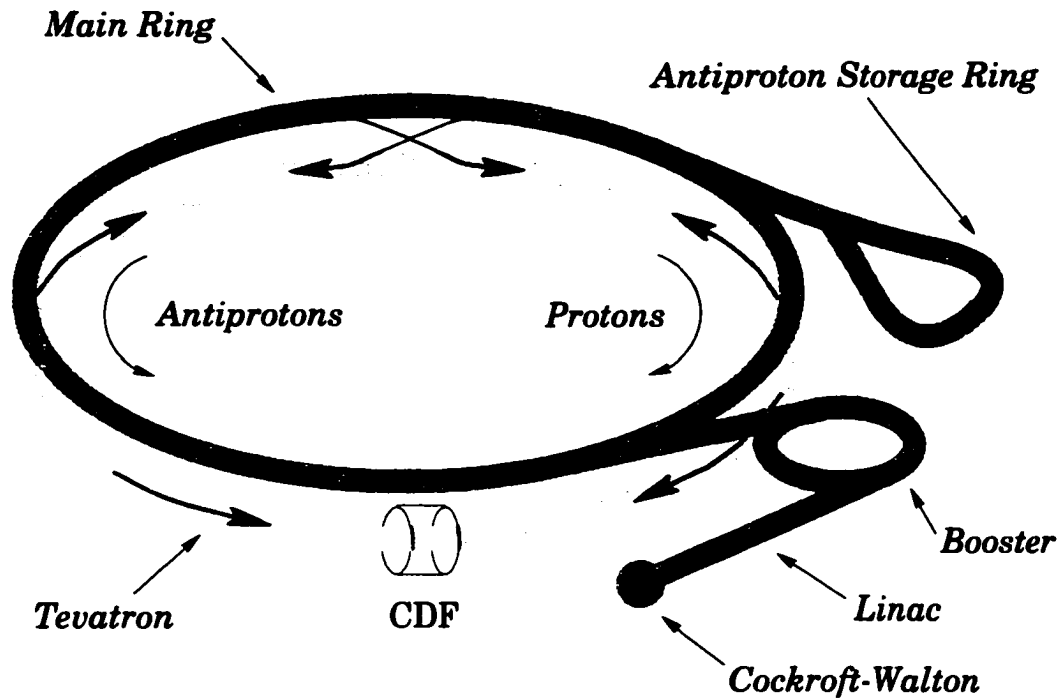


Figure 3.1: A schematic diagram of the accelerator at Fermilab. The CDF experiment is also shown.

is the schematic view of the Fermilab accelerator with CDF experiment shown at the interaction point B0.

This analysis uses  $91 \text{ pb}^{-1}$  of Run Ib data of the Tevatron which was collected from January, 1994, to July, 1995, which is the majority of the Run I data. The average Tevatron luminosity for Run Ib was  $1.6 \times 10^{31} \text{ cm}^{-2} \text{ s}^{-1}$ , with a peak luminosity of  $2.8 \times 10^{31} \text{ cm}^{-2} \text{ s}^{-1}$ .

## 3.2 The CDF detector

The CDF detector has been described in details elsewhere[19]. This section describes in general the CDF detector with details on the portions related to this analysis.

### 3.2.1 The Overview

The CDF detector is a solenoidal detector with azimuthal and forward-backward symmetries around the collision point. A magnetic field of 1.4 Tesla is produced by the superconducting solenoid in order to determine the charge and the momentum of charged particles.

Figure 3.2 shows an isometric view of the detector. Figure 3.3 shows a quarter-view of the CDF detector. The direction of the beam of the protons is defined as the  $z$  axis. The vertical is defined as the  $y$  axis, and then the  $x$  axis is fixed by a right-hand coordinate system and is radially outward from the Tevatron ring. The polar angle  $\theta$  is measured from the positive  $z$  axis and the azimuthal angle  $\phi$  is measured from the  $x$  axis counterclockwise around the  $z$  axis.

In collider physics, a useful quantity is the rapidity with respect to the  $z$  axis and is defined as

$$y \equiv \frac{1}{2} \ln \left( \frac{E + p_z}{E - p_z} \right) \quad (3.1)$$

# CDF Detector

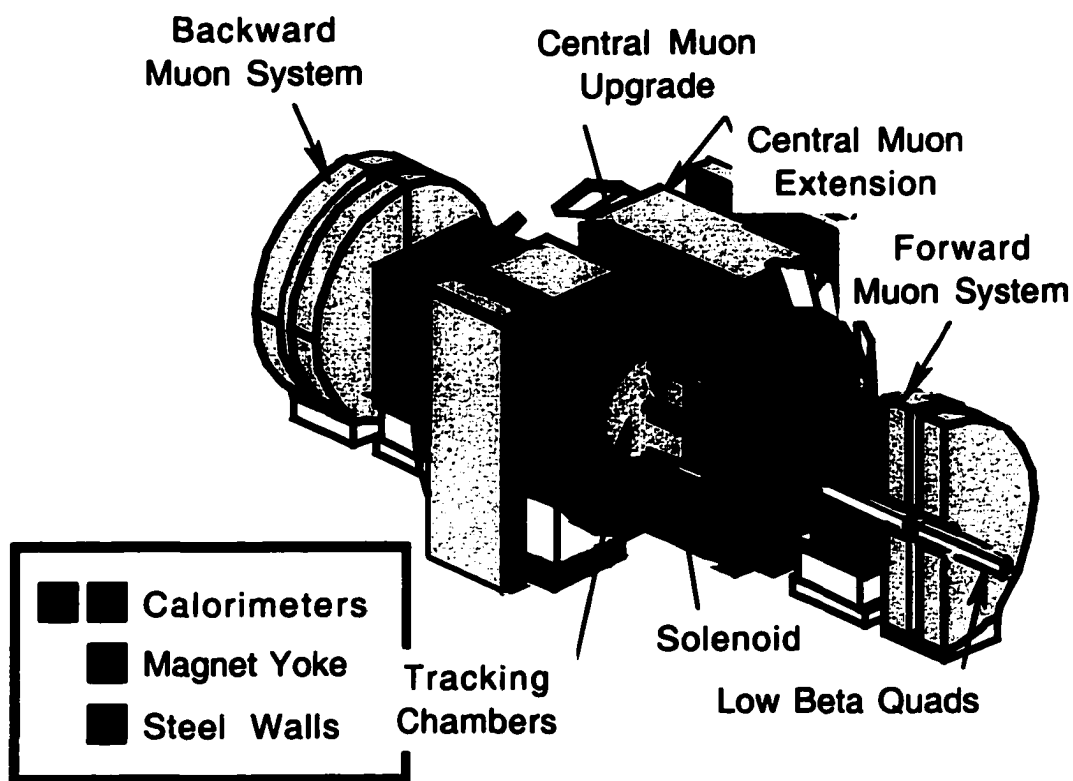


Figure 3.2: An isometric view of the CDF detector.

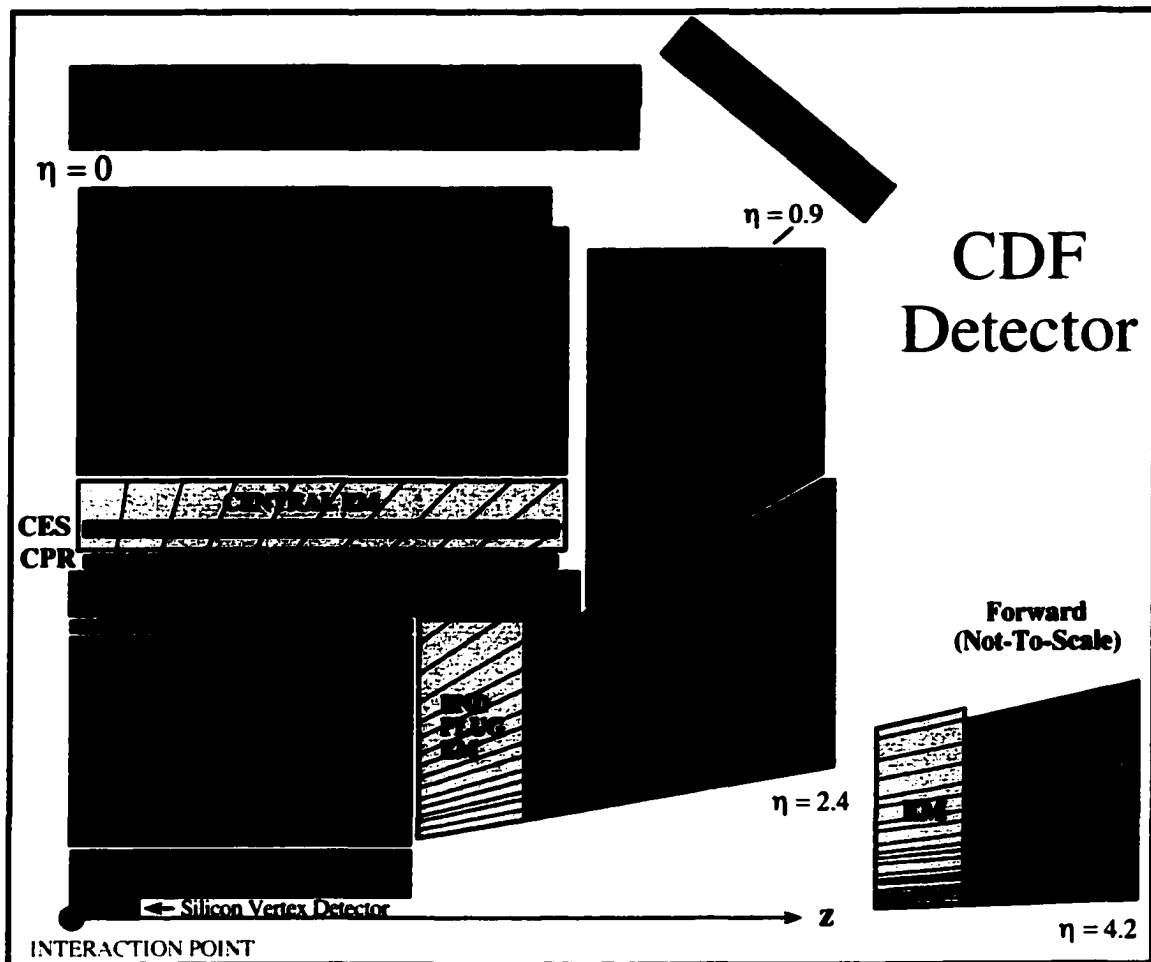


Figure 3.3: Quarter-view of the CDF detector. The detector has forward and backward symmetry around the interaction point as well as azimuthal symmetry. The interaction point is at the lower left of the figure. The z axis points to the east, the y axis points up, and the x axis points into the page.

Rapidities are additive under Lorentz transformation along the  $z$  axis. For ultra-relativistic particles,  $p \gg m$  and the rapidity can be approximated by the pseudo-rapidity

$$\eta \equiv \frac{1}{2} \ln \left( \frac{p + p_x}{p - p_x} \right) = -\ln \tan \frac{\theta}{2} \quad (3.2)$$

Other useful variables are the transverse momentum  $p_T = \sqrt{p_x^2 + p_y^2}$  and the azimuthal angle  $\phi$ . Since particles in energetic hadron collisions are distributed approximately flatly in  $\eta$  and  $\phi$ , the CDF detector was designed to have an approximately cylindrically symmetric layout of detector components with segmentation roughly uniform in these variables.

CDF detector is grouped into three regions: the central region, the plug region and the forward region. This analysis uses only the central region ( $|\eta| < 1.1$  or  $37^\circ < \theta < 143^\circ$ ) data. Starting from the interaction point proceeding radially outward in the central region, the detectors are the Silicon Vertex Detector (SVX), the Vertex Tracking Chamber (VTX) and the Central Tracking Chamber (CTC). These are the charged particle tracking system. Outside the tracking system we have the Central Electromagnetic Calorimeters (CEM) and the Central Hadronic Calorimeters (CHA). Outside the calorimeters resides two sets of muon chambers.

The SVX provides precise position measurement of secondary vertices from B hadron decays. It is very close to the  $p\bar{p}$  collision point, referred to as the primary

vertex where the B hadron is produced. The VTX provides  $z$  position measurement of the  $p\bar{p}$  collision. The CTC measures the trajectory of charged particles. The central calorimeters are used to identify the electrons, and the muon drift chambers are used to identify the muons.

Before describing the CDF detectors in more detail, we describe the CDF tracking parameters. A charged particle follows a helical trajectory in the constant magnetic field. It can be described by 5 parameters as shown in Figure 3.4:

- $C$  : Curvature of the track. The circle radius is  $1/2C$  .
- $d_0$ : Impact parameter, defined as closest radial distance to the beam line.
- $Z_0$  : The  $z$  position at the impact parameter point.
- $\phi_0$ : The  $\phi$  direction at the impact parameter point.
- $\cot\theta_0$  : The cotangent of the polar angle with respect to the beam line.

These 5 parameters are measured by the CTC. The SVX provides additional  $r\phi$  position information primarily improving the resolution of  $d_0$ . The VTX can be combined with CTC to determine the  $z_0$ . The  $p_T$  is related to  $C$  by

$$p_T = \frac{c \cdot B}{2C} \times 10^{-9} \quad (3.3)$$

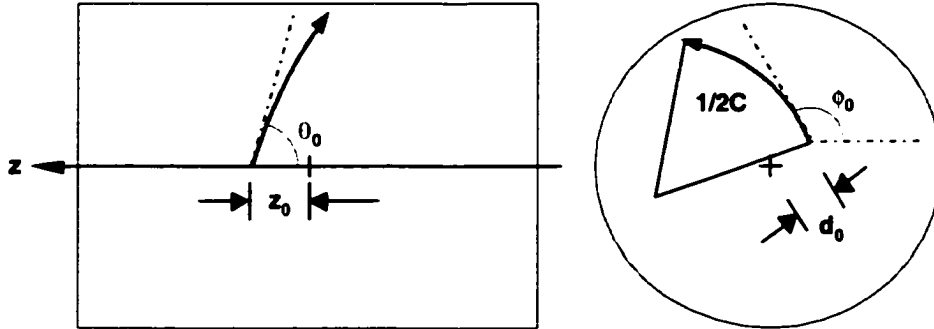


Figure 3.4: Diagram of the 5 tracking parameters from a side-view and end-view of the CTC which describe a charged particle traveling in a magnetic field following a helical trajectory.

Here  $p_T$  is in units of  $\text{GeV}/c$ ,  $c$  is the speed of light, and  $B$  is the magnetic field, which is 1.4 T.

The  $\eta_0$  is related to  $\theta_0$  by equation 3.2:

$$\eta_0 = -\ln \tan(\theta_0/2)$$

### 3.2.2 Tracking

#### The Silicon Vertex Detector (SVX)

The SVX provides tracking information near the beam spot, improving the resolution on  $d_0$  of the charged particle. This information is crucial when combining tracks to

form a secondary vertex such as a  $B^0$  or  $B_s^0$ .

The SVX consists of two independent cylindrical barrels of equal length aligned and centered along the beam line with a gap of 2.15 cm at  $z = 0$ . Figure 3.5 shows a schematic view of one barrel. The active length of the SVX is 51 cm. Due to the length of the proton and antiproton bunches, the primary vertex position has a Gaussian distribution in  $z$  with a rms width of  $\sim 30$  cm. Thus,  $\sim 60\%$  of the  $p\bar{p}$  collisions occur within the SVX. The inner and the outer radii of the barrel are 2.8612 and 7.8658 cm, respectively.

The SVX barrel consists of four concentric layers of silicon strip detectors, numbered from 0 to 3 in increasing radius. Each layer of the silicon strip detectors consists of twelve wedges, called ladders, 25.5 cm in length. Figure 3.6 shows a schematic view of one of the ladders.

Each ladder is divided into three single sided silicon wafers. Each wafer is 8.5 cm long. The wafer has silicon strips on one side only, parallel to the  $z$  axis, thus providing only  $r\phi$  information.

The finely spaced silicon strips of strongly p-doped silicon are deposited on a lightly n-doped bulk substrate. On the opposite side of the substrate a thin layer of strongly n-doped silicon is deposited. The total thickness is  $300 \mu\text{m}$ . A positive bias voltage is applied to the strongly n-doped layer side, creating an electric field in the n-doped substrate and depleting the free electrons in it. When a charged particle

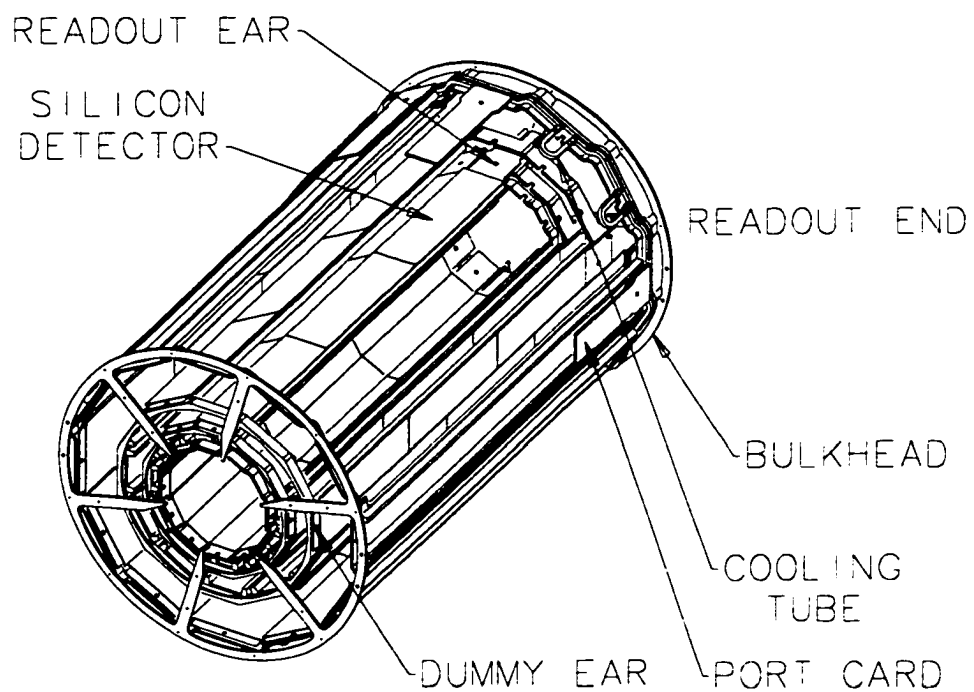


**Figure 3.5: The schematic drawing of one of the SVX barrel.**

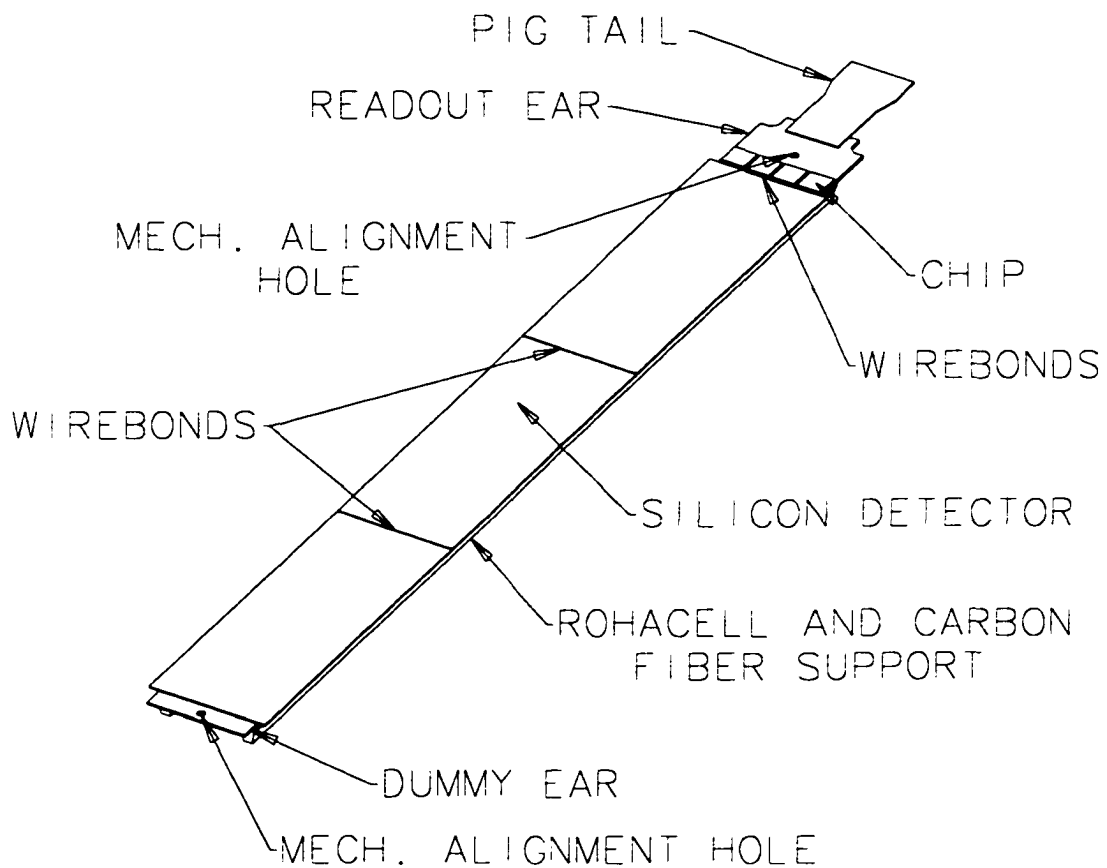


**Figure 3.6: The schematic drawing of a SVX ladder**

passes through the silicon, it leaves a trail of electron/hole pairs from ionization. The holes move to the p-doped strips in the electric field, where the charge is collected and integrated using an integrated circuit attached to the end of the strip.

The width of the strips is  $60 \mu\text{m}$  for the inner 3 layers,  $55 \mu\text{m}$  for the fourth one. A typical track deposits charge across several strips. Combining the weighted charge information across several strips provides a  $10 \mu\text{m}$  hit position resolution. The impact parameter resolution is measured to be  $13 \oplus 40/p_T \mu\text{m}$  where  $p_T$  is measured in  $\text{GeV}/c$  and  $\oplus$  denotes a sum in quadrature.

The data is read out by the SVX chip, which contains 128 channels. There are 2, 3, 4 and 6 chips per ladder on layers 0 to 3, respectively. In total, the SVX has 46,080 channels. Only strips that are significantly over the threshold are read out. The read out time of the SVX detector is about 2 ms, a relatively large value when compared with the read out time of the other CDF detector systems.

### **The Central Tracking Chamber (CTC)**

Surrounding the VTX, the CTC is the principle tracking device of the CDF detector. The SVX measures only  $d_0$  and  $\phi$ , while the CTC measures all the 5 track parameters. If possible, the information from both trackers is combined to form a global track fit to achieve better resolution.

The CTC is a cylindrical multi-wire drift chamber 3.214 m long with active area radius from 0.309 to 1.320 m. It is inside a 1.4 T solenoidal magnet and is filled with

Table 3.1: Some features of CTC.

Super Layer	Sense Wires per Cell	Number of Cells	Stereo Angle
0	12	30	0°
1	6	42	+3°
2	12	48	0°
3	6	60	-3°
4	12	72	0°
5	6	84	+3°
6	12	96	0°
7	6	108	-3°
8	12	120	0°

an argon-ethane gas mixture. Figure 3.7 shows the CTC end-plate with the position of the wire planes. There are totally 36,504 sense and field shaping wires extended along the length of the CTC.

The wires in the CTC are arranged into 84 layers which are divided into 9 super-layers, numbered 0 to 8, five axial and four stereo layers. The axial super-layers have twelve layers of wires and are alternated with the stereo super-layers each of which has six layers of wires. Figure 3.8 shows the wire positions for a CTC axial super-layer cell.

The sense-wire layers are tilted by 45° with respect to the radial direction. For the stereo layers, there are additional small  $\pm 3^\circ$  rotations about an axis in the radial direction, which introduces a  $z$  dependence to the  $r\phi$  measurement. When combined with the axial layers, the stereo layers provide information to measure the  $z_0$  and  $\cot\theta_0$  of tracks. Table 3.1 summarizes some features of CTC.

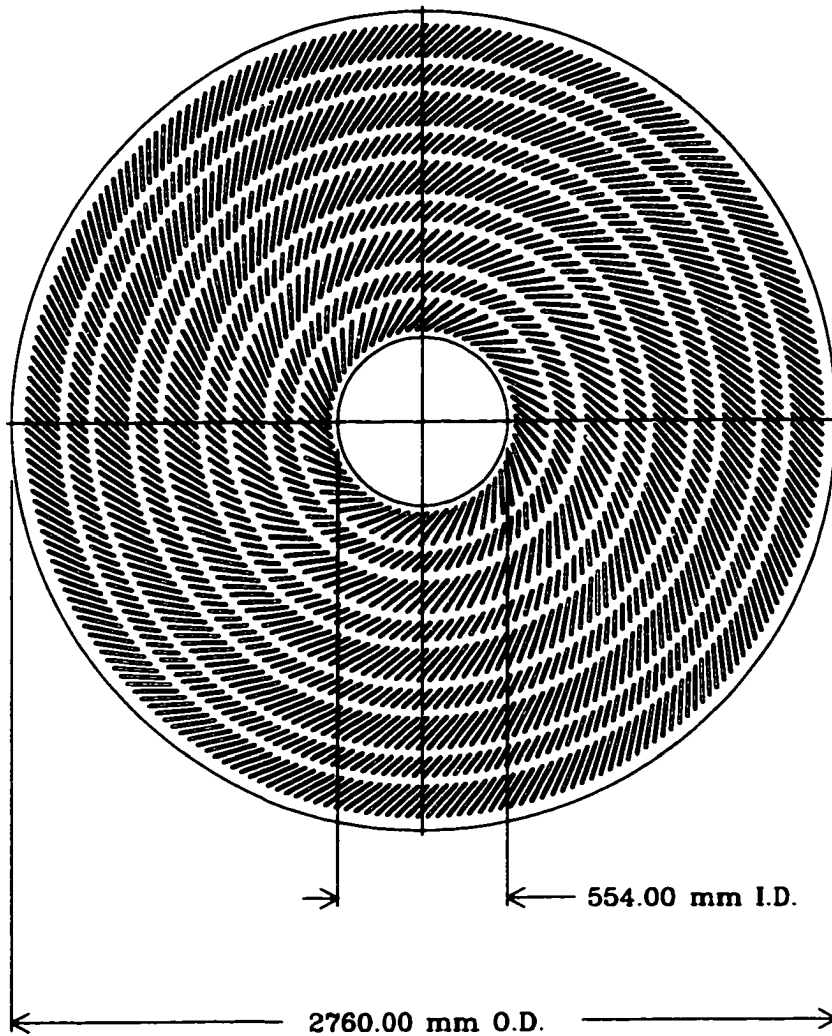


Figure 3.7: Diagram of the Central Tracking Chamber (CTC) end-plate showing the location of the wire planes.

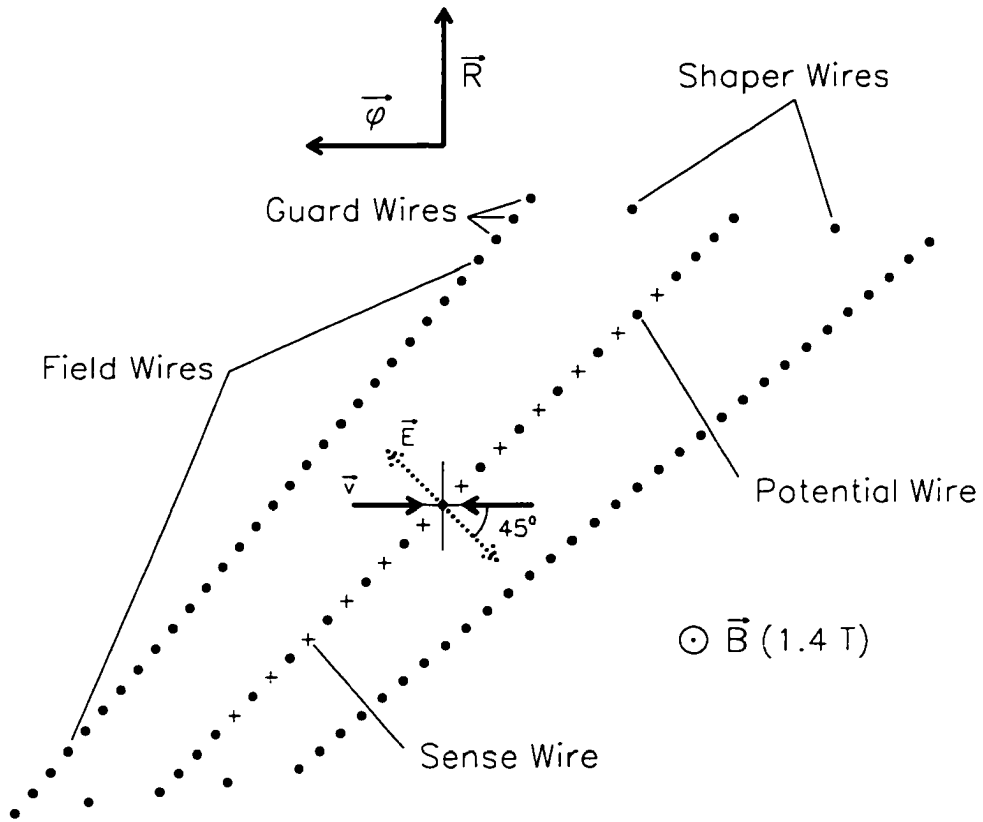


Figure 3.8: The wire positions for an axial super-layer cell of CTC

The momenta of charged particle is determined from the curvature of their ionization tracks as they pass through the magnetic field in the CTC. When the charged particles pass through the CTC, they ionize the gas and the electrons drift toward the sense wires. As they approach the sense wires, the electric field becomes much stronger due to the  $1/r$  potential and the accelerating electrons create an avalanche of other electrons from atoms in the gas. This avalanche of electrons provides the gain to make the ionization signal large enough to be detected. A high momentum track traveling radially passes through a maximum of 84 cells which provide the measurements for determining the track's curvature and thus momentum. The wires within a super-layer are grouped in measurement cells so that the maximum drift distance is less than 40 mm, corresponding to 800 ns of drift time.

Because of the CTC sense-wire layers  $45^\circ$  tilt design, the electrons drift perpendicularly to the radius vector, in a trajectory determined by the  $\vec{E} \times \vec{B}$  of the electric and magnetic fields, which gives the best resolution on the tracks. This design also ensures that high  $p_T$  tracks pass close to at least one sense wire. This angle also resolves the left-right ambiguity arising from the fact that it is impossible to tell which side of the sense wire the electrons drift from. Wrong assignment results in a fake track, which must also be considered in the pattern recognition. In the CTC the fake track is rotated by an angle of  $70^\circ$  with respect to the real track, simplifying the pattern recognition.

The CTC individual hit resolution is around 0.2 mm for  $r - \phi$  and 4 mm for  $r - z$ .

The transverse momentum resolution for the CTC is

$$\delta p_T / p_T = 0.002 \times p_T$$

where  $p_T$  is in units of GeV/c. If combined with SVX, the resolution is improved by a factor of about two.

### 3.2.3 The Central Calorimeters

The central region of the calorimeters is segmented in azimuthal and pseudo-rapidity increments to form a projective tower geometry pointing back to the nominal interaction point. The central region has an electromagnetic calorimeter labeled CEM, and behind it is a hadronic calorimeter labeled CHA. This allows a detailed comparison of the electromagnetic and hadronic energies deposited in each tower, thus separating electrons and photons from other hadrons.

The central EM calorimeter covers the entire  $\phi$  angle range and  $|\eta| < 1.1$ . The central EM calorimeter towers are  $15^\circ$  in  $\phi$  and 0.11 units wide in  $\eta$ . The CEM energy resolution is  $13.7\% / \sqrt{E_T} \oplus 2\%$  for incident electrons and photons. The symbol  $\oplus$  means that the constant term is added in quadrature to the resolution. The thickness of CEM is 18 radiation lengths. Figure 3.9 shows one CEM wedge. The CHA covers  $|\eta| < 0.9$  and the energy resolution is  $50\% / \sqrt{E_T} \oplus 3\%$  for incident pions. The thickness

of the CHA is 4.5 interaction lengths.

The CEM is composed of alternating layers of lead and scintillator. An EM shower develops in the lead and hits the scintillator and generating blue light. The blue light is collected and wave-shifted to green light by plastic wavelength-shifters at the ends of the scintillators. The green light is transmitted by waveguides to photo-multiplier tubes (PMT). The total amount of collected light is proportional to the initial electron energy.

At 6 radiation lengths into the CEM calorimeter there are central proportional chambers with strip and wire readout called the central electromagnetic strip detector (CES). The CES provides shower position measurements in both the  $z$  and the  $r - \phi$  views.

### **3.2.4 The Central Muon Detectors**

Because the muon's mass is 200 times that of the electron, it is much less efficient in initiating electromagnetic showers. The muon also does not interact hadronically, so it can pass through the hadron calorimeter, which acts as a hadron absorber for the central muon detection systems. Charged particles that penetrate the calorimeters and reach the muon detectors are most likely muons.

Two muon systems are located centrally covering  $|\eta| < 0.6$ , the central muon chambers (CMU) and the central muon upgrade (CMP). Both muon detectors con-

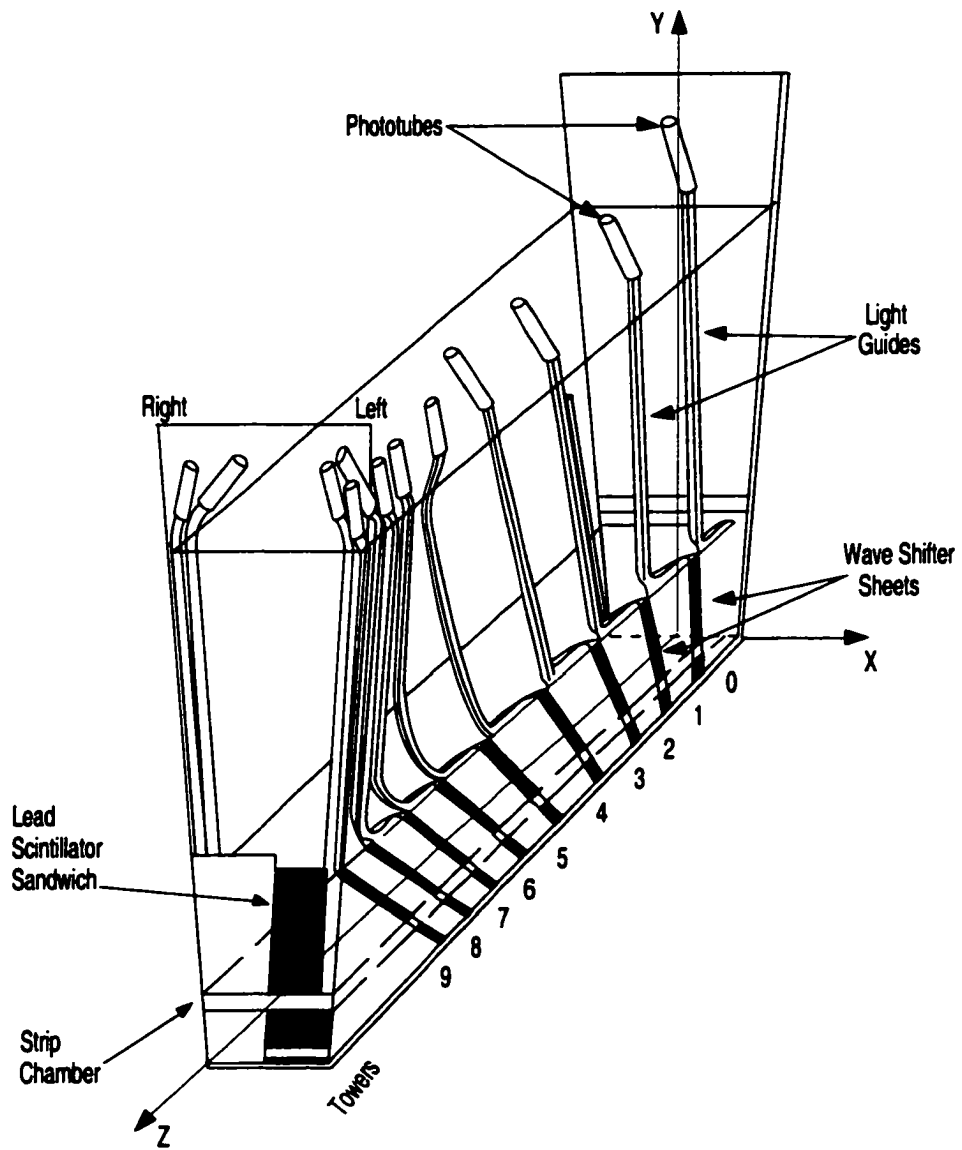


Figure 3.9: A CEM wedge.

sist of four layers of drift chambers. The CMU is located just outside the central hadronic calorimeters. The CMP chambers are further outside the detector behind an additional 60 cm of steel.

An extension to the central muon systems is called the central muon extension (CMX), located in conical arches covering  $0.6 < |\eta| < 1.0$  to complement the tracking coverage of the CTC. This extension is comprised of eight layers of drift chambers sandwiched between scintillator counters.

The central muon systems record only “muon stubs”, that is, track segments in drift chambers left by muon candidates. The muon drift chambers have a spatial resolution of  $280 \mu\text{m}$  in the  $\phi$  direction and  $1.2 \text{ mm}$  in  $z$ . In the pattern recognition, these track “stubs” in the muon chambers are matched to tracks in the CTC to identify them as muon candidates. That is, the hits in the muon chambers are required to match the extrapolated CTC track in both location and slope at the entry into the chamber. The system is almost 100% efficient for central muons with  $p_T > 3 \text{ GeV}/c$ .

### **3.2.5 Triggers**

CDF was built to study the physics resulting from  $p\bar{p}$  interaction at a center of mass energy of  $1.8 \text{ TeV}$ . The beam crossing occurs every  $3.5 \mu\text{s}$ . If we expect at least one interaction per crossing, we expect to have an interaction rate of about  $286 \text{ kHz}$ . The

rate of data taking is limited mostly by the rate at which events can be written to tape, which is about 10 Hz. So 1 event must be selected out of every 20-30 thousand events. This is accomplished with the CDF trigger system.

The CDF trigger consists of 3 levels. Level 1 and Level 2 are made of specially designed hardware which makes the decision to initiate the full detector readout. Level 3 trigger is a software trigger. The purpose of a multi-level trigger system is to introduce as little bias as possible at the lower levels, with the goal of reducing the rate to a point where the next level can do a more complex analysis without incurring significant dead-time. The read out of the detector components is of order 1 ms. So to keep the dead time due to readout below 10%, the detector readout should begin after the Level 2 trigger has reduced the rate to 100 Hz or less.

The Level 1 trigger looks for signs of an interaction, such as hits in the beam-beam counters, energy in the calorimeter, or a candidate muons in one of the muon chambers. The output rate of the Level 1 trigger is about 1 KHz.

The Level 2 trigger bases its decision on the calorimeter and muon information, as well as the CTC tracks found by the Central Fast Tracker (CFT). The CFT is a hardware tracker which uses hits in the axial super-layers of the CTC and pre-programmed hit patterns to reconstruct tracks and provide a Level 2 trigger. For the inclusive lepton trigger case, only higher  $p_T$  tracks ( $> 7.5$  GeV) are matched to the hits in the muon chambers and showers in the EM calorimeter. The output rate of

the Level 2 trigger is about 20 to 30 Hz.

If the event passes the Level 2 trigger, it is read out fully by the CDF detectors. The Level 3 trigger thus has the full event information so it can perform event reception, building, reconstruction, classification, and selection. After this process, the Level 3 trigger makes the final decision whether an event should be written to tape or not. The output rate of the Level 3 trigger is about 1 to 4 Hz and is limited by the rate at which the events can be written to tape.

### **The Inclusive Electron Trigger**

The inclusive electron trigger requires an EM energy cluster with greater than 8.0 GeV transverse energy. The ratio of the total  $E_T$  (electromagnetic and hadronic) over the electromagnetic  $E_T$  must be less than 1.125. There must also be a CFT track with greater than 7.5 GeV/c transverse momentum pointing at the EM energy cluster, where the track matching is done using the wires in the CES. The cross section for the inclusive electron trigger is about 200 nb.

### **The Inclusive Muon Trigger**

The inclusive muon trigger requires a CFT track with greater than 7.5 GeV/c transverse momentum pointing at hits in the central and upgrade muon chambers. The extrapolation of the CFT track to the position of the muon chambers and the position of the hits in the muon chambers are required to agree within  $5^\circ$ . The cross section

for the inclusive muon trigger is about 100 nb.

# Chapter 4

## Data Selection

### 4.1 Data Sample

For a time dependent  $B_s^0$  mixing analysis, in each event we need to know the flavor of the  $B_s^0$  both at production and at decay. We also need to know the proper time  $t$  at decay for the  $B_s^0$  meson as well as the resolution of this measurement.

The trigger side (same side) lepton tells us the flavor of the  $B_s^0$  at decay. The flavor of the  $B_s^0$  at production is determined by opposite side flavor tagging which, will be described in detail in the following chapter.

The proper time is determined by measuring the point of decay versus the point of production in the transverse ( $x - y$ ) plane for the  $B_s^0$  meson that produced the trigger lepton. This is done by searching for tracks close to the trigger lepton to form a vertex (the secondary vertex) separated from the point of the  $p\bar{p}$  collision

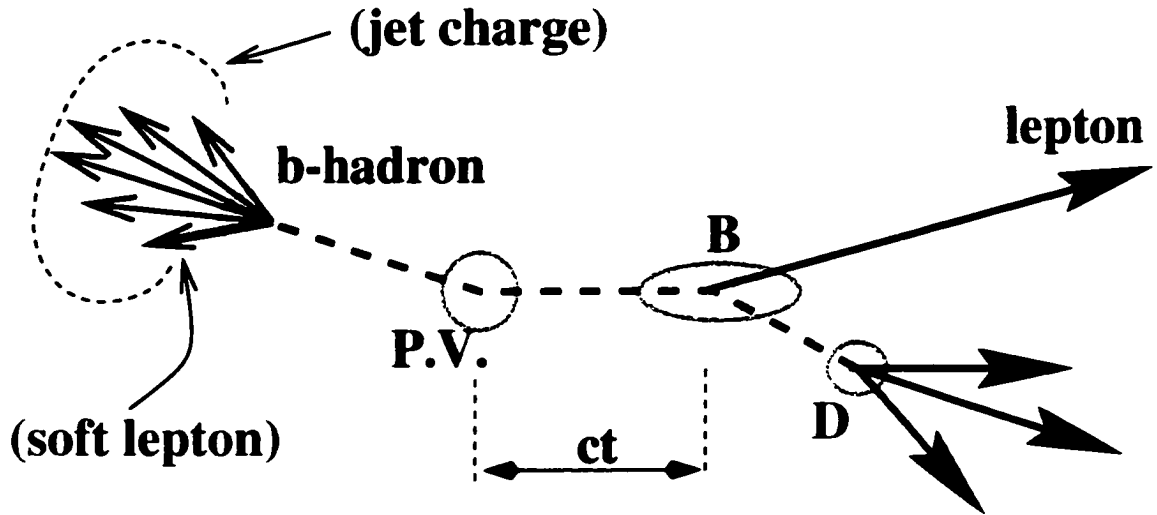


Figure 4.1: A general diagram of the decay mode  $B \rightarrow \nu \ell D$ . Here  $B$  can be  $B_s^0$  and  $D$  be  $D_s$ , where  $D_s \rightarrow \phi\pi$ ,  $\phi \rightarrow KK$  or  $D_s \rightarrow K^{*0}K$ ,  $K^{*0} \rightarrow K\pi$ . The flavor tag is obtained from the decay on the opposite side; if the decay of the opposite side  $b$ -hadron is semileptonic, and the lepton is found, its charge is used as the flavor tag. Otherwise the charge of the  $b$ -jet (weighted by transverse momentum) is used.

(the primary vertex). The measurement of the two dimensional  $(x, y)$  distance  $L_{xy}$  between the primary vertex and the secondary vertex, combined with an estimation of the  $B_s^0$  meson transverse momentum ( $p_T(B_s^0)$ ) enables the measurement of the proper decay time  $t$ .

This analysis uses the Run 1b inclusive lepton trigger data collected during the 1993-1995 run corresponding to approximately  $90 \text{ pb}^{-1}$  data. The following section describes in detail how we reconstruct and select the data.

## 4.2 Reconstruction of $B_s^0 \rightarrow \nu \ell D_s$ Decays

We reconstruct semileptonic  $B_s^0$  decays in the inclusive lepton datasets (both electron and muon triggers are used). We consider  $D_s$  decays of two kinds:  $D_s^- \rightarrow \phi \pi^-$  followed by  $\phi \rightarrow K^+ K^-$ , or  $D_s^- \rightarrow K^{*0} K^-$ , followed by  $K^{*0} \rightarrow K^+ \pi^-$ . In both cases, the final state consists of two oppositely charged kaons and one pion, and the only difference is in their resonant sub-structure. Correspondingly, the search criteria for these two decay modes are similar. The flavor tag is obtained from the decay on the opposite side; if the decay of the opposite side  $b$ -hadron is semileptonic, and the lepton is found, its charge is used as the flavor tag. Otherwise the charge of the  $b$ -jet (weighted by transverse momentum) is used. Figure 4.1 shows a diagram of the  $B$  decay on one side, and the  $b$ -hadron decay (used for flavor tagging) on the opposite side.

We now describe the reconstruction of the  $D_s \rightarrow \phi \pi$  mode. The reconstruction of the  $K^{*0} K$  mode proceeds in a similar way. The reconstruction process starts with a trigger lepton, which has to satisfy a relatively loose set of electron or muon identification cuts. In a cone around this lepton, we first consider oppositely charged track pairs, assume that they are  $K^+ K^-$ , and check whether this track pair satisfies the  $\phi$  selection cuts (including that the invariant mass of this track pair – assuming they are kaons – is close to  $m_\phi$ ). We then use the vertexing package CTVMFT to constrain the two tracks to pass through a common point, and require that the probability of this fit is  $> 1\%$ . The fit probability is the probability that a  $\chi^2$  function

with ndof degrees of freedom has a value greater than the actual  $\chi^2$  of the fit. Thus, small  $\chi^2$  give large probabilities (maximum 1) indicating a good fit, and large  $\chi^2$  give small probabilities.

If this track pair passes the  $\phi$  cuts, we add another track, assume that it is a  $\pi$ , use CTVMFT to see if the three tracks intersect at a common vertex, calculate the invariant mass of the three tracks, and check whether it's close to the  $D_s^-$  mass. Then we extrapolate the  $D_s^-$  candidate back along its flight path to intersect it with the lepton track and find the  $B_s^0$  decay vertex.

In the following sections we give the selection cuts in more detail.

#### 4.2.1 Selection Cuts For $B_s^0 \rightarrow \ell D_s, D_s \rightarrow \phi\pi$ Mode

- Tracks:
  - loose electron and muon identification cuts
  - all four tracks are required to be ‘good SVX’ tracks. This means:
    - \* in CTC, at least two axial and two stereo layers with at least two hits
    - \* CTC exit radius of  $> 130$  cm (CTC exit radius is the radial position at which the track crosses the plane that defines the edge of the CTC in  $z$ .)
    - \* at least three hits in the SVX
    - \* for the SVX fit,  $\chi^2/N_{hit} < 6$

– hadrons in cone of  $\Delta R < 1$  around the lepton

\*  $\Delta R(K) < 0.69, \Delta R(\pi) < 0.92$

• Kinematic cuts:

–  $p_T(K) > 1.2 \text{ GeV}, p_T(\pi) > 0.73 \text{ GeV}$

–  $p_T(\phi) > 2.9 \text{ GeV}, p_T(D_s) > 3.5 \text{ GeV}$

–  $|m(K, K) - 1.0194| < 0.01 \text{ GeV}$

–  $3.1 < m(\ell D_s) < 5.5 \text{ GeV}$

• Helicity: ( $\psi \equiv \text{angle}(K, D_s)$  in  $\phi/K^{*0}$  CM frame)  $0.42 < |\cos \psi| < 1.0$

• Vertex cuts

– Vertex probability  $> 1\%$

–  $\sigma_{ct}(B_s^0) < 0.1 \text{ cm}$

#### 4.2.2 Selection Cuts For $B_s^0 \rightarrow \ell D_s, D_s \rightarrow K^{*0}K$ Mode

• Tracks: exactly the same as in the case of  $D_s \rightarrow \phi\pi$ , except

– hadrons in cone of  $\Delta R < 1$  around the lepton

\*  $K_1$  from  $K^{*0}, K_2$  from  $D_s$

\*  $\Delta R(K_1) < 0.73, \Delta R(K_2) < 0.54, \Delta R(\pi) < 0.85$

- **Kinematic cuts**

- $p_T(K_1) > 1.5 \text{ GeV}, p_T(K_2) > 1.7 \text{ GeV}, p_T(\pi) > 0.57 \text{ GeV}$

- $p_T(K^{*0}) > 2.0 \text{ GeV}, p_T(D_s) > 2.5 \text{ GeV}$

- $|m(K_1, \pi) - 0.8961| < 0.055 \text{ GeV}$

- $3.4 < m(\ell D_s) < 5.5 \text{ GeV}$

- **Helicity:** ( $\psi \equiv \text{angle}(K, D_s)$  in  $\phi/K^{*0}$  CM frame  $|\cos \psi| > 0.63$ )

- **Vertex cuts:**

- Vertex probability  $> 1\%$

- $\sigma_{ct}(B_s^0) < 0.1 \text{ cm}$

### 4.2.3 $D_s$ Mass Fit Result

Figure 4.2 shows the fitted  $K^+K^-\pi$  mass distribution for  $D_s \rightarrow \phi\pi$ . The solid histograms represent events where  $\ell^+$  and  $D_s^-$  have correct charge correlation (opposite charge), and the dashed ones where they do not. We note that the fact that the sample with the ‘wrong  $\ell - D_s$  charge correlation’ exhibits no  $D_s$  mass peak implies that the contribution of other channels with a  $D_s$  and a fake lepton is negligible, and thus that all  $D_s$  events are coming from a semileptonic  $B_s^0$  decay.

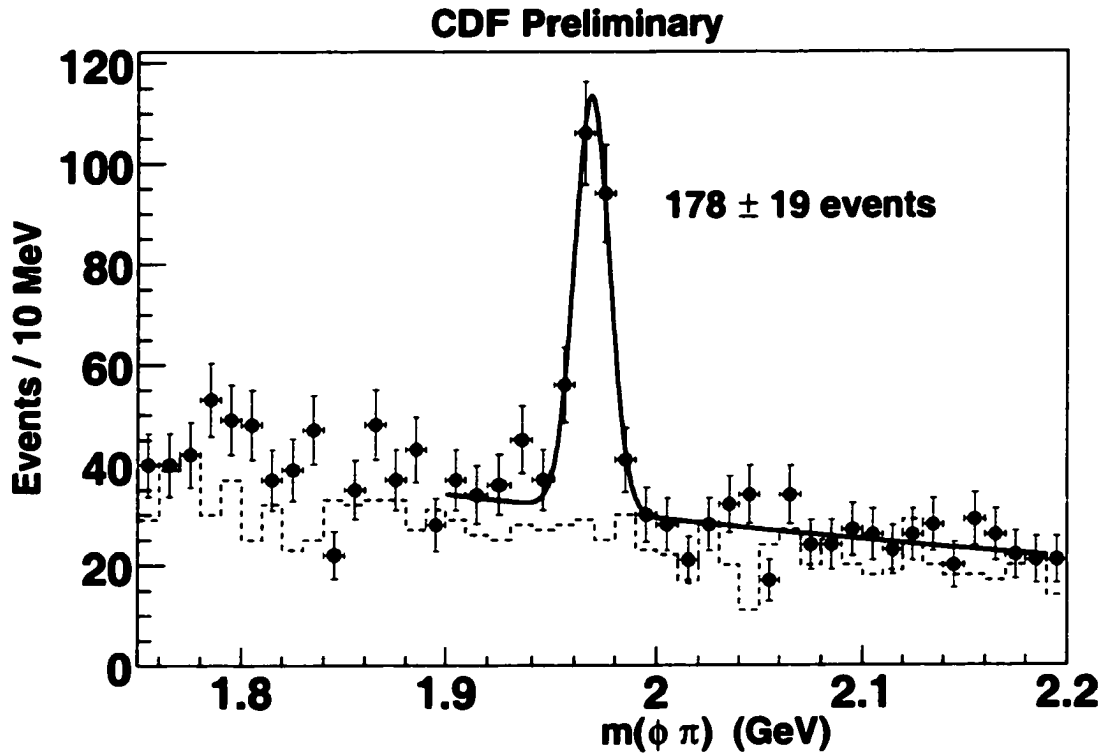


Figure 4.2: The  $KK\pi$  invariant mass distribution for the  $\ell^+ D_s^-$  decay channel, where  $D_s^- \rightarrow \phi\pi$ . We fit the mass distribution with a single Gaussian that describes the  $D_s$  signal, and with an exponential that describes the shape of the combinatorial background. The fit is superimposed on top of the data points. The dashed histogram represents events where lepton and  $D_s$  have the same charge.

The data points (true  $B_s^0$  signal) are fitted with a single Gaussian (for the signal) and a decreasing exponential (for the combinatorial background), and the fit result is overlaid.

For  $\phi\pi$  mode, the fit yields signal of  $178 \pm 19$  events with  $S/B = 1.66$ . The  $S$  here means the signal events in the signal region and  $B$  is the background events in the signal region. The statistical power of the mixing measurement depends on  $S/\sqrt{S+B}$  (see equation 7.4), which is 10.2 for this mode. The fitted  $m(\phi\pi) = 1968.6 \pm 1.0$  MeV, agrees with PDG value 1968.5 MeV. We use the fit range 1.9-2.2 in order to avoid the Cabibbo-suppressed decay  $D^- \rightarrow \phi\pi^-$ .

For the  $K^{*0}K$  decay mode, the  $KK\pi$  invariant mass distribution is further complicated by the presence of a  $D^-$  reflection. This case is special and is described below.

#### 4.2.4 Estimating the Contribution of $D^-$ to the $D_s \rightarrow K^{*0}K$ Decay mode

Reference [20] describes in detail the physics background for  $K^{*0}K$  mode in the context of the measurement of the  $B_s^0$  meson lifetime. A  $D^-$  can decay to  $K^{*0}\pi$  and the reconstruction code use the  $\pi$  from the  $D^-$  as a  $K$  and reconstruct it as  $D_s$ .

We obtain the shape of this reflection from the Monte Carlo simulation and then employ it in the fit to the invariant mass of  $KK\pi$  candidates (together with the signal

Gaussian and the exponential combinatorial background) to derive the  $D^-$  fraction in the whole mass region.

We use a CDF Monte Carlo event generator (BGEN) to generate 18 million of  $B^0 \rightarrow \ell^+ D^{(*)-}$  events. We force  $D^- \rightarrow K^{*0} \pi^-$  with  $K^{*0} \rightarrow K^+ \pi^-$ . The reconstruction code takes the  $\pi$  from the  $D^-$  as a  $K$  and the candidate is reconstructed as a  $D_s$ . The plot on the top right of figure 4.3 shows the reconstructed  $D^-$  mass distribution when it is reconstructed as a  $D_s$ , with the fit overlaid (the vertical scale on the inset is arbitrary).

The fitting function for the  $D^-$  reflection is a product of an error function and an exponential:

$$M_{B^0} = \begin{cases} c \operatorname{ERF}(\alpha(m - m_0)) \exp(\beta(m - m_0)) & \text{when } m > m_0 \\ c \operatorname{ERF}(\alpha(m - m_0)) & \text{when } m \leq m_0 \end{cases} \quad (4.1)$$

where  $\operatorname{ERF}()$  is the error function. We use a binned likelihood fit to get the shape of the  $D^-$  reflection, that is, fit to get the parameters  $\alpha$ ,  $\beta$  and  $m_0$ .

After we get the shape of this  $B^0$  reflection from the fit, we can build the total  $D_s$  mass function by adding the three functions together: the  $B^0$  reflection, Gaussian for the signal, an exponential for the combinatorial background

$$F(m) = c_1 M_{B^0} + c_2 G(m - m_{D_s}, \sigma) + c_3 \exp(-\gamma m) \quad (4.2)$$

We fit for all the other parameters except the shape of  $B^0$  reflection using a binned likelihood fit (result shown in Figure 4.3) to obtain  $178 \pm 43$  signal events. The mean of the  $D_s$  Gaussian is  $m(D_s) = 1.9715 \pm 0.0022 \text{ GeV}/c^2$ , in agreement with the world average value. The  $S/\sqrt{S+B}$  equals 7.9. An unbinned likelihood fit gives the fraction of  $B_s^0$  over  $B_s^0 + B^0$  in  $\pm 3\sigma$  region of the signal as  $(100_{-14.0}^{+0.0})\%$ . The errors here are used for the systematic studies.

We can also estimate the fraction of  $B_s^0$  in  $3\sigma$  signal region from the reconstruction efficiency of  $K^{*0}K$  and  $K^{*0}\pi$  obtained from the Monte Carlo calculation and the branching ratios of various decays involved in these decay chains. Of 18 million generated  $B^0$  events, 10,300 pass the reconstruction cuts. Of 32 million generated  $B_s^0$  events, 52,100 pass the reconstruction cuts. Finally, 54.6%  $B^0$  events are in the  $B_s^0 \pm 3\sigma$  signal region, giving

$$\begin{aligned} \frac{N(B_s^0)}{N(B^0)} &= \frac{f_s \cdot Br(B_s^0 \rightarrow \ell D_s \nu) \cdot Br(D_s \rightarrow K^{*0}K, K^{*0} \rightarrow K\pi) \cdot \epsilon(K^{*0}K)}{f_d \cdot Br(B^0 \rightarrow \ell D^- \nu) \cdot Br(D^- \rightarrow K^{*0}\pi, K^{*0} \rightarrow K\pi) \cdot \epsilon(K^{*0}\pi)} \\ &= \frac{16.0\% \cdot 8.1\% \cdot 3.3\% \cdot 52.1K/32M}{37.5\% \cdot 6.7\% \cdot 1.27\% \cdot 10.3K/18M \cdot 0.546} = 6.98 \end{aligned} \quad (4.3)$$

This yields 87.5% for  $B_s^0$  fraction over  $B_s^0 + B^0$  but with relatively large errors.

This is consistent with the results of the fit.

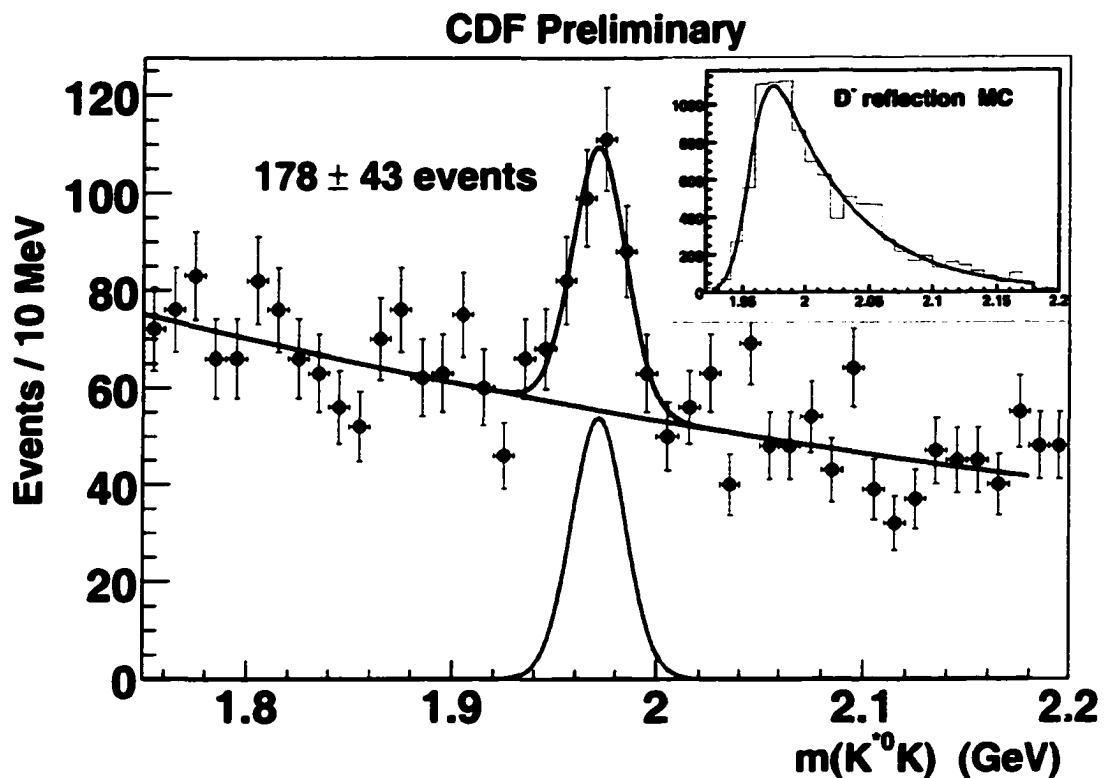


Figure 4.3: The  $KK\pi$  invariant mass distribution for the  $\ell^+ D_s^-$  decay channel, where  $D_s^- \rightarrow K^{*0} K^-$ . We fit the mass distribution with a single Gaussian that describes the  $D_s$  signal, the  $M_{B^0}(m)$  function that describes the  $B^0$  reflection and an exponential that describes the shape of the combinatorial background. The scaled  $B^0$  reflection histogram with the fitted function (the horizontal scale is enlarged) and the single Gaussian are also in the plot.

# Chapter 5

## Flavor Tagging

### 5.1 Introduction

In order to make a measurement of the oscillation frequency of  $B_s^0$ , we need to know the flavor of the  $B$  meson (is it a  $B_s^0$  or a  $\bar{B}_s^0$ ) both at production and at decay. We determine the flavor of the  $B$  meson at decay by the decay products. For the flavor of the  $B$  meson at production, because  $b\bar{b}$  quarks are generated in pairs, we use flavor of the opposite side  $B$  to determine the flavor of the same side  $B$  meson. We assume the opposite side  $B$  has opposite flavor from the same side  $B$  flavor at production. This is not always true, since we have a small but finite probability that the opposite  $B$  is a  $B_d^0$  or  $\bar{B}_d^0$  which can mix, which is taken into account. The algorithm to determine the flavor of the opposite  $B$  meson is called flavor tagging.

### 5.1.1 Dilution

The most important quantity that describes the performance of the tagging algorithms is called the dilution ( $D$ ), given by

$$D = \frac{N_{tag} - N_{mistag}}{N_{tag} + N_{mistag}}, \quad (5.1)$$

where  $N_{tag}$  is number of correctly tagged events and  $N_{mistag}$  is number of incorrectly tagged events.  $D = 1$  for perfectly tagging,  $D = 0$  for randomly tagging, and  $D = -1$  when the tagging is always opposite the true flavor.

$D$  is related to  $P_{mistag}$  and  $P_{tag}$  by

$$D = 1 - 2P_{mistag} \quad (5.2)$$

$$D = 2P_{tag} - 1$$

or

$$P_{mistag} = \frac{1 - D}{2} \quad (5.3)$$
$$P_{tag} = \frac{1 + D}{2}$$

where  $P_{tag}$  ( $P_{mistag}$ ) is the probability that the tag is correct(incorrect). The tagging efficiency  $\epsilon$  is simply the fraction of events that have a tag, that is,

$$\epsilon = \frac{N_{tag}}{N_{tot}}. \quad (5.4)$$

Consider an asymmetry measurement with  $N_{tot}$  events, dilution  $D$ , and tagging efficiency  $\epsilon$ . Among the  $N_{tag}$  tagged events, there are  $N_{rs}$  measured right sign events where the  $B_s^0$  does not mix and  $N_{ws}$  measured wrong sign events where the  $B_s^0$  mixes. The measured asymmetry is

$$A_{meas} = \frac{N_{rs} - N_{ws}}{N_{rs} + N_{ws}} \quad (5.5)$$

The true asymmetry is

$$A_{true} = \frac{1}{D} A_{meas} \quad (5.6)$$

with a statistical uncertainty

$$\sigma_A = \sqrt{\frac{1 - D^2 A^2}{\epsilon D^2 N_{tot}}} \quad (5.7)$$

We can see that the error scales as  $1/\sqrt{\epsilon D^2 N}$ , rather than the more familiar term  $1/\sqrt{N}$ .  $\epsilon D^2 N$  is the effective number of tagged events and  $\epsilon D^2$  gives the statistical power of this flavor tagging method. When tuning the cuts for the certain flavor

tagging method, we maximize the quantity  $\epsilon D^2$ .

In our analysis we use two flavor tagging methods: Soft Lepton Tagging(SLT) and Jet Charge Tagging(JQT), both of which rely on the opposite side  $B$  of the same event. In general, SLT has low efficiency but high dilution. whereas JQT has high efficiency but low dilution.

### 5.1.2 Dilution Calibration

Due to low statistics of the reconstructed  $B_s^0$  and its high oscillation frequency, we can not determine the dilution directly from the  $B_s^0$  decays in our data. Instead, we use the kinematically almost identical lepton plus displaced vertex sample to do a simultaneous fit and get the dilution information. This uses the assumption that the opposite side tagging dilution is independent of the same side  $B$  meson whether it is a  $B_s^0$  or  $B_d^0$ , as long as the two different  $B$  mesons have similar momentum spectra. Monte Carlo studies indicate this is true.

We have Owen Long's analysis [21] of the  $B_d^0$  oscillation frequency, which is kinematically identical to our reconstructed data. The  $p_t(B)$  spectrum of both Monte Carlo data are quite similar. The top plot of Figure 5.1 is the  $P_t$  of the  $B_d^0$  from Monte Carlo data from reference [21]. The bottom plot of Figure 5.1 is the  $P_t$  of the  $B_s^0$  from our Monte Carlo data. They look similar. Hence we can directly use opposite side flavor tagging results of reference [21] and apply them to our data. In the rest

of this chapter, we describe in detail the tagging methods[21] and parameterization.

### 5.1.3 The Raw Dilution

The raw dilution is defined by assuming opposite sign events are correctly tagged events and same sign events are mistagged events. Here opposite(same) sign means the trigger lepton charge and opposite side tagged flavor have the opposite(same) sign.

$$D_{raw} = \frac{N_{os} - N_{ss}}{N_{os} + N_{ss}} \quad (5.8)$$

The assumption that opposite sign events are correctly tagged events is not always correct because the same side trigger lepton could be from a  $B$  meson that oscillated before decaying, a sequential  $B$  decay, or a misidentified lepton etc. We introduce a parameter  $N_d$  which contains the integrated effect of all the same side mistags and relates the true dilution  $D$  to the raw dilution by

$$D = N_d \cdot D_{raw} \quad (5.9)$$

Note that it is always true that  $N_d > 1$  and  $D_{raw} < D$ . In  $B_d^0$  mixing analysis,  $\Delta m_d$  was fixed at world average and  $N_d$  was determined in the fit to get the value which we use for our analysis.

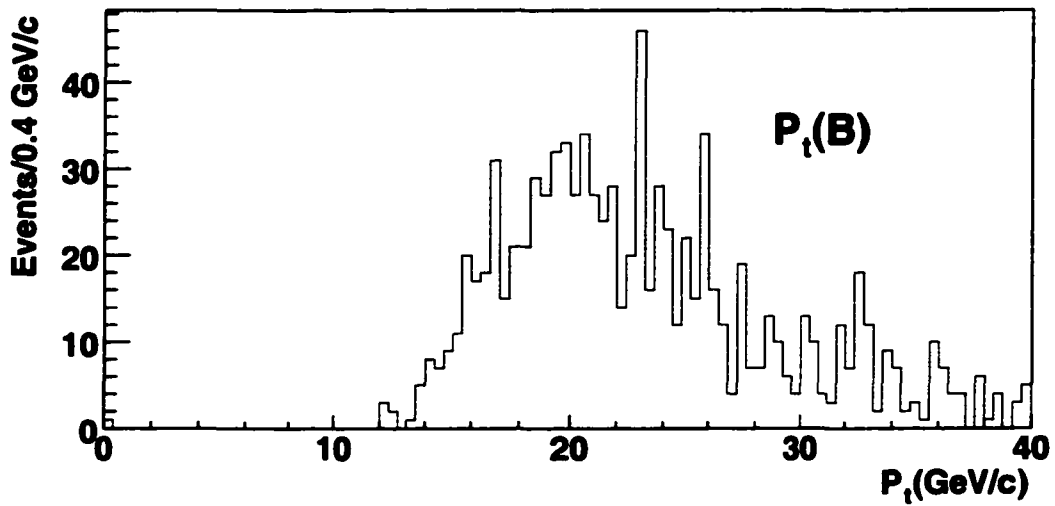
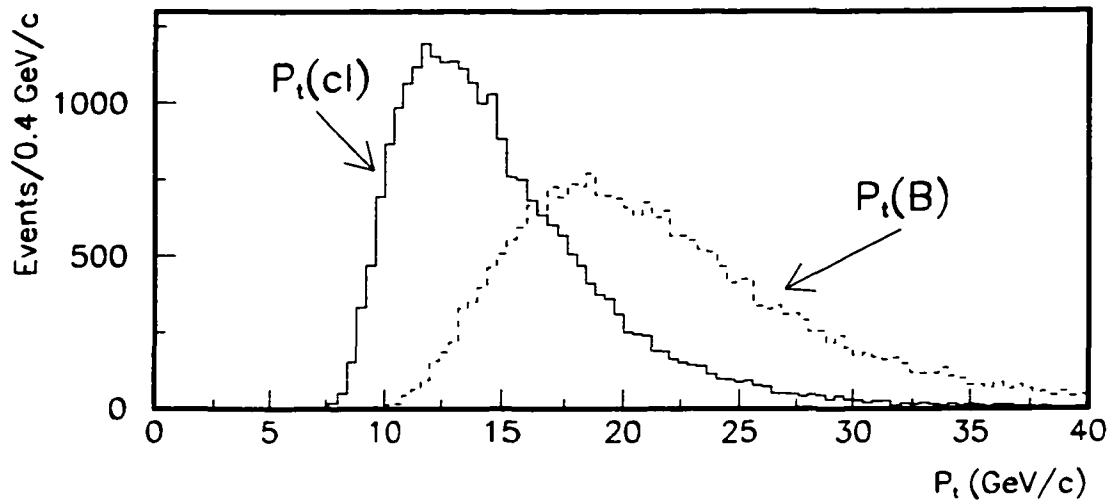


Figure 5.1: The plot on the top is the cluster and true  $P_t$  distributions for the Run 1b electron Monte Carlo data from Reference [21]. The plot on the bottom is the  $P_t$  distribution from our Run 1b electron Monte Carlo data.

## 5.2 The Secondary Vertex

Jet Charge Tagging uses a jet opposite to trigger lepton which is tagged as having a secondary vertex. In this section, we will describe in detail the determination of the primary vertex, the track-based jet algorithm, and how the secondary vertex tag is found. The tag is required to have  $L_{xy} > 0$  and be separated in  $\phi$  from the trigger lepton by at least 0.5 radians.  $L_{xy}$  is the transverse decay length, defined as the two dimensional ( $x$  and  $y$ ) distance between the primary and secondary vertices projected onto the jet axis. Track-based jets are formed using a cone clustering algorithm. Tracks with a significant impact parameter to the primary vertex are chosen in an attempt to form a secondary vertex. If a good vertex is found that is significantly displaced in the transverse direction from the primary vertex, the jet is used as a secondary vertex tagged jet.

### 5.2.1 The Primary Vertex

For each CDF data taking run (about 1 to 10 hours), the database has an averaged beam line position accurate to about  $35 \mu m$  in  $x$  and  $y$ . The beam has a slope with respect to  $z$  axis ( $\partial x/\partial z = 5 \mu rad$ ,  $\partial y/\partial z = -4.4 \mu rad$ ). The VTX provides us with the  $z$  position of the primary vertex for each event, which together with the run averaged beam line position, gives us the seed position for an event-by-event fit for the primary vertex location using tracks with SVX information.

Acceptable SVX tracks must have  $P_t > 0.4$  GeV/c, at least 3 SVX hits,  $|d_0| < 2.0$  cm, and  $z$  of the track within 5 cm of the primary vertex  $z$ . The trigger lepton track is excluded from the fit since it is from the  $B$  and not from the primary vertex. The first iteration of the fit uses all the acceptable tracks and the seed primary vertex location to find a common vertex. For each iteration, the track which contributes the most to the vertex  $\chi^2$  is removed, until no track contribution to the vertex  $\chi^2$  is more than 50.

### 5.2.2 Track-Based Jets

Track-based jets are formed for the opposite side jet charge tagging event using a cone clustering algorithm. All tracks passing the quality cuts listed in Table 5.1 are used. Tracks with  $P_t > 1$  GeV/c are considered as seeds for the jet. If two seeds are within  $\Delta R$  of 0.7 of each other, they are merged together. After merging all possible seeds, Tracks with  $P_t > 0.4$  GeV/c within  $\Delta R$  of 0.8 around the jet are added to the jet.

### 5.2.3 Secondary Vertex Finding

The secondary vertex finding algorithm is similar to the algorithm used for the top quark discovery at CDF [23] with some minor changes. The original method was designed for tagging the high  $P_t$   $B$  jets in  $t\bar{t}$  events and to minimize fake tags. The

Track Quality Cuts	
Requirement	Value
Max $\Delta z$ w.r.t P.V.	5 cm
Min track $P_t$	0.4 GeV/c
Max $ d_0 $	0.2 cm
Min CTC Exit Radius	130 cm
Min hits in good Stereo Layer	2
Min hits in good Axial Layer	5
Min good Stereo Layers	2
Min good Axial Layers	2

Table 5.1: Track quality criteria for track clustering from Reference [21]. The CTC exit radius is the radial position at which the track crosses the plane that defines the edge of the CTC in  $z$ .

modified method takes into account that  $B$  jets in our analysis are softer and emphasizes efficiency rather than purity.

The vertex finding algorithm is done in two passes. The first pass has relatively loose track criteria but requires a minimum of three tracks. The second pass has relatively tighter cuts but only requires a minimum of two tracks. The details of the two passes are:

### Pass 1

Tracks forming the secondary vertex are required to meet the following criteria:

- At least 2 axial CTC superlayers with at least 4 sense wire measurements.
- At least 2 stereo CTC superlayers with at least 2 sense wire measurements.

- **Good SVX clusters (hits), defined as:**
  - not shared by with any other track.
  - No bad strips.
  - No more than 3 strips in the cluster.
- **Not consistent with coming from a  $K_s^0$  or  $\Lambda$ .**
- **$|\Delta z| < 5$  cm from primary vertex.**
- **$|d_0| < 0.15$  cm with respect to primary vertex.**
- **$\chi^2/d.o.f < 6$  for track fit to SVX hits.**
- **Tracks with two SVX hits must have both hits in the first two or last two layers of silicon.**
- **For tracks with two SVX hits, both hits must be good hits and the track must have  $P_t > 1.5$  GeV/c.**
- **Tracks with three or four SVX hits must have at least one good hit and  $P_t > 0.5$  GeV/c.**
- **$|d_0/\sigma_{d_0}| > 2.5$ .**

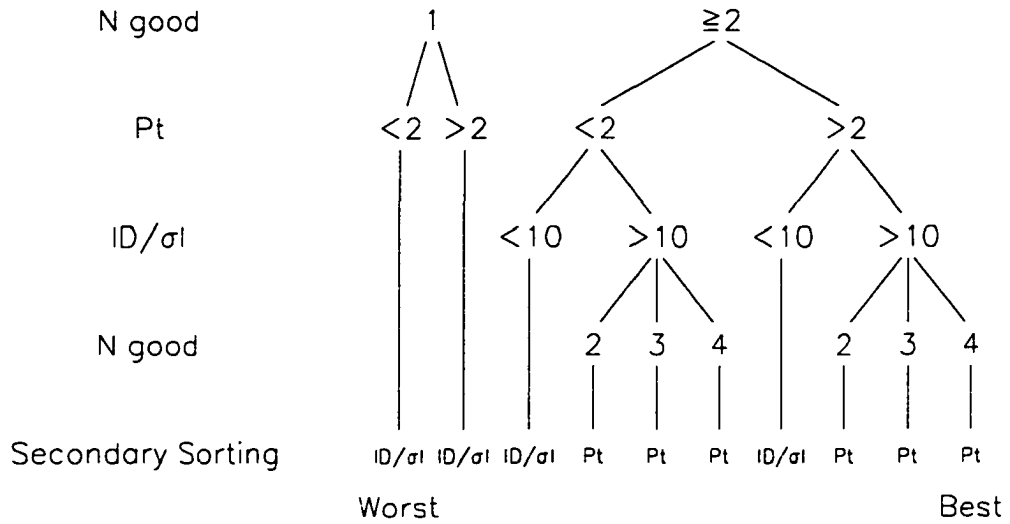


Figure 5.2: The ordering hierarchy for tracks to be considered in vertexing from Reference [21]. Tracks with high  $|d_0/\sigma_{d_0}|$ ,  $P_t$ , and a larger number of good SVX hits are considered first. Tracks in the same class are sorted by the Secondary Sorting variable.

Pass 1 needs 3 qualified tracks. If only two tracks pass the above criteria, then the third track must pass all above criteria except the last one ( $|d_0/\sigma_{d_0}| > 2.5$ ). This increases the acceptance for pass 1 at low  $L_{xy}$ .

The qualified tracks are marked based on the number of good SVX hits,  $P_t$ , and  $|d_0/\sigma_{d_0}|$ . Tracks with high  $|d_0/\sigma_{d_0}|$ ,  $P_t$ , and larger number of SVX hits are placed first in the list and are considered first in the vertexing. The ordering scheme is illustrated in Figure 5.2.

Starting with the best track in the list (beginning of the list), the tracks in the list are combined in pairs to form a seed vertex. The seed vertex must have one track with  $P_t > 2.0$  GeV/c. After the seed vertex is found, the algorithm looks for the so-called “attached tracks” in the list. The attached track must have its closest distance to the seed vertex in the  $x - y$  plane be within  $3\sigma$ . If at least one attached track is found, the seed vertex and the attached tracks are fit to form a common vertex. If a track has a  $\chi^2$  contribution of greater than 50 for the common vertex fit, it is dropped. The process is repeated until no track has a contribution to the  $\chi^2$  greater than 50.

At this point, if there are still three tracks in the vertex, two final requirements are applied to the vertex:  $L_{xy}/\sigma_{L_{xy}} > 2.5$  and  $L_{xy} < 2.5$  cm. The first requirement is to remove the fake vertices from randomly combined tracks. The reason for the second requirement is that a  $B$  hadron with  $P_t = 40$  GeV/c has a probability of less than 0.1% to travel more than 2.5 cm distance in the transverse plane before it decays. Most vertices with  $L_{xy} > 2.5$  cm are combinatoric mistakes or contain poorly measured tracks.

## Pass 2

If pass 1 fails, the algorithm goes to pass 2. The tracks must pass 1 track’s criteria plus the additional requirements listed below.

- No 2 hit tracks.
- $P_t > 1.0$  GeV/c.

- $|d_0/\sigma_{d_0}| > 3.0$ .
- 3 hit tracks must have at least 2 good hits.

Searching for the seed vertex and the final vertex is then the same as pass 1, except this time 2 tracks are required instead of 3 tracks. Also, two track vertices that are consistent with  $K_s^0 \rightarrow \pi^+\pi^-$  or  $\Lambda \rightarrow p^\pm\pi^\mp$  are removed.

### 5.3 Opposite Side Jet Charge Flavor Tagging

The jet charge flavor tagging was developed in the  $e^+e^-$  collider environment [24] [25] [26] [27] [28]. The jet charge is a momentum weighted average charge of the tracks associated with the jet, given by

$$Q_{jet} = \frac{\sum_i^n q_i \cdot (\vec{\mathbf{p}}_i \cdot \hat{\mathbf{a}})^\kappa}{\sum_i^n (\vec{\mathbf{p}}_i \cdot \hat{\mathbf{a}})^\kappa} \quad (5.10)$$

The sum is all over the tracks associated with the jet. The tracks and jet are defined in the track based jet algorithm. Here  $q_i$  is the charge of the track. The weight for this track is the momentum of this track along the jet axis direction.  $\kappa$  is a weighting factor emphasizes different parts of the momentum. A low(high)  $\kappa$  gives low(high) momentum tracks more weight.  $\kappa = 0$  gives all the track equal weight.  $\kappa = \infty$  gives all the weight to the highest momentum track. The jet charge is normalized such that it lies between -1 and 1. In this analysis,  $\kappa = 1$  is used.

In the following subsections, we will describe selection of the opposite-side  $b$  jet, the jet charge distributon, the dilution and statistical power of the opposite-side jet charge tag, and a test result of the charge tagging.

### 5.3.1 $b\bar{b}$ Production Topologies

The major  $b\bar{b}$  production mechanism at  $p\bar{p}$  collider at  $\sqrt{s} = 1.8\text{TeV}$  is direct production dominated by gluon-gluon fusion. Direct  $b\bar{b}$  production creates two  $b$  jets that are back-to-back in  $\phi$  and balanced in  $P_t$ . Since the  $b\bar{b}$  pair is produced from gluons within the  $p$  and  $\bar{p}$  which carry a variable fraction of the  $p$  or  $\bar{p}$  momentum, the  $b$  and  $\bar{b}$  jets are not necessarily back-to-back in  $\eta$ .

The other two higher order  $b\bar{b}$  production mechanisms are called flavor excitation and gluon splitting. Figure 5.3 shows representative Feynman diagrams for the three mechanisms. The flavor excitation process, for the events that pass our triggers, gives one  $b$  jet in the central (low  $\eta$ ) region. The other  $b$  in the event usually has a large longitudinal boost, putting it outside the tracking chamber acceptance. That is, the tracks from the  $b$  jet all have large  $|\eta|$  and exit the tracking chamber before traversing all of the sense wires. The gluon splitting process gives two  $b$  jets relatively close to each other in  $\eta$  and  $\phi$ . The  $b$  jets are balanced by a gluon jet on the opposite direction in  $\phi$ . The contribution to the total  $b\bar{b}$  cross section from higher order production mechanisms is comparable to that of direct production.

In real life, one can't distinguish between the different production processes. This means some of the time, the jet selected as the opposite side  $b$  in the event is actually from a gluon. There are two ways of dealing with this problem. If the event has one jet with secondary vertex tag which is not the trigger lepton jet, we use this secondary

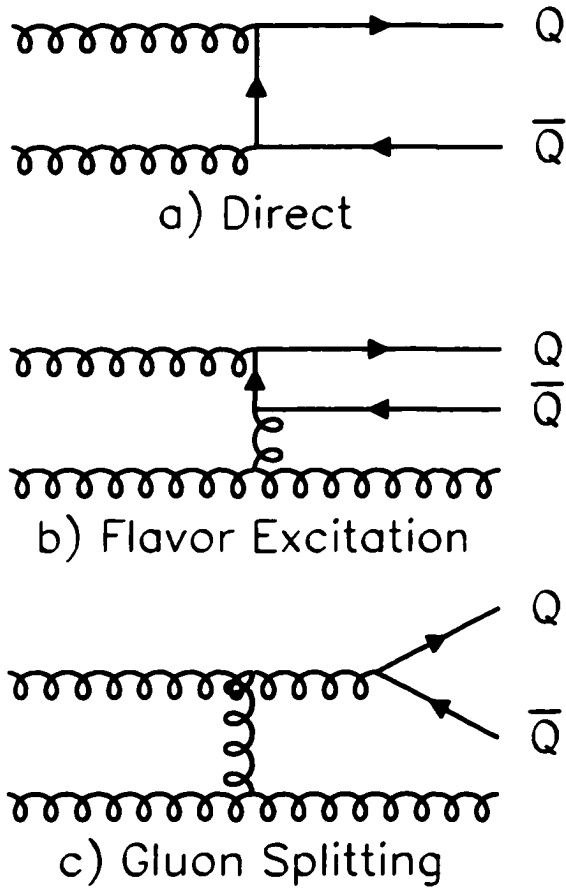


Figure 5.3: Representative Feynman diagrams for the three major  $b\bar{b}$  production mechanisms. Note that not all possible diagrams are shown.

vertex tagged jet to calculate the jet charge. If no jet other than the trigger lepton jet is secondary vertex tagged, the highest  $P_t$  jet opposite the trigger lepton in  $\phi$  is selected as the opposite  $b$  jet. The next subsection gives details of the opposite side jet selection and classification.

### 5.3.2 Opposite Jet Secondary Vertex Tagged(JST) and JQT

When we have an opposite side jet with a secondary vertex tag, we label it as a JST. If no opposite secondary vertex tag is found, it is labeled as a normal JQT. This distinction is made because jet charge tagging for JST tags has higher dilution than for normal JQT tags. However JST has lower efficiency, around 7% of the events are classified as JST events.

When there is no opposite secondary vertex tag found, the task to identify the second  $b$  jet is much more difficult. The only choice we have is based the jet topology alone. That is, based on only  $\phi$  and  $P_t$  information of the jet. So we have to assume the event is from direct  $b\bar{b}$  production, which yields 2 roughly back-to-back jets in  $\phi$ . The selection criteria is thus the opposite side  $b$  jet has a separation in  $\phi$  greater than  $\pi/2$  from the trigger lepton with a minimum transverse momentum 5.0 GeV/c. If there is more than one jet satisfying the criteria, we pick the one with highest momentum. JQT has a tagging efficiency around 42%, which is high but the dilution is low.

### 5.3.3 Jet Charge Distributions and Dilutions

The dilution of the jet charge tagging is a function of the jet charge. Figures 5.4 and 5.5 (from reference [21]) show jet charge distributions and the raw dilution as a function of the  $|Q_{jet}|$  for both  $e$  and  $\mu$  trigger data respectively. The raw dilution for each bin  $|Q_{jet}|$  is derived from the jet charge distribution at the two related bins of  $\pm|Q_{jet}|$  using Equation 5.8. We can see that  $D(raw)$  is roughly a linear function of  $|Q_{jet}|$  with exception of  $|Q_{jet}| = 1$ :

$$D(raw) = |Q_{jet}| \cdot D_{max}(raw) \quad (5.11)$$

This function is used to determine the jet charge tagging dilution on an event-by-event basis based on the  $|Q_{jet}|$ . For an event with  $|Q_{jet}| = 1$ , the raw dilution is used. The error on those parameters will be included in our study of systematic uncertainties.

Jet charge with a secondary vertex tag has a higher dilution than without a secondary vertex tag because the secondary vertex associated jet has an increased probability that the jet is indeed from the other  $B$  in the event. For those events where the jet charge is calculated from a gluon jet instead of the other  $B$  jet, we have zero dilution on average.

For each bin of  $|Q_{jet}|$ , we have  $D(raw)$  and the tagging efficiency  $\epsilon$ . Thus we have  $\epsilon D^2(raw)$  vs  $|Q_{jet}|$  distributions for the  $e$  and  $\mu$  triggers, which are shown in

## e Trigger

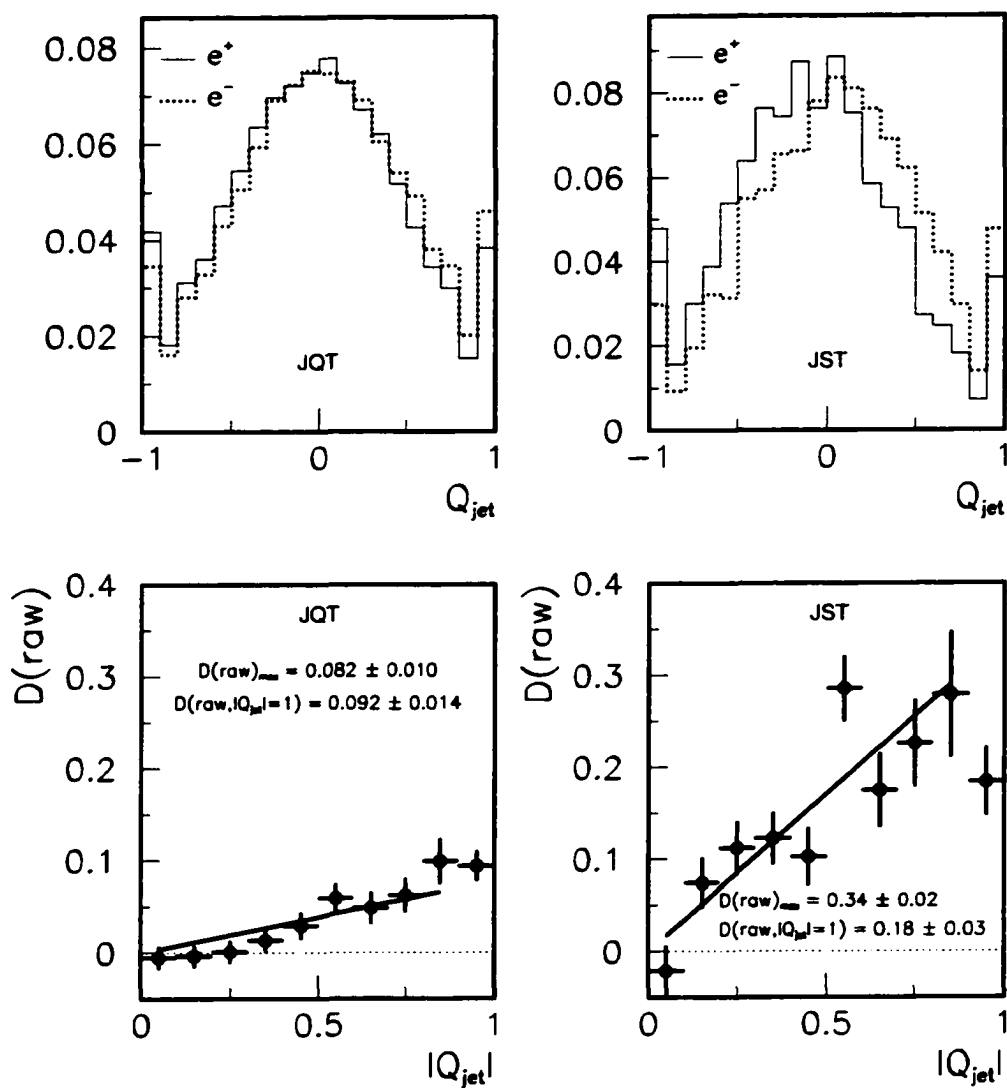


Figure 5.4: Jet charge and  $D(raw)$  vs  $|Q_{jet}|$  distributions for JQT and JST tagged events in the  $e$  trigger data from Reference [21].

## $\mu$ Trigger

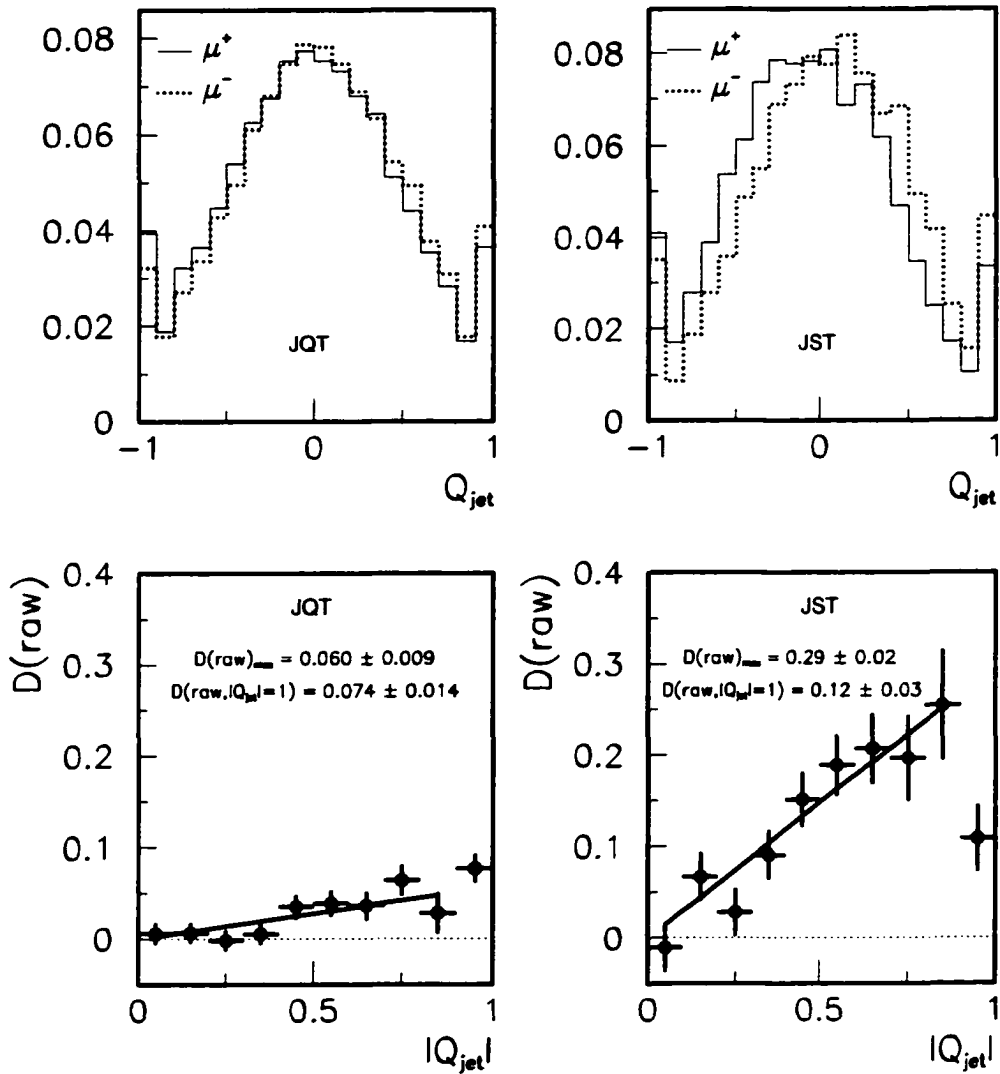


Figure 5.5: Jet charge and  $D(raw)$  vs  $|Q_{jet}|$  distributions for JQT and JST tagged events in the  $\mu$  trigger data from Reference [21]

## e Trigger

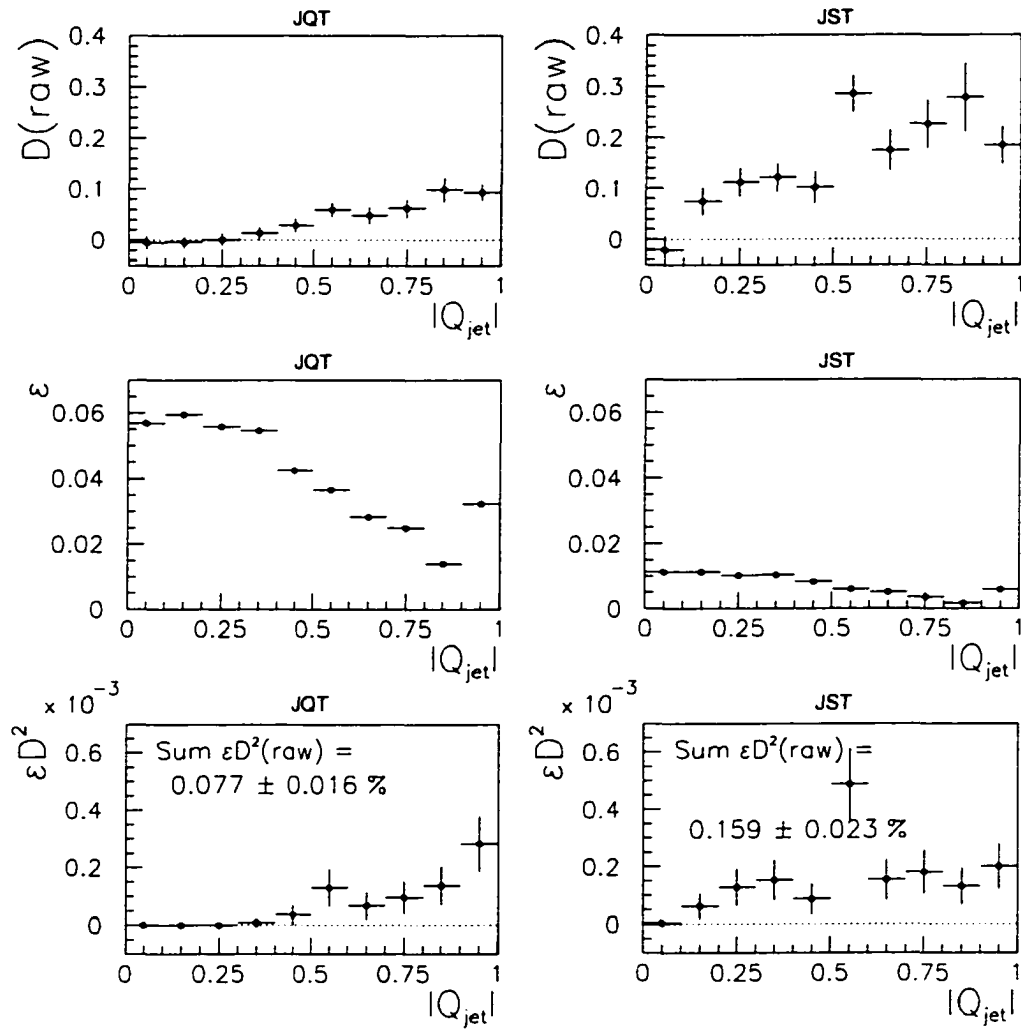


Figure 5.6: The raw dilution  $D(raw)$ , flavor tagging  $\epsilon$  and  $\epsilon D^2$  in bins of  $|Q_{jet}|$  for JQT and JST  $e$  trigger events from Reference [21].

## $\mu$ Trigger

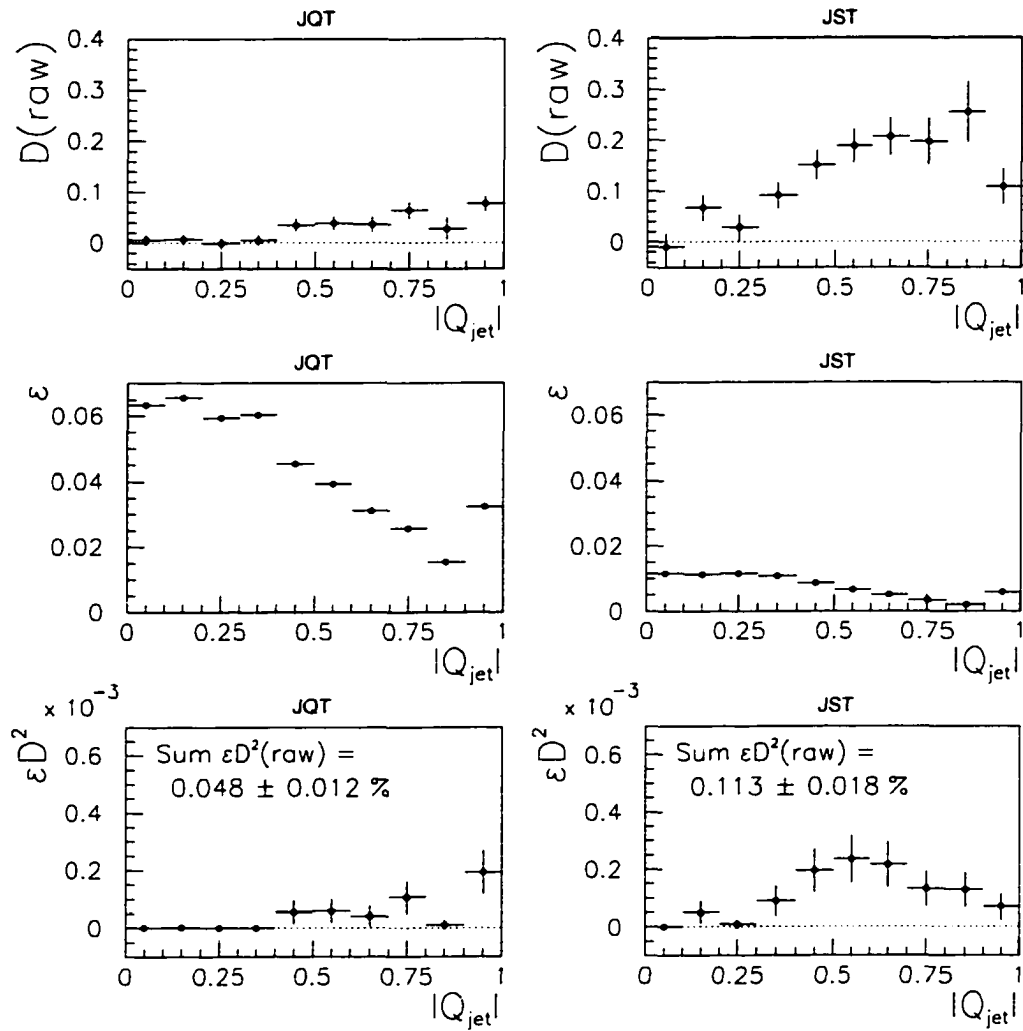


Figure 5.7: The raw dilution  $D(raw)$ , flavor tagging  $\epsilon$  and  $\epsilon D^2$  in bins of  $|Q_{jet}|$  for JQT and JST  $\mu$  trigger events from Reference [21].

Tag Type	$e$ Trigger		$\mu$ Trigger	
	Total $\epsilon$	$\Sigma_i \epsilon_i D_{raw}^2$	Total $\epsilon$	$\Sigma_i \epsilon_i D_{raw}^2$
JQT	$41.55 \pm 0.14\%$	$0.077 \pm 0.016\%$	$43.81 \pm 0.14\%$	$0.048 \pm 0.012\%$
JST	$7.44 \pm 0.08\%$	$0.159 \pm 0.023\%$	$7.66 \pm 0.07\%$	$0.113 \pm 0.018\%$
Combined	$48.99 \pm 0.16\%$	$0.236 \pm 0.028\%$	$51.47 \pm 0.16\%$	$0.161 \pm 0.022\%$

Table 5.2: Jet charge flavor tag  $\Sigma_i \epsilon_i D_{raw}^2$  where the sum is in bins of  $|Q_{jet}|$  from Reference [21].

Figures 5.6 and 5.7. The equivalent  $\epsilon D^2(raw)$  for the combination of the entire sample is  $\Sigma_i \epsilon_i D_i^2(raw)$ . The results of this calculation are also shown in the plots and summarized in Table 5.2. These values for  $\epsilon D^2(raw)$  need to be multiplied by  $N_B^2$  from the  $\Delta m_d$  fit to get the true flavor tag  $\epsilon D^2$ , which quantifies the statistical power of the flavor tagging method (see Equation 5.7).

### 5.3.4 Testing of JQT

From Reference [22] we have the jet charge tagging true dilution for electron trigger Monte Carlo data, that is,  $D = 0.51 \cdot Q_{jet}$ . This analysis used Pythia[29] 5.6 and QQ[30] 7.2. We generate events using the same Pythia and QQ versions as well as using the same options but reconstruct the same side signal from the channel  $B_s \rightarrow \ell D_s$  with  $D_s \rightarrow \phi\pi$ .

We control the decay of the  $B_s$  and turn on mixing of  $B^0$ 's, but not  $B_s$ . Thus, we know the flavor of  $B_s$  at production and can determine the tagging results. Then we can calculate the dilution and compare it to Reference [22]. We separate our data into 10 bins, calculate the dilution for each bin, and fit the ten points using a linear

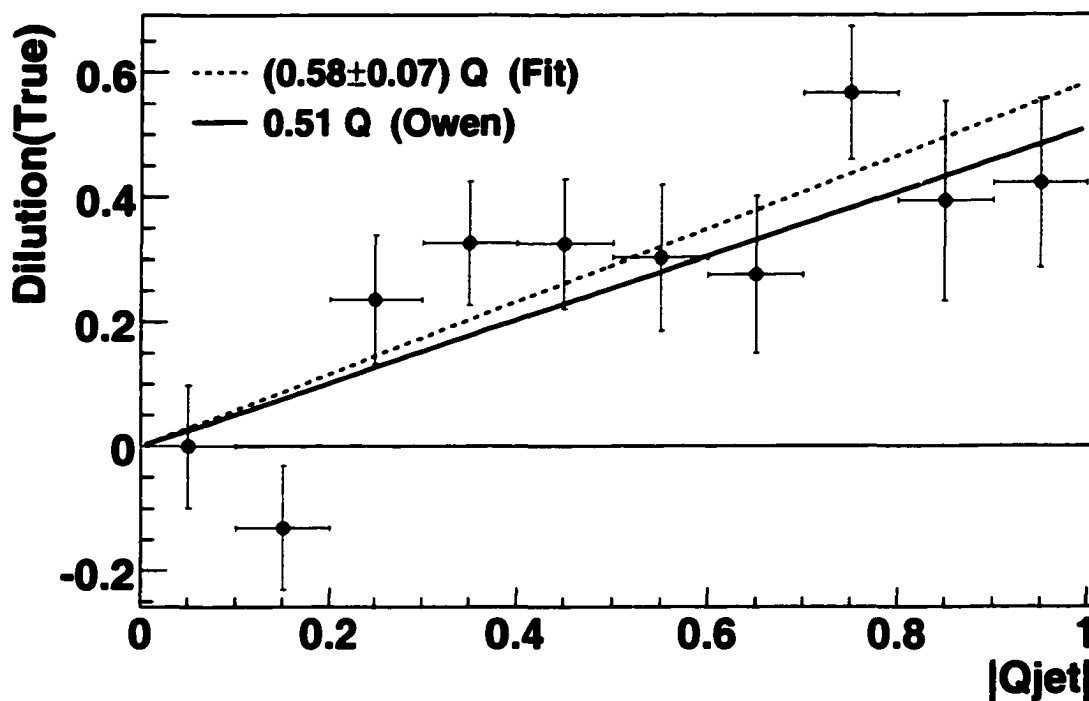


Figure 5.8: Testing of Owen's JQT tagging

fit, with the true dilution constrained to zero when  $|Q_{jet}| = 0$ . Figure 5.8 shows the comparison of Reference [22]'s result and ours, showing they are consistent. Note that we did not turn on the  $B_s$  mixing, but the effect of it is neglectable compared to the statistical errors we have.

This shows us that our flavor tagging algorithm works properly for our data sample. It also verifies that opposite side tagging is independent of the same side signal mode. This makes it possible to use the dilution results from Reference [22] for our analysis.

## 5.4 Opposite Side Soft Lepton Flavor Tagging

The opposite side  $B$  can decay semileptonically, just as the same side  $B$  decays semileptonically. The sign of the lepton from the opposite side  $B$ 's semileptonic decay can be used as a tag. CDF developed low  $p_T$  electron and muon  $b$  tagging for its top discovery [23] [31]. This analysis uses the same algorithms with minor changes to reflect the less energetic  $B$  events.

Before we discuss more details of the soft lepton tagging, we first cover the details of the removal of the soft electrons consistent with the conversion., which is one of the selection criteria for soft electron tagging.

### 5.4.1 Conversion Soft Electron Removal

A small fraction of the soft electrons are from photon conversions ( $\gamma \rightarrow e^+e^-$ ), which need to be eliminated. The conversions are identified by searching for an opposite charge track that forms a good vertex with the soft lepton. That track is referred to as the conversion partner. The track of the soft lepton and the track of the conversion partner must be parallel to each other at the vertex point within the detector's resolution.

Two sets of selection criteria, shown in Table 5.3, were used to evaluate the efficiency of the conversion finding algorithm for real conversion electrons. The "loose" criteria were chosen to be fully efficient in identifying real conversion electrons, but it

Conversion Finding Cuts		
Parameter	Tight	Loose
$r - \phi$ Separation at point of tangency	0.2 cm	0.5 cm
Difference of cotangents	0.03	0.06
$z$ Mismatch at point of tangency	2.0 cm	5.0 cm
Conversion radius	-5 cm to 50 cm	-10 cm to 50 cm
$\Delta\phi$ at radius of conversion	0.01	0.05
Pointing residual to origin	1.0 cm	1.0 cm

Table 5.3: Tight and loose cuts used in conversion finding from Reference [21].

also labels many non-conversion electrons as conversion electrons. The “tight” criteria are a compromise between reducing the overall efficiency and keeping the efficiency for real conversions high and are used in our analysis.

The  $dE/dx$  spectrum of the conversion partner is used to measure the number of real and fake conversions. The number of sense wire measurements used in the  $dE/dx$  measurement ( $N_{CTC}$ ) is required to be at least 25 to ensure a quality  $dE/dx$  measurement. We also require the conversion partner to be consistent with the electron hypothesis with the cut below

$$\frac{dE/dx_{meas} - dE/dx_{pred}(e)}{\sigma_{dE/dx}} > -2.0 \quad (5.12)$$

#### 5.4.2 SLT Selection Criteria and Parameterization

As we just discussed, conversion electrons are removed as soft electron candidates. The soft lepton and the trigger lepton are required to have an invariant mass of more than 5 GeV/c. The soft lepton must not be in the trigger lepton jet, which means a

separation of  $\Delta R > 0.7$ . This also eliminates leptons from sequential decays:  $b \rightarrow \ell \nu c$ ;  $c \rightarrow \ell \nu s$ .

An important quantity that distinguishes direct decay soft leptons from sequential decay leptons, charm decays leptons, and misidentified leptons is  $P_t(\text{rel})$ .  $P_t(\text{rel})$  is defined as the component of the soft lepton momentum transverse to the axis of the jet that it is associated with, where the lepton is not included in the calculation of the jet axis. Statistically, leptons from the sequential decays, charm decays, and misidentification have smaller  $P_t(\text{rel})$  than direct decay leptons.

The SLT raw dilution is a function of  $P_t(\text{rel})$  in the same way that the jet charge raw dilution is a function of  $|Q_{jet}|$ . Figure 5.9 (from Reference [21]) shows the soft lepton raw dilution as a function of  $P_t(\text{rel})$  for the  $e$  and  $\mu$  trigger data. The function has the form

$$D_{raw}(P_t(\text{rel})) = A \cdot (1 - e^{-P_t(\text{rel})+B}) \quad (5.13)$$

where the parameters  $A$  and  $B$  are determined for each trigger type and each of the soft lepton types. We classify the soft lepton as an electron or one of four types of muon depending on which muon detectors are used. If the soft lepton is isolated, then we do not have a  $P_t(\text{rel})$  measurement. The average  $D_{raw}$  for events which do not have the  $P_t(\text{rel})$  measurement is used. These points are shown in Figure 5.9 as the negative  $P_t(\text{rel})$  bin. The dashed curves are the variations on  $D_{raw}(P_t(\text{rel}))$  for

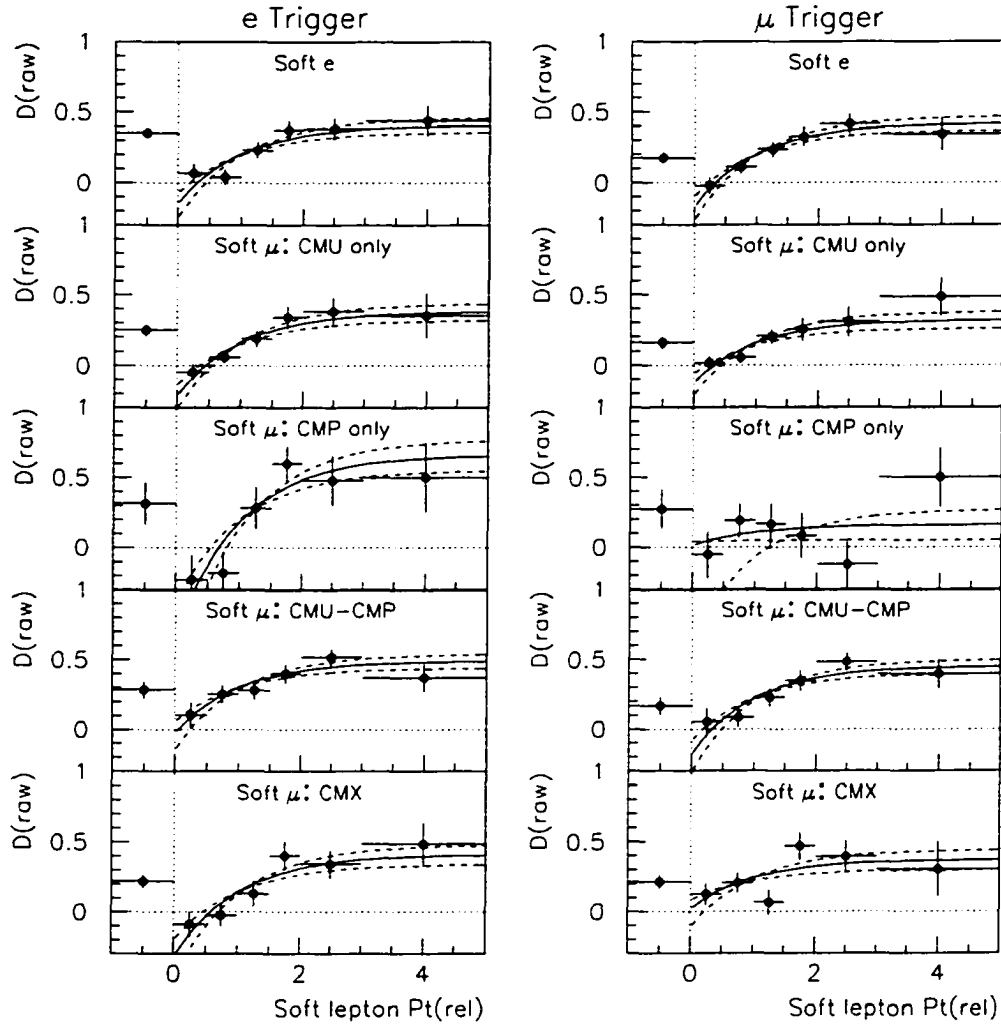


Figure 5.9: The soft lepton raw dilution as a function of the soft lepton  $P_t(\text{rel})$  from the analysis of Reference [21]. The data are divided into the 5 soft lepton types for the  $e$  and  $\mu$  triggers. The negative  $P_t(\text{rel})$  is for events where the soft lepton is isolated and does not have a  $P_t(\text{rel})$  measurement. The solid line is used in the event-by-event dilution prediction. The dashed lines are used for the systematic studies.

SLT Type	$e$ Trigger		$\mu$ Trigger	
	Total $\epsilon$	$\Sigma_i \epsilon_i D_i^2(\text{raw})$	Total $\epsilon$	$\Sigma_i \epsilon_i D_i^2(\text{raw})$
Soft $e$	$1.59 \pm 0.04$ %	$0.136 \pm 0.021$ %	$1.56 \pm 0.03$ %	$0.074 \pm 0.015$ %
Soft $\mu$ , CMU	$1.71 \pm 0.04$ %	$0.069 \pm 0.015$ %	$1.62 \pm 0.04$ %	$0.041 \pm 0.011$ %
Soft $\mu$ , CMP	$0.20 \pm 0.01$ %	$0.028 \pm 0.009$ %	$0.22 \pm 0.01$ %	$0.009 \pm 0.005$ %
Soft $\mu$ , CMUP	$1.08 \pm 0.03$ %	$0.125 \pm 0.020$ %	$0.86 \pm 0.03$ %	$0.064 \pm 0.013$ %
Soft $\mu$ , CMX	$0.86 \pm 0.03$ %	$0.044 \pm 0.012$ %	$0.80 \pm 0.02$ %	$0.045 \pm 0.011$ %
All Types	$5.44 \pm 0.07$ %	$0.402 \pm 0.036$ %	$5.06 \pm 0.06$ %	$0.233 \pm 0.026$ %

Table 5.4: Soft lepton flavor tag  $\Sigma_i \epsilon_i D_i^2(\text{raw})$  where the sum is in bins of soft lepton  $P_t(\text{rel})$  from Reference [21].

Values for $N_D$ , $\Delta m_d$ fixed to $0.47 \text{ ps}^{-1}$		
Flavor Tag	$e$ Trigger	$\mu$ Trigger
JQT	$1.88 \pm 0.20 \pm 0.15$	$2.41 \pm 0.29 \pm 0.39$
JST	$1.76 \pm 0.20 \pm 0.09$	$2.14 \pm 0.33 \pm 0.25$
SLT	$1.72 \pm 0.08 \pm 0.11$	$2.01 \pm 0.13 \pm 0.22$

Table 5.5: Values for  $N_D$  factors, where  $\Delta m_d$  has been fixed to the world average ( $0.47 \text{ ps}^{-1}$ ) from Reference [21]. The first error is statistical, the second is systematic. Those numbers are used for our dilution calibration.

the systematic studies. For those events which do not have a  $P_t(\text{rel})$  measurement the statistical error on the raw dilution is used for the variation in the systematic studies.

The statistical power of the soft lepton flavor tag is estimated from  $\Sigma_i \epsilon_i D_i^2(\text{raw})$  where the sum is in bins of soft lepton  $P_t(\text{rel})$ . The values of  $\Sigma_i \epsilon_i D_i^2(\text{raw})$  are summarized in Table 5.4.

## 5.5 The Dilution Normalization $N_D$

For the correction from raw dilution to true dilution,  $N_d$ , we use the results from Reference [21] when  $\Delta m_d$  was fixed to the world average and  $N_d$  was determined (see table 5.5). The statistical plus systematic uncertainties in the table are used in our systematic studies. The statistical power of the flavor taggers we used was measured by Reference [21] to be

- Jet Charge :  $\epsilon D^2 = 0.78 \pm 0.12(\text{stat}) \pm 0.09(\text{sys})\%$
- Soft Lepton :  $\epsilon D^2 = 1.07 \pm 0.09(\text{stat}) \pm 0.10(\text{sys})\%$

In the event-by-event fitting for our analysis, we use the SLT, if present. If there is no SLT and there is a JST, we use the JST. If there is no SLT and no JST, and there is a JQT, we use the JQT. Otherwise, we treat it as an untagged event.

# Chapter 6

## The Fitting Method

### 6.1 K-factor Distribution

The lifetime of  $B_s^0$  is related to the decay length of  $B_s^0$  by the equation

$$ct \equiv \frac{L}{\beta\gamma} = L_{xy}(B_s^0) \frac{m(B_s^0)}{p_T(B_s^0)} \quad (6.1)$$

When the  $B_s^0$  decays semi-leptonically, it can not be fully reconstructed and thus we are unable to accurately measure  $p_T(B_s^0)$ . We use  $p_T(\ell^+ D_s^-)$  as a best approximation. We define a correction factor  $K$  as

$$K = \frac{p_T(\ell^+ D_s^-)}{p_T(B_s^0)} \quad (6.2)$$

and introduce the pseudo proper decay length  $x$

$$x = L_{xy}(B_s^0) \frac{m(B_s^0)}{p_T(\ell^+ D_s^-)} = ct \frac{1}{K} \quad (6.3)$$

The correction factor  $K$  is determined from Monte Carlo. We have generated approximately 30 million semi-leptonic  $B_s^0$  decays for each decay mode,  $\phi\pi$  and  $K^{*0}K$ , using BGENERATOR[32] with a minimum  $p_T(b)$  of 9 GeV and apply our standard kinematical cuts. We have forced  $B_s^0$  decays to  $\ell^+\nu D_s^{(*)-}$  and  $D_s^- \rightarrow \phi\pi^-$  or  $K^{*0}K^-$ , with  $\phi \rightarrow K^+K^-$  and  $K^{*0} \rightarrow K^+\pi^-$ . We use the branching ratios from the version 9.1 of CLEO Monte Carlo QQ[30] decay table. The fractions are

$$Br(B_s^0 \rightarrow D_s^- \ell^+ X) = 1.8\% \quad (6.4)$$

$$Br(B_s^0 \rightarrow D_s^{*-} \ell^+ X) = 4.6\%$$

We use a cut of  $p_T(\ell) > 6.0$  GeV/c in generating the final  $K$  factor distribution histogram. Figures 6.1 and 6.2 show the  $K$  factor distribution histograms for  $\phi\pi$  and  $K^{*0}K$  modes. Figures 6.3 and 6.4 show the pull distribution histograms of the decay length for  $\phi\pi$  mode and  $K^{*0}K$  mode.

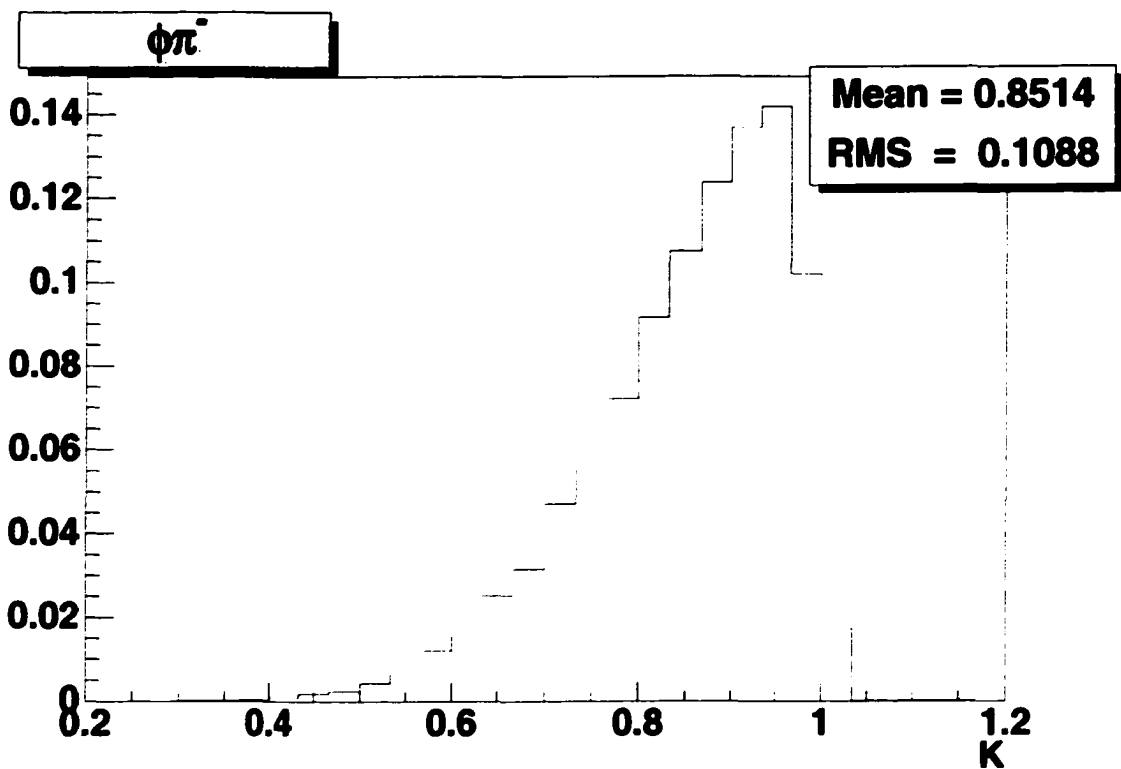


Figure 6.1: Monte Carlo generated  $K$ -factor distribution for  $\phi\pi$  mode, where  $K = \frac{p_T(\ell^+ D_s^-)}{p_T(B_s^0)}$ .

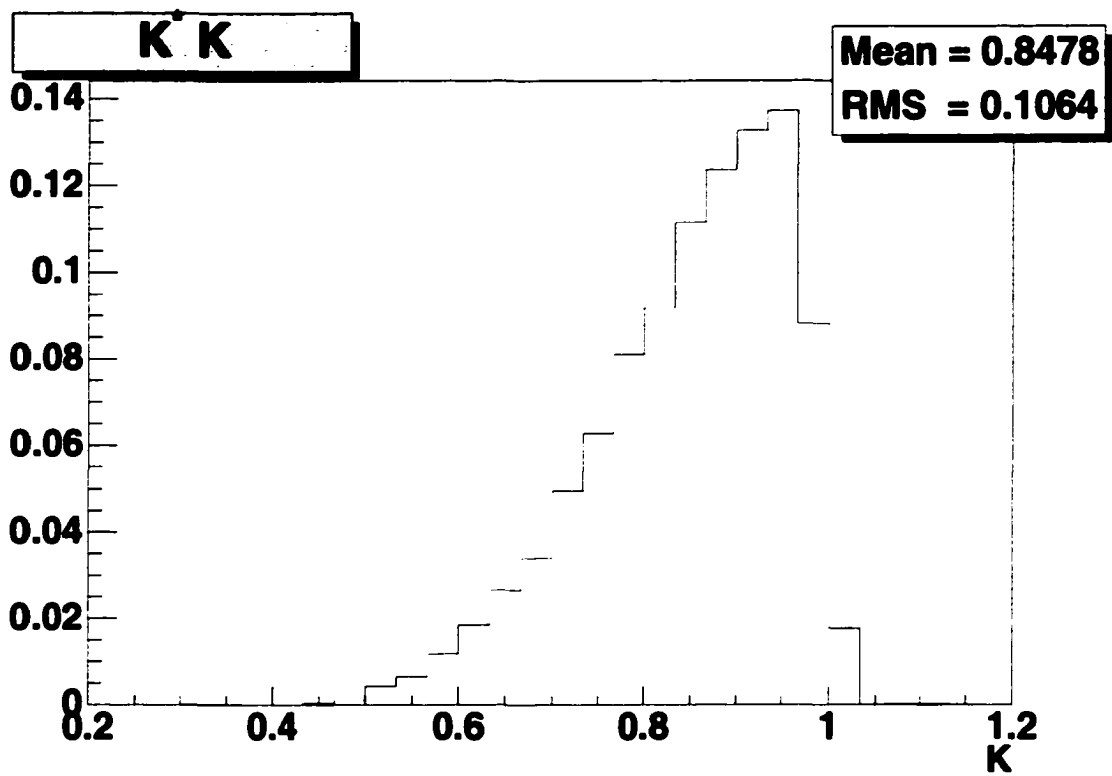


Figure 6.2: Monte Carlo generated  $K$ -factor distribution for  $K^{*0}K$  mode.

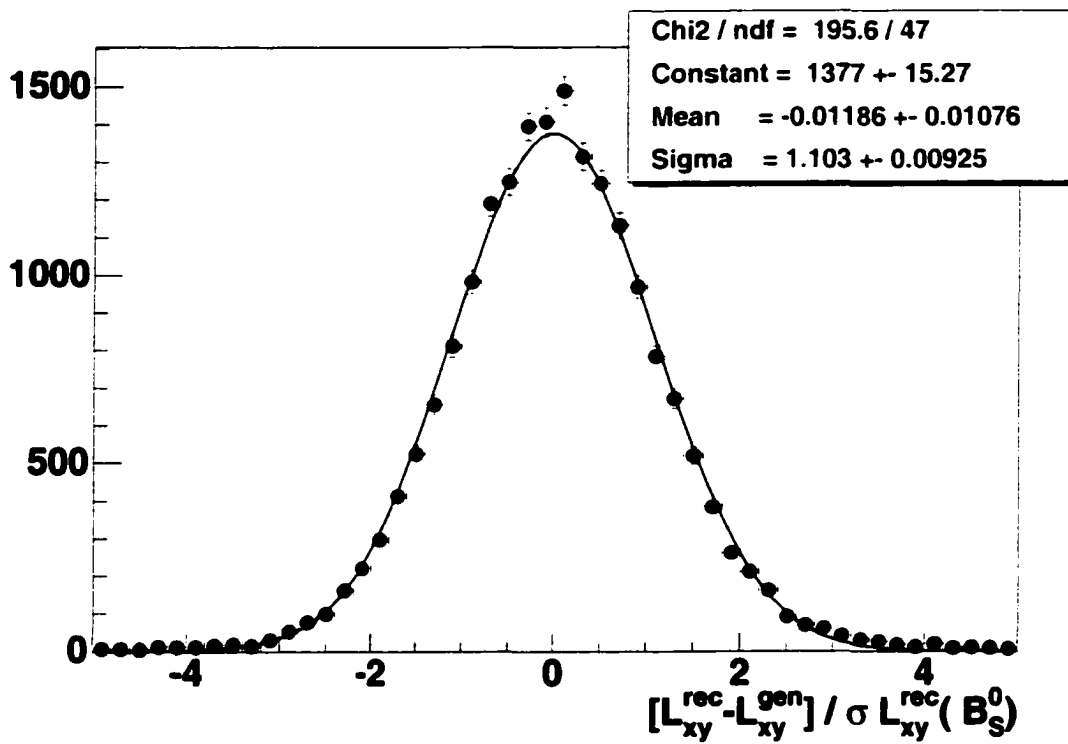


Figure 6.3: Monte Carlo generated  $L_{xy}$  pull for  $\phi\pi$  mode with a single Gaussian fit superimposed.

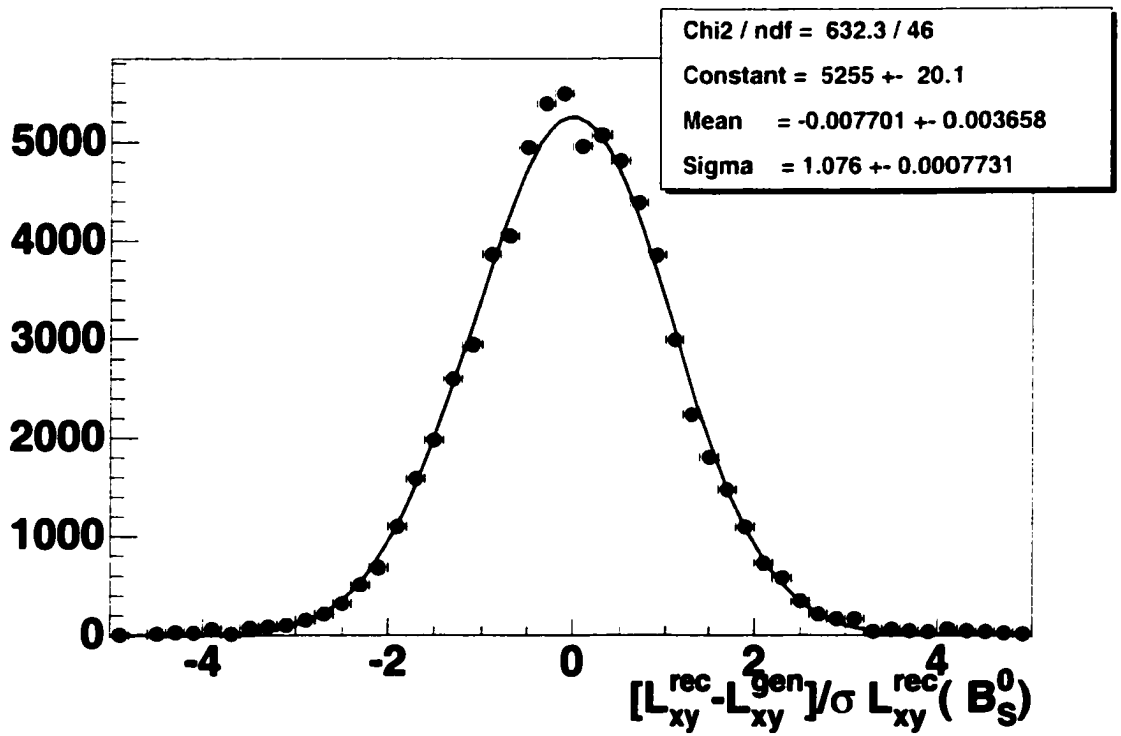


Figure 6.4: Monte Carlo generated  $L_{xy}$  pull for  $K^{*0}K$  mode.

## 6.2 Fitting Function

### 6.2.1 Lifetime Probability Density Function

The proper decay time probability density function (p.d.f.) is

$$P(ct, c\tau) = \frac{1}{c\tau} \exp\left(-\frac{ct}{c\tau}\right) \cdot \theta(ct) \quad (6.5)$$

Where  $\theta(ct)$  is the step function, which is 0 when  $ct < 0$  and is 1 when  $ct \geq 0$ .

Since we can not measure the decay length with perfect resolution, and further, since the  $p_T$  of the  $B_s^0$  is not fully reconstructed in our case, we have to use the pseudo proper decay time  $x$  we just introduced. Thus we have to convolute the p.d.f with the Gaussian decay length resolution and with the  $K$ -factor distribution function  $D(K)$ . So the actual proper decay time p.d.f. for the signal becomes

$$F_{sig}(x) = \frac{K}{c\tau} \exp\left(-\frac{Kx}{c\tau}\right) \otimes G(x, s \cdot \sigma) \otimes D(K), \quad (6.6)$$

where  $\otimes$  denotes a convolution.

The resolution term has a scale factor  $s$  since we may under or over estimate the decay length resolution, and in this document we omit the term  $\theta(x)$ . We do not have an analytical  $K$ -factor distribution function, but we have the histogram from the Monte Carlo data. So we first convolute the p.d.f with a Gaussian analytically and get the Gaussian smeared p.d.f., and then the Gaussian smeared p.d.f is convoluted

with the  $D(K)$  numerically.

There is also background having prompt, positive long-lived exponential, and negative long-lived exponential components.

$$F_{bkg}(x) = (1 - f_- - f_+)G(x, s \cdot \sigma) \quad (6.7)$$

$$+ \frac{f_+ K}{\lambda_+} \exp\left(-\frac{Kx}{\lambda_+}\right) \otimes G + \frac{f_- K}{\lambda_-} \exp\left(\frac{Kx}{\lambda_-}\right) \otimes G$$

Here  $\lambda_+(\lambda_-)$  is the lifetime for positive(negative) exponential background, and  $f_+(f_-)$  is the fraction of each, and the fraction of the prompt background is  $1 - f_+ - f_-$ . The positive and negative exponential are also convoluted with the Gaussian decay length resolution.

Once we have the signal and background p.d.f., we need to combine them to make the whole p.d.f in order to fit the  $B_s^0$  lifetime data. From the  $D_s$  mass plot we can see the probability fraction of signal over background changes with  $D_s$  mass, so we introduce  $D_s$  mass dependence into the probability density function. The mass p.d.f for the signal is a normalized Gaussian

$$M_{sig}(m) = \frac{1}{\sqrt{2\pi}\sigma_M} \exp\left(-\frac{(m - m_D)^2}{2\sigma_M^2}\right) \quad (6.8)$$

Here  $m_D$  is the mean of the  $D_s$  mass,  $\sigma_M$  is the width of the Gaussian for the  $D_s$ ,

mass signal. The mass space p.d.f for the combinatorial background is chosen as a normalized exponential to fit the shape of the data, giving

$$M_{bkg}(m) = \frac{\exp(-\frac{m}{\tau_M})}{\tau_M \left( \exp(-\frac{m_L}{\tau_M}) - \exp(-\frac{m_H}{\tau_M}) \right)}.$$

Here  $\tau_M$  is the lifetime of this exponential.  $m_L$  is the low end of the  $D_s$  mass range in the fit. For  $\phi\pi$  mode, we choose 1.9 GeV, in order to avoid the Cabibbo-suppressed decay  $D^- \rightarrow \phi\pi^-$ . For  $K^{*0}K$ , we choose 1.75 GeV.  $m_H$  is the high end of the fitted  $D_s$  mass. We choose 2.2 GeV for  $\phi\pi$  and 2.18 GeV for  $K^{*0}K$ .

The final  $B_s^0$  lifetime p.d.f is

$$\mathcal{F} = (1 - f_b)M_{sig}(m)F_{sig}(x) + f_b M_{bkg}(m)F_{bkg}(x) \quad (6.9)$$

Here  $f_b$  is the fraction of background in the whole  $D_s$  mass region used in the fit.

### 6.2.2 Mixing P.D.F and the Unbinned Likelihood Function

Once we have the p.d.f for the  $B_s^0$  lifetime, we are ready to build the p.d.f. for the  $B_s^0$  mixing. For each event, the tag is

- RS: right sign event
- WS: wrong sign event

- NT: untagged event

If it is an untagged event, the mixing p.d.f. is the same as the lifetime p.d.f. If it is a tagged event,

$$F_{sig}^{rs,ws}(x) = \frac{K}{2c\tau} e^{-\frac{Kx}{c\tau}} \left(1 \pm AD \cos \frac{\Delta m K x}{c}\right) \otimes G \otimes D(K) \quad (6.10)$$

$$F_{bkg}^{rs,ws}(x) = \begin{cases} f_{rs} \cdot F_{bkg}^{nt}(x) & \text{if right sign} \\ (1 - f_{rs}) \cdot F_{bkg}^{nt}(x) & \text{if wrong sign} \end{cases}$$

We now have several more fit parameters. Let me summarize them, including the lifetime fit parameters.

$f_{bkg}$  is the background fraction over whole region

$\tau$  is the lifetime of  $B_s^0$

$s$  is the overall scale factor to account for under- or over-estimates of the error

$D$  is the dilution,  $D = 1 - 2W$ ,  $W$  is the mistag rate

$A$  is the amplitude, it is for the amplitude fit, discussed later.

$f_+$ ,  $f_-$  are the fractions of positive and negative lifetime backgrounds

$\lambda_+$ ,  $\lambda_-$  are the lifetimes of those backgrounds

$f_{rs}$  is the fraction of right sign for the background

$m_D$  is the mass of the  $D_s$ ,

$\sigma_M$  is the Gaussian  $\sigma$  for the mass of  $D_s$  signal

$\tau_D$  is the lifetime of the mass of  $D_s$  combinatorial background

Now we have the final mixing p.d.f

$$\mathcal{F}^{tag} = (1 - f_b) M_{sig}(m) F_{sig}^{tag}(x) + f_b M_{bkg}(m) F_{bkg}^{tag}(x). \quad (6.11)$$

And the unbinned likelihood function for the mixing is

$$-\ln \mathcal{L} = -\sum_{i=1}^{N_{nt}} \ln \mathcal{F}^{nt}() - \sum_{i=1}^{N_{rs}} \ln \mathcal{F}^{rs}() - \sum_{i=1}^{N_{ws}} \ln \mathcal{F}^{ws}()$$

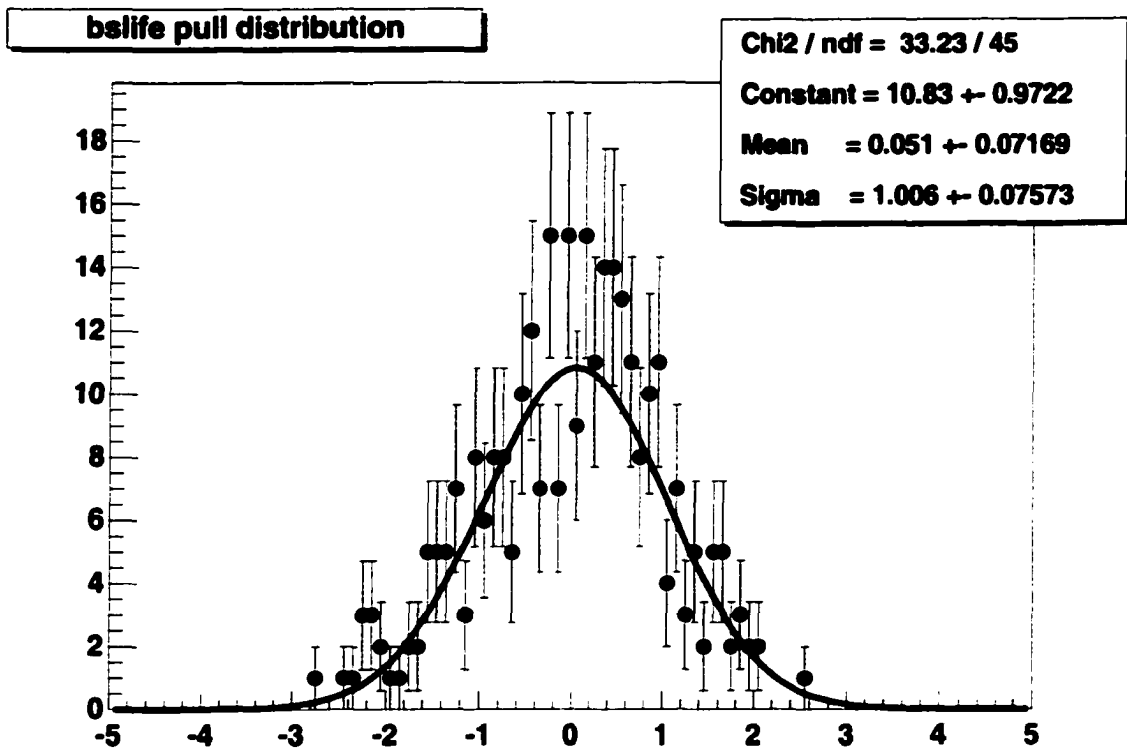


Figure 6.5: Pull distribution of  $B_s^0$  lifetime from a simple toy Monte Carlo.

### 6.3 Test of the Fitters

We have built a fitting program, a Fit Framework based on ROOT[33] which can do many fitting processes. We have tested this program extensively on simple Monte Carlo data. For example, figure 6.5 is the pull histogram of the  $B_s^0$  lifetime, which is one of our fit parameters. We have done extensive studies of the pull distribution for each parameter and have not found any significant bias on the pulls.

We are using the amplitude fit method[34] in an attempt to find a  $B_s^0$  mixing limit. The amplitude fit method is a standard method in  $B_s^0$  mixing limit studies and

can easily be used to combine different results. It is basically a Fourier transformation from proper-time space into frequency space. The way to do the amplitude fit is to vary only amplitude but fix all the other parameters at nominal values. We set  $\Delta m$  at different fixed values, and try to fit for the amplitude. If there is no mixing at a certain  $\Delta m$ , we should get fitted amplitude consistent with 0. If there is mixing at a certain  $\Delta m$ , then the amplitude fit should return a amplitude consistent with 1 at that  $\Delta m$ . A value of  $\Delta m$  can be excluded for mixing at 95% confidence level if  $A + 1.645\sigma_A < 1$ . The lower limit on  $\Delta m$  is defined as the highest  $\Delta m$  value below which all values of  $\Delta m$  are excluded.

Figure 6.6 is a simple Monte Carlo amplitude scan result. It shows how a positive mixing result will look like for an input of  $\Delta m_s = 9\text{ps}^{-1}$  with high statistics and good resolution. An amplitude fit of simple Monte Carlo data which is scaled corresponding to CDF data for our channel is shown in figure 6.7. This indicates the possibility of setting a limit for  $\ell D_s$  channel. These simple Monte Carlo experiments are also a good way to test our fitter.

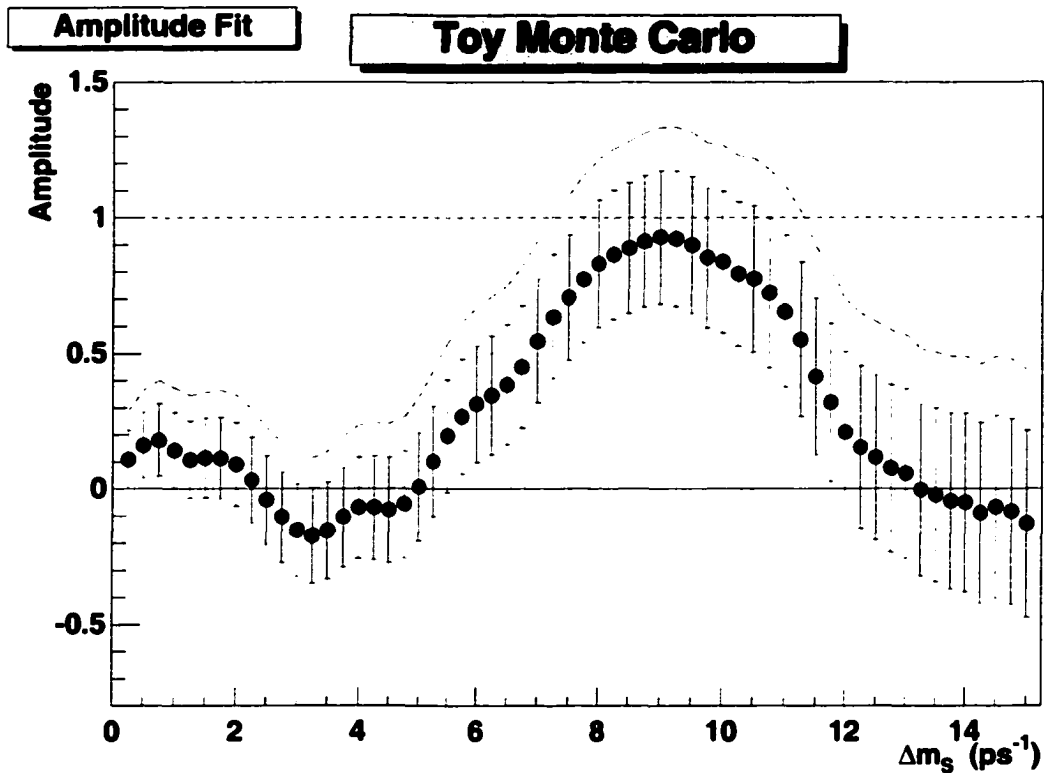


Figure 6.6: Toy Monte Carlo amplitude fit with input  $\Delta m_s = 9\text{ps}^{-1}$ , resolution = 0.0012 cm, 10000 events. The dashed line corresponds to  $A + 1.645\sigma_A$  with statistical uncertainties. The values of  $\Delta m_s$  for which the dashed line is less than one are excluded at 95% confidence level. We can see there is mixing at  $\Delta m_s = 9\text{ps}^{-1}$ .

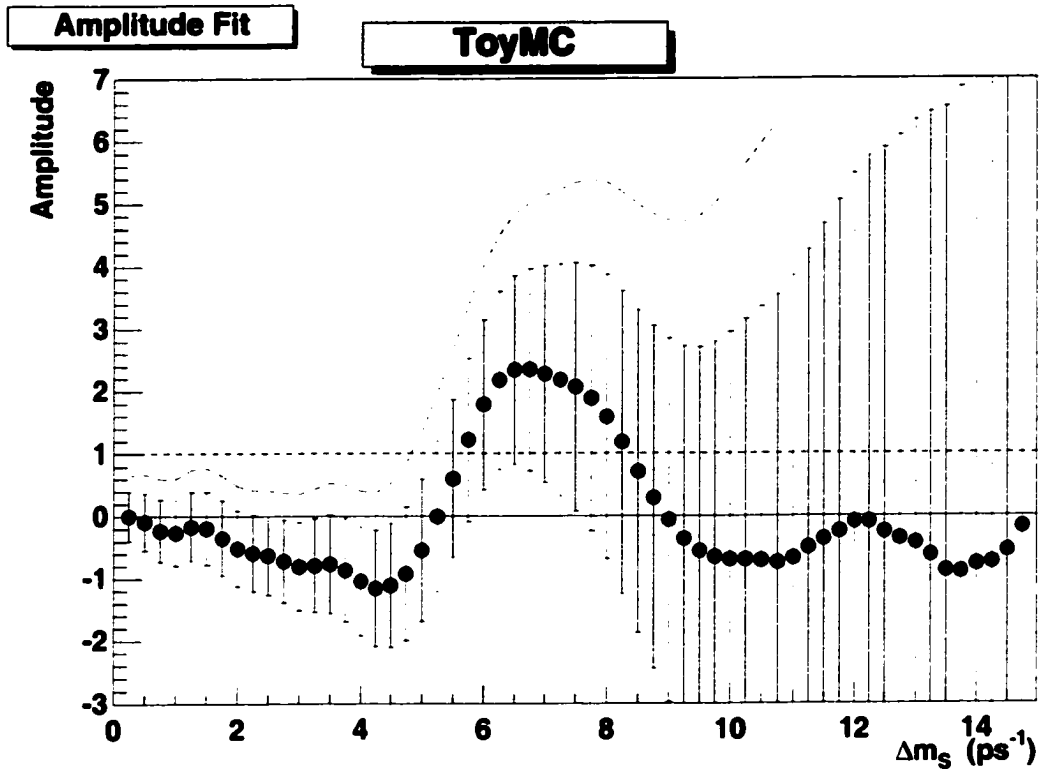


Figure 6.7: Toy Monte Carlo amplitude fit with input  $\Delta m_s = 20\text{ps}^{-1}$ , resolution = 0.0078 cm, 769 events with the appropriate tagging efficiency and dilution. This is trying to simulate the CDF  $\ell D_s$  channel data.

# Chapter 7

## Determination of the Lower Limit on

$$\Delta m_s$$

### 7.1 $B_s^0$ Lifetime Fit

Before we do a final fit for the limit on  $\Delta m_s$ , we need to determine the nominal value of each fit parameter in the unbinned likelihood function, as well as the uncertainties on each parameter. This includes the combinatorial background and the mass distribution shape since they are also in the p.d.f.

The nominal process is as follows. We first fit the shape of the  $D_s$  mass distribution alone. We then fix the fitted  $D_s$  mass shape, as well as fixing the  $B_s^0$  lifetime to the world average, vary the combinatorial background shape, and do the fit. After that,

Fit Parameter	Fit Result
$c\tau[\mu\text{m}]$	448 (fixed)
scale	$1.12^{+0.09}_{-0.08}$
$f_b$ [%]	$83.9^{+1.6}_{-1.7}$
$\lambda_+[\mu\text{m}]$	$656^{+48}_{-43}$
$\lambda_-[\mu\text{m}]$	$331^{+59}_{-44}$
$f_+$ [%]	$45.2^{+2.3}_{-2.3}$
$f_-$ [%]	$18.6^{+2.0}_{-2.0}$
$m_D$ [GeV]	1.9686 (fixed)
$\sigma_M$ [GeV]	$0.0084^{+0.0010}_{-0.0009}$
$\tau_M$ [GeV]	$0.5302^{+0.1507}_{-0.0959}$

Table 7.1:  $\phi\pi$  mode lifetime fit result with  $B_s^0$  lifetime fixed to world average.

we vary everything (except the  $B_s^0$  lifetime) and do a simultaneous fit.

As a cross check on our fitter, we also allow the  $B_s^0$  lifetime to vary in our fit and compare the result with previous measurements.

### 7.1.1 $\phi\pi$ Mode Lifetime Fit

For  $\phi\pi$  mode, after we get the combinatorial background shape, we vary every fit parameter except the  $B_s^0$  lifetime and the mass of the  $D_s$ , which are fixed to PDG[14] values, do a simultaneous fit both for the  $D_s$  mass shape and for the combinatorial background. Table 7.1 gives the results. These fitted parameter values will be the input for the later amplitude studies. The uncertainties of these fit parameters will be included in the systematic studies.

We also do a lifetime measurement by varying the  $B_s^0$  lifetime in the fit. Table

Table 7.2:  $\phi\pi$  mode lifetime fit result.

Fit Parameter	Fit Result
$c\tau[\mu\text{m}]$	$474^{+50}_{-45}$
scale	$1.12^{+0.09}_{-0.08}$
$f_b$ [%]	$84.0^{+1.6}_{-1.7}$
$\lambda_+[\mu\text{m}]$	$651^{+49}_{-43}$
$\lambda_-[\mu\text{m}]$	$331^{+58}_{-44}$
$f_+$ [%]	$45.2^{+2.4}_{-2.3}$
$f_-$ [%]	$18.6^{+2.0}_{-1.9}$
$m_D$ [GeV]	1.9686 (fixed)
$\sigma_M$ [GeV]	$0.0084^{+0.0010}_{-0.0009}$
$\tau_M$ [GeV]	$0.5273^{+0.1488}_{-0.0949}$

7.2 and Figure 7.1 show the results for the lifetime fit.

### 7.1.2 $K^{*0}K$ Mode Lifetime Fit

When we fit  $K^{*0}K$  mode lifetime, we have to include the  $B^0$  reflection term in the p.d.f. The proper decay time for the  $B^0$  reflection is similar to the  $B_s^0$  signal. We use the same K-factor histogram for  $B^0$  also.

$$F_{B^0}(x) = \frac{K}{c\tau_{B^0}} \exp\left(-\frac{Kx}{c\tau_{B^0}}\right) \otimes G(x, s \cdot \sigma) \otimes D(K). \quad (7.1)$$

The mass shape for the  $B^0$  reflection is the one we already discussed in chapter 4:

$$M_{B^0} = \begin{cases} c \operatorname{ERF}(\alpha(m - m_0)) \exp(\beta(m - m_0)) & \text{when } m > m_0 \\ c \operatorname{ERF}(\alpha(m - m_0)) & \text{when } m \leq m_0 \end{cases} \quad (7.2)$$

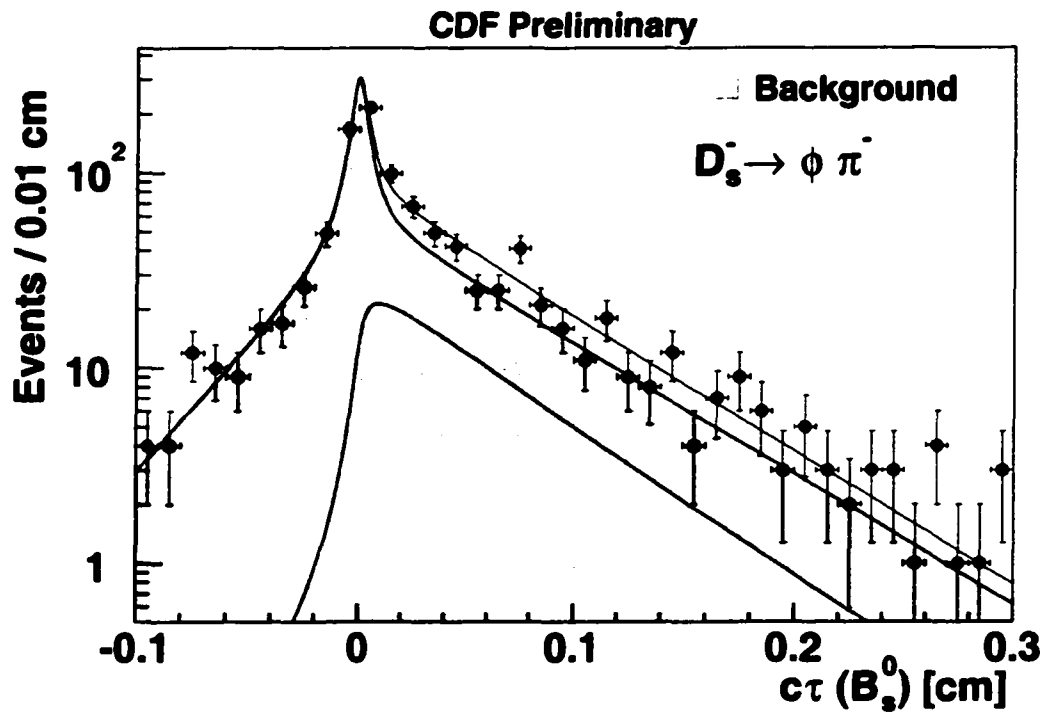


Figure 7.1:  $B_s^0 \phi\pi$  mode lifetime fit result with signal and background overlaid. The shaded area is the background and the lower curve is the signal. The fit yields  $B_s^0$  lifetime  $474^{+50}_{-45} \mu\text{m}$ .

Here  $m_0 = 1.9588$ ,  $\alpha = 51.46$ ,  $\beta = 0.06033$  and parameter  $c$  is a normalization constant. We integrate through the range 1.75-2.18 GeV to get the normalization constant. We define a new parameter  $f_{B^0}$  as number of  $B^0$  reflection events in the whole region, and we fix the shape of the  $B^0$  reflection during the lifetime fit. The total p.d.f. for  $K^{*0}K$  mode is

$$\mathcal{F} = (1 - f_b - f_{B^0})M_{sig}(m)F_{sig}(x) + f_b M_{bkg}(m)F_{bkg}(x) + f_{B^0} M_{B^0} F_{B^0}. \quad (7.3)$$

Note here

$$1 - f_b - f_{B^0} = \frac{1 - f_b}{1 + f_{b0}}$$

with the fit parameter  $f_{b0}$  defined as

$$f_{b0} = \frac{\text{Number of } B^0 \text{ events in whole region}}{\text{Number of } B_s^0 \text{ events in whole region}}.$$

Table 7.3 gives the fitted results when the  $B_s^0$  lifetime and the  $D_s$  mass are fixed to the PDG values.

Table 7.4 and Figure 7.2 show the fitted result when allowing the  $B_s^0$  lifetime to vary. The  $\phi\pi$  mode and  $K^{*0}K$  mode  $B_s^0$  lifetime fit results are  $c\tau(\phi\pi) = 474_{-45}^{+50}(\mu\text{m})$

Fit Parameter	Fit Result
$c\tau[\mu\text{m}]$	448 (fixed)
scale	$1.59^{+0.07}_{-0.07}$
$f_b$ [%]	$94.5^{+0.7}_{-1.0}$
$\lambda_+[\mu\text{m}]$	$526^{+20}_{-19}$
$\lambda_-[\mu\text{m}]$	$302^{+49}_{-37}$
$f_+$ [%]	$46.9^{+1.4}_{-1.4}$
$f_-$ [%]	$9.4^{+1.1}_{-1.1}$
$m_D$ [GeV]	1.9686 (fixed)
$\sigma_M$ [GeV]	$0.0119^{+0.0018}_{-0.0015}$
$\tau_M$ [GeV]	$0.7667^{+0.1088}_{-0.0854}$
$f_{b0}$ [%]	$0.0^{+25.2}_{-0.0}$

Table 7.3:  $K^{*0}K$  mode lifetime fit result with  $B_s^0$  lifetime fixed to world average.

and  $c\tau(K^{*0}K) = 397^{+65}_{-62}(\mu\text{m})$ , respectively, which agree well with the world average[5].

## 7.2 $B_s^0$ Amplitude Fit

### 7.2.1 The Sensitivity

The following equation is a theoretical estimate of the uncertainty on the amplitude for each given  $x = \Delta m/\Gamma$ :

$$\sigma_A = \sqrt{\frac{S+B}{S}} \frac{1}{\sqrt{\epsilon D^2}} \exp \frac{x^2 \sigma_t^2 \Gamma^2}{2} \sqrt{\frac{1+4x^2}{1+2x^2}} \frac{1}{\sqrt{S}} \quad (7.4)$$

where  $\Gamma$  is inverse of  $B_s$  lifetime,  $S$  is the number of signal events,  $B$  is the number of background events, and the time resolution  $\sigma_t$  depends on both decay length resolution

Table 7.4:  $K^{*0}K$  mode lifetime fit result.

Fit Parameter	Fit Result
$c\tau[\mu\text{m}]$	$397^{+65}_{-62}$
scale	$1.59^{+0.07}_{-0.07}$
$f_b$ [%]	$94.4^{+0.3}_{-1.0}$
$\lambda_+[\mu\text{m}]$	$531^{+22}_{-21}$
$\lambda_-[\mu\text{m}]$	$303^{+49}_{-37}$
$f_+$ [%]	$46.9^{+1.4}_{-1.5}$
$f_-$ [%]	$9.4^{+1.1}_{-1.1}$
$m_D$ [GeV]	1.9686 (fixed)
$\sigma_M$ [GeV]	$0.0119^{+0.0018}_{-0.0015}$
$\tau_M$ [GeV]	$0.7655^{+0.1085}_{-0.0854}$
$f_{b0}$ [%]	$0.0^{+25.4}_{-0.0}$

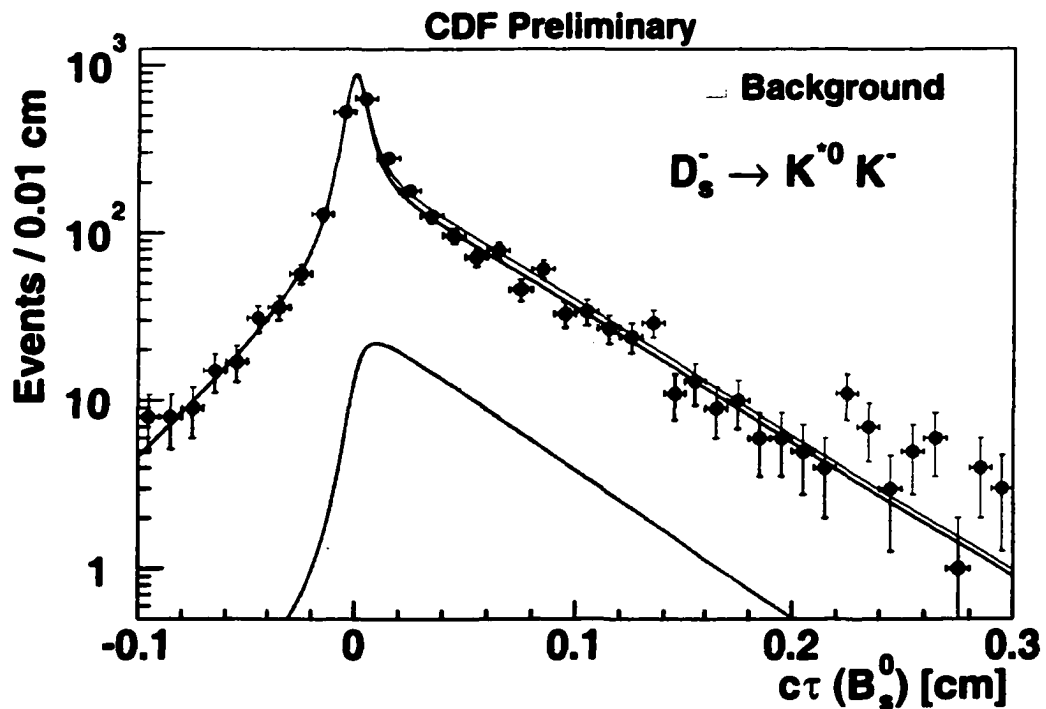


Figure 7.2:  $B_s^0$  lifetime fit result for  $K^{*0}K$  mode with signal and background overlaid. The shaded area is the background and the lower curve is the signal. The fit yields  $B_s^0$  lifetime of  $397^{+65}_{-62} \mu\text{m}$ .

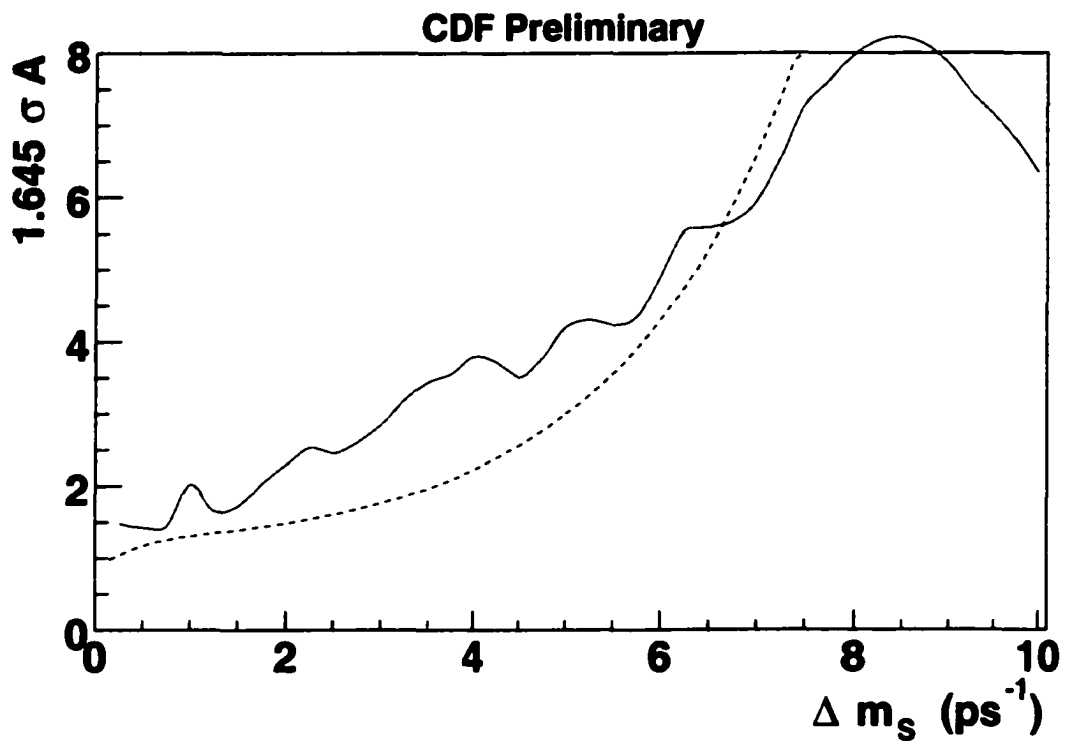


Figure 7.3: Estimate of the lower limit for  $\Delta m_s$  from study of  $\ell D_s$  channel at 95% confidence level. The dashed line is from the theoretical estimate of our data. The solid line is from the measurement of the amplitude scan.

and  $\beta\gamma$  resolution. The  $\beta\gamma$  term, or the  $K$  factor resolution term, depends on  $t$ , and it comes from the uncertainty of the  $B_s^0$  momentum since we can't fully reconstruct the  $B_s^0$  momentum.

$$\sigma_t^2 = \left(\frac{K\sigma_L}{c}\right)^2 + \left(\frac{\sigma_{Kt}}{K}\right)^2 \quad (7.5)$$

The sensitivity is defined as 1.645 times  $\sigma_A$  for 95% confidence level limit [6], that is, the average upper limit for many equivalent experiments. Figure 7.3 shows the theoretical estimated sensitivity versus  $\Delta m_s$  for our data and the measured sensitivity of our data versus  $\Delta m_s$ . Figure 7.4 shows the combined sensitivity estimate of the current measurement[6] and our data. From the plot we can see there is a  $0.2 \text{ ps}^{-1}$  increase of the combined sensitivity.

## 7.2.2 Amplitude Fit Result of $\phi\pi$ and $K^{*0}K$

Table 7.5 lists a few more input parameters for the amplitude fit for  $\phi\pi$  mode and  $K^{*0}K$  mode in addition to those fitted parameters from the lifetime fit. The  $B_s^0$  lifetime and  $D_s$  mass are set at the PDG value. We need also to obtain the value for the fit parameter  $f_{rs}$ , which is the fraction of right sign for the combinatorial background. We choose a  $D_s$  mass region far from signal and physics background, which ideally contains only background. For  $\phi\pi$  mode, we choose the  $D_s$  mass region 2.03 - 2.2 GeV. We choose the  $D_s$  mass region 1.75 - 1.93 GeV for  $K^{*0}K$  mode. We

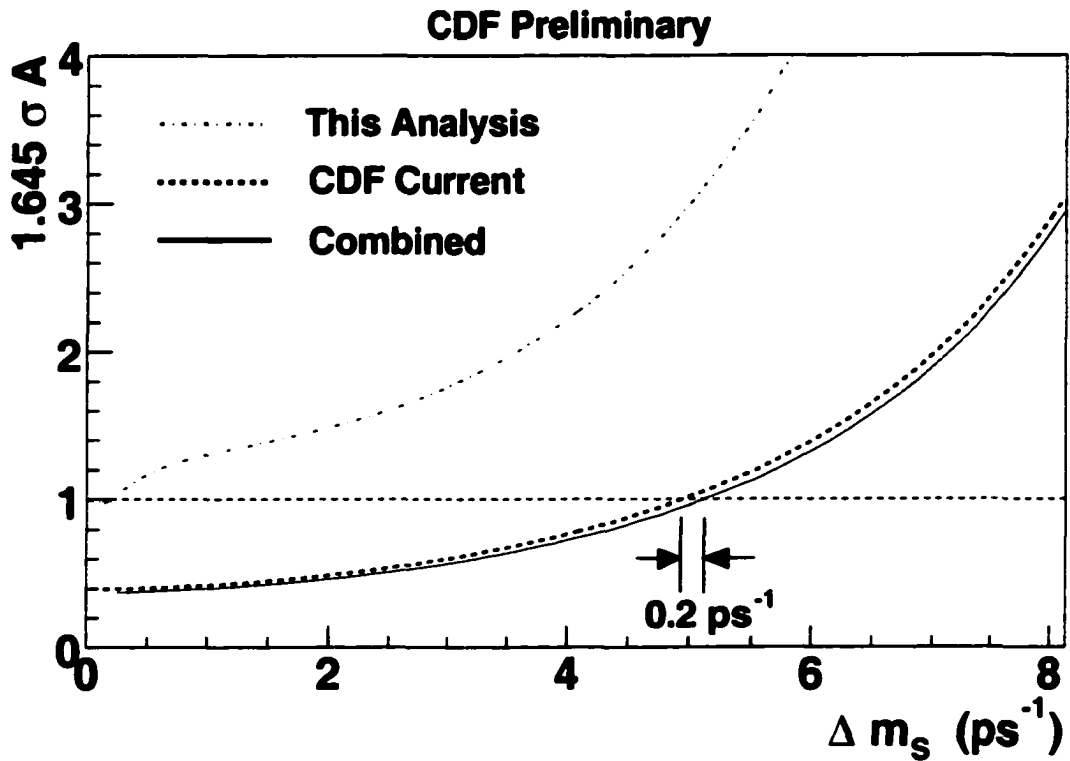


Figure 7.4: The combined theoretical estimate of the sensitivity of CDF current measurement and this analysis. The dot-dashed line is our estimated sensitivity. The dashed line is the estimated sensitivity of the current CDF measurement[35]. The solid line is the combined sensitivity estimate of these two measurements. The combined sensitivity is increased by  $0.2 \text{ ps}^{-1}$ .

Table 7.5:  $\phi\pi$  and  $K^{*0}K$  modes input parameters for the later amplitude fit

Input Parameter	Input Value
$c\tau[\text{um}]$	$448 \pm 19$
$m_D [\text{GeV}]$	$1.9686 \pm 0.0006$
$f_{rs}(\phi\pi) [\%]$	$53.3 \pm 2.6$
$f_{rs}(K^{*0}K) [\%]$	$49.2 \pm 1.5$

then find the number of tagged events  $N$  and number of right sign events  $N_r$  in this region. The parameter  $f_{rs}$  nominal value is  $N_r/N$ . The uncertainty on it is

$$\sigma_f = \sqrt{\frac{N_r(N - N_r)}{N^3}} \quad (7.6)$$

Those input parameter uncertainties of Table 7.5 together with the previous fitted parameter errors from the lifetime fit result are used in the systematics studies.

After we obtained the nominal values for all our fitting parameters for the two modes, we do an amplitude scan for both modes and combine the result together. Figure 7.5 is the combined amplitude scan for  $\phi\pi$  mode and  $K^{*0}K$  mode with all the tagging methods. Figure 7.6 is the current CDF's result[6]. Figure 7.7 is the combined result of CDF and ours where we assume no correlation of the systematic uncertainties between the measurements.

### 7.3 The Systematic Errors

For amplitude fit the systematic uncertainty is: (From reference [34])

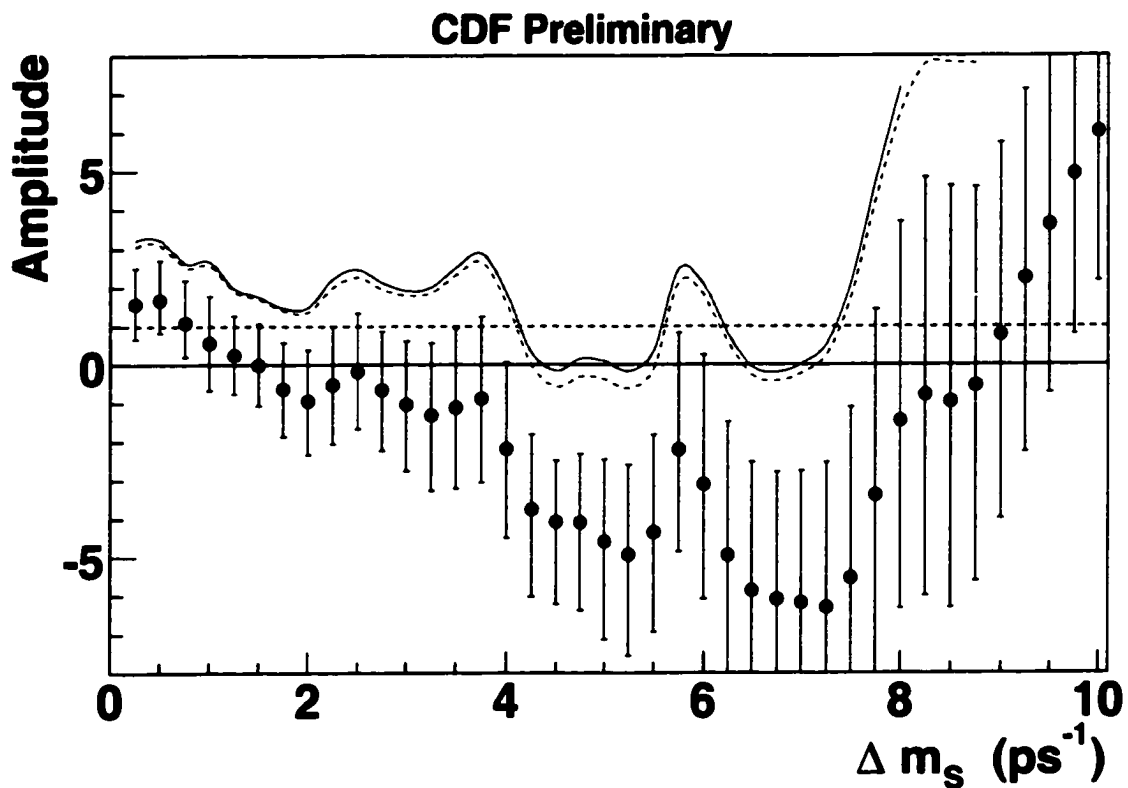


Figure 7.5:  $\phi\pi$  mode and  $K^{*0}K$  mode combined result of the amplitude scan. The dots with  $1\sigma$  error bars are fitted amplitudes with errors. The dashed line corresponds to  $A + 1.645\sigma_A$  with statistical uncertainties. The solid line is for statistical + systematic uncertainties.

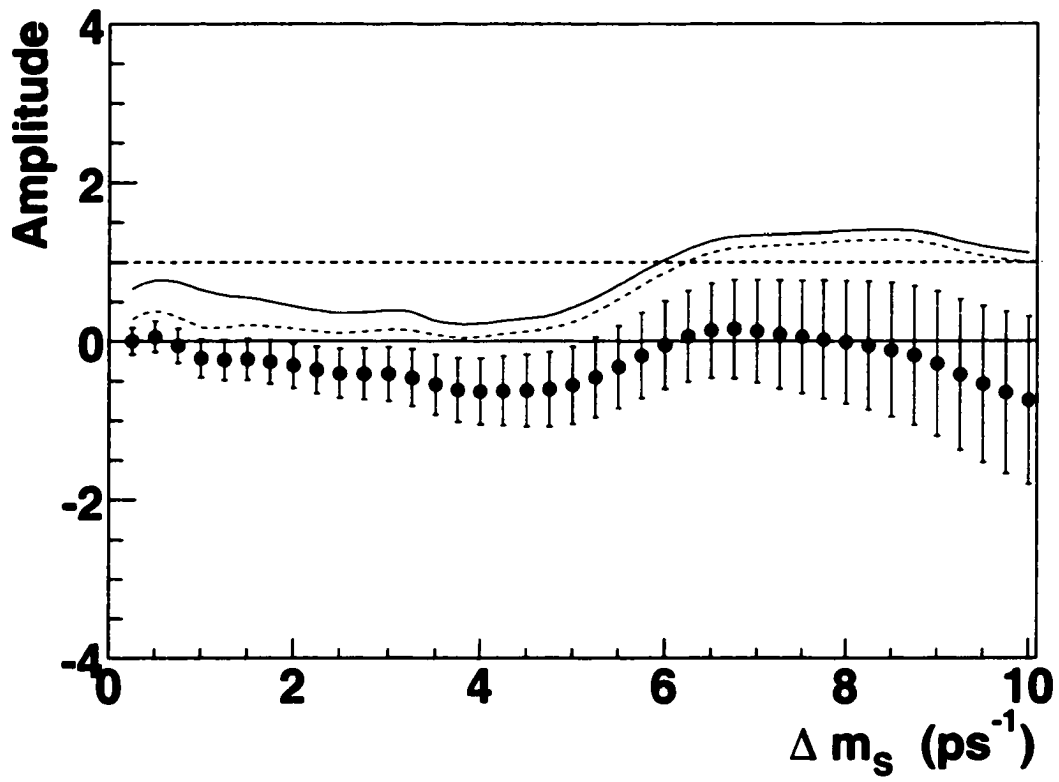


Figure 7.6: The CDF current result of  $B_s^0$  mixing amplitude scan. The values of  $\Delta m_s$  for which the solid line is less than one are excluded at 95% confidence level. The current CDF limit on  $\Delta m_s$  is  $5.8 \text{ ps}^{-1}$ .

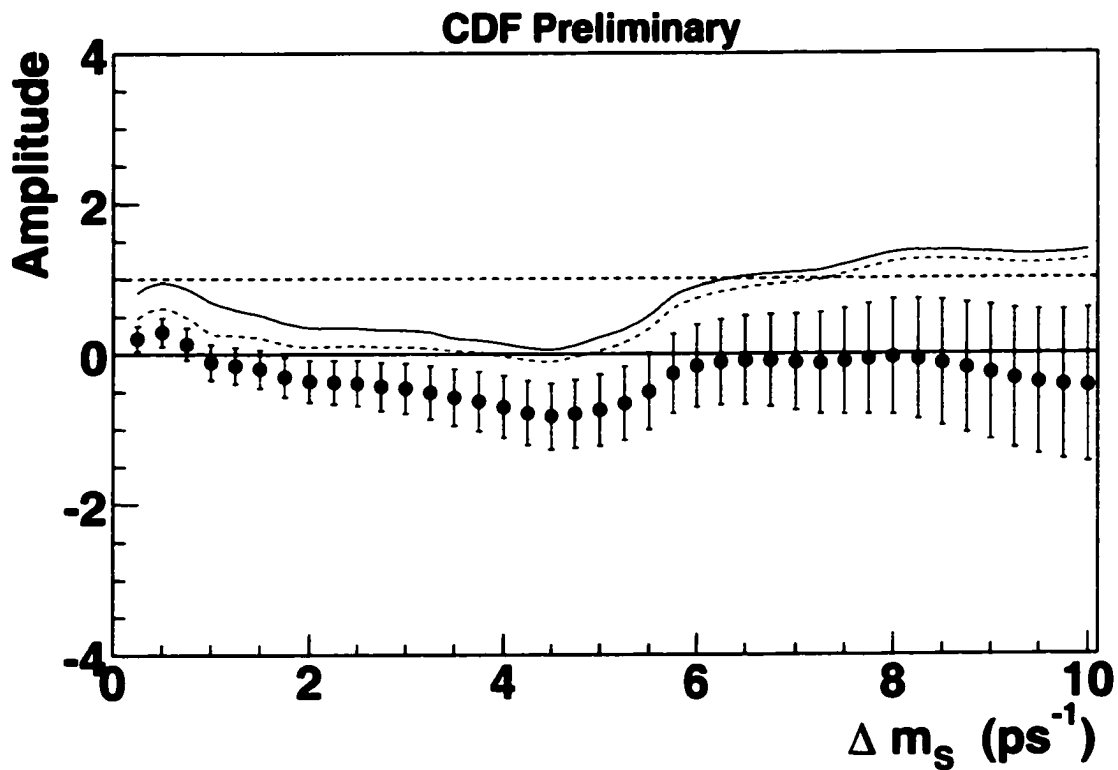


Figure 7.7: The combination of current CDF amplitude scan and ours assuming no correlation between the two analysis when combining the systematic uncertainties. The CDF preliminary new limit would be  $6.3 \text{ ps}^{-1}$ .

$$\sigma[A(\nu)]_{sys} = \Delta A(\nu) + (1 - A) \frac{\Delta\sigma(A)}{\sigma[A(\nu)]} \quad (7.7)$$

where  $\Delta A(\nu)$  and  $\Delta\sigma(A)$  are changes on amplitude and its uncertainty between the new fit and the fit using nominal parameter values. For systematic uncertainties due to fit parameters, we vary the fit parameter nominal value by  $\pm 1\sigma$  for that parameter and redo the amplitude scan. For other kinds of systematic uncertainties, we do the new amplitude scan under the new condition. Systematic uncertainties errors calculated this way correctly cover both the variations on the amplitude and variations on the amplitude uncertainty.

Sources of systematic errors we considered are uncertainties on fit parameters, such as dilution, fraction of right sign in sideband region,  $B_s^0$  lifetime (we are using the PDG value), resolution scale factor, fraction of background in the data region, shape of background ( $f_+, f_-, \tau_+, \tau_-$ ), etc. The other major systematic error sources come from the dilution parameterization which is already stated in Chapter 5. The total systematic uncertainties will be the sum in quadrature of all the systematic uncertainties obtained.

The systematic uncertainties are much smaller compare to the statistical uncertainties. Appendix A describes how we combine the uncertainties. When we merge the systematic uncertainties of our two modes, the dilution systematic uncertainties are 100% correlated. When we merge our results with current CDF results, we assume

**the dilution systematic uncertainties of the two are totally uncorrelated.**

# Chapter 8

## Conclusion

The current CDF  $B_s^0$  mixing frequency  $\Delta m_s$  limit is  $5.8 \text{ ps}^{-1}$ [6]. Combined with our measurement, the new CDF preliminary limit on  $\Delta m_s$  is

$$\Delta m_s > 6.3 \hbar \text{ ps}^{-1}$$

which is a 10% improvement though this measurement itself does not provide a limit measurement and the  $\ell D_s$  channel only has sensitivity at low  $\Delta m_s$  region. The world limit as of Fall, 2002, is  $13.1 \text{ ps}^{-1}$ .

This measurement uses  $91 \text{ pb}^{-1}$  of the inclusive  $e$  and  $\mu$  trigger data of the CDF Run I detector in  $p - \bar{p}$  collisions at  $\sqrt{s} = 1.8 \text{ TeV}$  and uses jet charge flavor tagging and soft lepton flavor tagging methods.

The CDF Run II experiment is expected to push the  $\Delta m_s$  limit to  $\sim 70 \text{ ps}^{-1}$  if

$\Delta m_s$  is above that value. Otherwise CDF in Run II is expected to measure it for the first time.

# Appendix A

## Combining Errors

In general we have two sets of measurement

$$x_1 = x_0 + \alpha_1 + \beta_1 + \gamma_1 + \dots$$

$$x_2 = x_0 + \alpha_2 + \beta_2 + \gamma_2 + \dots$$

Here  $x_0$  is the true value,  $x_1$  and  $x_2$  are the two measurements,  $\alpha$ ,  $\beta$ ,  $\gamma$ ,  $\dots$  are the different type of deviations from the true value. Note

$$\overline{\alpha_1} = 0$$

$$\overline{\alpha_1^2} = \sigma_{1a}^2$$

and  $\sigma_{1a}$  is the standard deviation. Similarly we have  $\sigma_{1b}^2, \sigma_{1c}^2, \dots$ .

We assume  $\sigma_{1a}$  and  $\sigma_{2a}$  are quadratic sum of all the uncorrelated errors of the measurement (including statistic errors and uncorrelated systematic errors),  $\sigma_{1b}$  and  $\sigma_{2b}$  are systematic errors correlated by efficiency  $f_b$ ,  $\sigma_{1c}$  and  $\sigma_{2c}$  are correlated by efficiency  $f_c, \dots$ . When  $f_b = 0$ ,  $\sigma_{1b}$  and  $\sigma_{2b}$  are actually totally uncorrelated, when  $f_b = \pm 1$ ,  $\sigma_{1b}$  and  $\sigma_{2b}$  are totally (anti)correlated. Thus

$$\begin{aligned}\sigma_1^2 &= \overline{(x_1 - x_0)^2} = \sigma_{1a}^2 + \sigma_{1b}^2 + \sigma_{1c}^2 + \dots \\ \sigma_2^2 &= \overline{(x_2 - x_0)^2} = \sigma_{2a}^2 + \sigma_{2b}^2 + \sigma_{2c}^2 + \dots \\ \sigma_{12} &= \overline{(x_1 - x_0)(x_2 - x_0)} = f_b \sigma_{1b} \sigma_{2b} + f_c \sigma_{1c} \sigma_{2c} + \dots\end{aligned}$$

Therefore the error matrix is

$$\begin{bmatrix} \sigma_{1a}^2 + \sigma_{1b}^2 + \sigma_{1c}^2 + \dots & f_b \sigma_{1b} \sigma_{2b} + f_c \sigma_{1c} \sigma_{2c} + \dots \\ f_b \sigma_{1b} \sigma_{2b} + f_c \sigma_{1c} \sigma_{2c} + \dots & \sigma_{2a}^2 + \sigma_{2b}^2 + \sigma_{2c}^2 + \dots \end{bmatrix} \equiv \begin{bmatrix} \sigma_1^2 & \sigma_{12} \\ \sigma_{12} & \sigma_2^2 \end{bmatrix} \equiv \sigma^2$$

The covariance matrix is then

$$V \equiv (\sigma^2)^{-1} = \frac{1}{\det \sigma^2} \begin{bmatrix} \sigma_2^2 & -\sigma_{12} \\ -\sigma_{12} & \sigma_1^2 \end{bmatrix} \equiv \begin{bmatrix} V_{11} & V_{12} \\ V_{12} & V_{22} \end{bmatrix}$$

Thus we have

$$\chi^2 = \sum_{i,j} (x_i - x)(x_j - x)V_{ij}$$

Minimizing  $\chi^2$  gives

$$\begin{aligned} x &= \frac{(V_{11} + V_{12})x_1 + (V_{22} + V_{12})x_2}{V_{11} + V_{22} + 2V_{12}} \\ &= \frac{(\sigma_2^2 - \sigma_{12})x_1 + (\sigma_1^2 - \sigma_{12})x_2}{\sigma_1^2 + \sigma_2^2 - 2\sigma_{12}} \\ \sigma_x^2 &= \left(\frac{\partial x}{\partial x_1}\right)^2 \sigma_1^2 + \left(\frac{\partial x}{\partial x_2}\right)^2 \sigma_2^2 + 2\frac{\partial x}{\partial x_1} \frac{\partial x}{\partial x_2} \sigma_{12} \\ &= \frac{\sigma_1^2 \sigma_2^2 - \sigma_{12}^2}{\sigma_1^2 + \sigma_2^2 - 2\sigma_{12}} \end{aligned}$$

We can rewrite the above two equations as follow:

$$\begin{aligned} \frac{1}{\sigma_x^2 - \sigma_{12}} &= \frac{1}{\sigma_1^2 - \sigma_{12}} + \frac{1}{\sigma_2^2 - \sigma_{12}} \\ x &= \left( \frac{x_1}{\sigma_1^2 - \sigma_{12}} + \frac{x_2}{\sigma_2^2 - \sigma_{12}} \right) (\sigma_x^2 - \sigma_{12}) \end{aligned}$$

From these two equations we can easily see when  $\sigma_{12} = 0$ , the results are reduced to the standard formulas for merging two uncorrelated errors.

# Bibliography

- [1] N. Cabibbo, Phys. Rev. Lett., **10**, 531 (1963).
- [2] M. Kobayashi and T. Maskawa, Progr. Theor. Phys. **49**, 652 (1973).
- [3] Michael Gronau, *CP violation in the standard model: The B meson system*, Proceedings of the workshop on B Physics at Hadron Accelerators, page 1.
- [4] Isard Dunietz, *Extracting CKM parameters from B decays*, Proceedings of the workshop on B Physics at Hadron Accelerators, Snowmass, Colorado, eds. P. McBride and C. Shekhar Mishra, Fermilab-CONF93/267 (Batavia, 1993), page 83.
- [5] K. Hagiwara *et al.*, Physical Review D**66**, 010001 (2002)
- [6] F. Abe *et al.* Phys. Rev. Lett. **82**, 3576 (1999).
- [7] Donald H. Perkins, Intro. to High Energy Physics.
- [8] M. Gell-Mann, Phys. Lett **8**, 214 (1964).

- [9] S.L. Glashow, J. Iliopoulos and L. Maiani, Phys. Rev. **D2**, 1585 (1970).
- [10] L. Wolfenstein, Phys. Rev. Lett., **51**, 1945 (1983).
- [11] A.J. Buras *et al.* Nucl. Phys. **B245**, 369 (1984).
- [12] T. Inami and C.S. Lim, Prog. Theor. Phys. **65**, 297 (1981)
- [13] A. J. Buras, Proceedings of 'Beauty 95', Oxford, England, July 1995, Nucl. Instrum. Meth. A **368**, 1 (1995)
- [14] D.E. Groom *et al.*, The European Physical Journal **C15**, 1 (2000)
- [15] A. J. Buras, Nucl. Phys. B **347**, 491 (1990).
- [16] C. Bernard, Nucl. Phys. Proc. Suppl. **94**, 159 (2001)
- [17] A. J. Buras, Plenary talk at ICHEP96, July 1996, **hep-ph/9610461**.
- [18] A. J. Buras and M. Lindner, "Heavy flavors", *Singapore: World Scientific (1992)*  
*785 p. (Advanced series on directions in high energy physics, 10)*.
- [19] F. Abe *et al.*, Nucl. Instrum. Methods Phys. res. **A 271**, 387 (1998).
- [20] K. Burkett and M. Paulini, CDF Internal note 4239.
- [21] O. Long, Thesis, Univ. of Pennsylvania..
- [22] O. Long *et al.*, CDF Internal note 3810 page 22.

- [23] F. Abe *et al.* **PRD50**, No 5, Sept. 1994.
- [24] R. Akers D. Buskulic *et al.* **Phys. Lett. B 327**, 411 (1994).
- [25] D. Buskulic *et al.* **Phys. Lett. B 356**, 409 (1995).
- [26] K. Abe *et al.* **Phys. Rev. Lett. 74**, 2890 (1995).
- [27] P. Abreu *et al.* **Zeit. Phys. C 72**, 17 (1996).
- [28] D. Buskulic *et al.* **Zeit. Phys. C 75**, 397 (1997).
- [29] H. U. Bengtsson & T. Sjöstrand, **Computer Physics Commun. 43**, 43 (1987);  
T. Sjöstrand, **Computer Physics Commun. 82**, 74 (1994);
- [30] Paul Avery, Ken Read, Garry Trahern, *QQ:A Monte Carlo Generator*, CLEO  
Software Note CSN-212, March 25, 1985.
- [31] D. Kestenbaum, Thesis, Harvard University (1996).
- [32] P. Sphicas, CDF Internal note 2655
- [33] R. Brun and F. Rademakers, *ROOT - An Object Oriented Data Analysis Framework*, Proceedings AIHENP'96 Workshop, Lausanne, Sep. 1996, **Nucl. Inst. & Meth. in Phys. Res. A 389** (1997) 81-86. See also <http://root.cern.ch/>.
- [34] H. Moser and A. Roussaire, **Nucl. Instrum. and Meth. A 384**, 491 (1997)
- [35] F. Bedeschi *et al.* CDF Internal note 4712



## 2017 ProQuest Distribution Agreement

This Agreement is between the author (Author) and ProQuest LLC, through its ProQuest Dissertation Distribution business (formerly ProQuest/UMI). Under this Agreement, Author grants ProQuest certain rights to preserve, archive and distribute the dissertation or thesis (the Work), abstract, and index terms provided by Author to ProQuest.

### Section I. License for Inclusion of the Work in ProQuest Publishing Program

**Grant of Rights.** Author hereby grants to ProQuest the **non-exclusive**, worldwide right to reproduce, distribute, display and transmit the Work (in whole or in part) in such tangible and electronic formats as may be in existence now or developed in the future. Author further grants to ProQuest the right to include the abstract, bibliography and other metadata in the ProQuest Dissertations & Theses database (PQDT) and in ProQuest Dissertation Abstracts International and any successor or related index and/or finding products or services.

**ProQuest Publishing Program - Election and Elements.** The rights granted above shall be exercised according to the publishing option selected by Author in Section III, Author Options, and subject to the following additional Publishing Program requirements:

- **Distribution of the Work.** Except as restricted by Author in the publishing option selected, the rights granted by Author automatically include (1) the right to allow sale and distribution of the Work, in whole or in part, by ProQuest and its sales agents and distributors and (2) the right to make the Abstract, bibliographic data and any meta data associated with the Work available to search engines and harvesters.
- **Restrictions.** ProQuest will use commercially reasonable efforts to restrict the distribution of the Work as provided under the publishing option selected by Author or *as later elected by Author* through direct contact with ProQuest. Such election is subject to Author's Degree Granting Institution Directives. With respect to restrictions requested after submission of the Work, Author acknowledges that ProQuest cannot recall or amend previously distributed versions of the Work.
- **Removal of Work from the Program.** ProQuest may elect not to distribute the Work if it believes that all necessary rights of third parties have not been secured. Refer to the website [http://www.proquest.com/products\\_umi/dissertations/](http://www.proquest.com/products_umi/dissertations/) for information about copyright and your dissertation or thesis. If Author's degree is rescinded, and/or the degree-granting institution so directs, ProQuest will expunge the Work from its publishing program in accordance with its then current publishing policies.
- **Degree Granting Institution Directives.** Author is solely responsible for any conflict between policies and directions of Author's degree-granting institution, Author's choice of publishing model, and/or any restriction Author places on the use of the Work. For the avoidance of doubt, ProQuest is not responsible for access to the Work that is provided by Author's degree-granting institution through its library or institutional repository. Author must work directly with Author's degree granting institution to ensure application of any restrictions to access relating to the Work by Author's degree granting institution.

**Delivery of the Work.** Author shall provide to ProQuest the Work and all necessary supporting documents during the online submission process, according to the Instructions accompanying this agreement.

**Rights Verification.** Author represents and warrants that Author is the copyright holder of the Work and has obtained all necessary rights to permit ProQuest to reproduce and distribute third party materials contained in any part of the Work, including all necessary licenses for any non-public, third party software necessary to access, display, and run or print the Work. Author is solely responsible and will indemnify ProQuest for any third party claims related to the Work as submitted for publication.

#### Open Access Publishing Plus

- I want the broadest possible dissemination of my work, and I want to provide free global access to the electronic copy of my work via the internet.
- I understand that I will not be eligible to receive royalties.

Formatted: Indent: Left: 0.69", First line: 0.07", Bulleted + Level: 1 + Aligned at: 0.69" + Indent at: 0.78"

I want major search engines (e.g. Google, Yahoo) to discover my work. Learn more: <http://www.proquest.com/en-US/products/dissertations/google.shtml>

- Yes
- No

Formatted: Indent: Left: 0.75", Bulleted + Level: 2 + Aligned at: 0.81" + Indent at: 1.06"

Acknowledgment: I have read, understand and agree to this ProQuest Publishing Agreement, including all rights and restrictions included within the publishing option chosen by me as indicated above

REQUIRED Author's signature

Date 7/26/17

(Print Name)

HONGQUAN Niu

Institution conferring degree

Brandeis's Univ.

This page must accompany your manuscript and the rest of the submission materials

Please check type of manuscript:

M (Master's Thesis)

D (Dissertation)

### Dissertation/Master's Thesis Submission Form

Please print clearly in block letters

#### Personal Information

Last Name NIU Middle Name or Initial \_\_\_\_\_  
First Name HONGQUAN Country (ies) of Citizenship P.R.China

#### Degree & Dissertation Information

Title of Dissertation/ Thesis Limit on the  $B_s^0 \bar{B}_s^0$  Oscillation Freq.  
Institution conferring degree Brandeis Univ. Degree awarded (abbreviate; e.g., Ph.D.) Ph.D.  
College, School, or Division \_\_\_\_\_ Year degree awarded 2003  
Department or Program Dept. of Physics Year manuscript completed \_\_\_\_\_  
Advisor/Committee Chair Craig Blocker  
Committee Member Lawrence Kirsch Committee Member \_\_\_\_\_  
Committee Member George Brandenburg Committee Member \_\_\_\_\_

Committee Member \_\_\_\_\_ Committee Member \_\_\_\_\_

Language of manuscript English

Primary Subject Category: Enter the 4-digit code and category name from the Subject Category Guide that most closely describes the area of your research.

Code 0798 Category Particle Physics

You may suggest two additional subject categories that may aid in the discovery of your work in our digital database.

Code \_\_\_\_\_ Category \_\_\_\_\_ Code \_\_\_\_\_ Category \_\_\_\_\_

Provide up to 6 keywords or short phrases for citation indices, library cataloging, and database searching.

**Current Contact Information**

Current Email Address hankni@partners.org

Street Address 39 Smith St.

*Please provide your postal address if you are interested in receiving royalties on sales of your thesis.*

City Marblehead Province MA Daytime Phone 781-248-6485

Country USA Postal Code 01945 Evening Phone \_\_\_\_\_

**Permanent Contact Information**

Permanent Email Address hankni@email.com

Street Address (line 1) same

City \_\_\_\_\_ Province \_\_\_\_\_ Future Phone \_\_\_\_\_

Country \_\_\_\_\_ Postal Code \_\_\_\_\_ Alternate Future Phone \_\_\_\_\_

**THIS PAGE MUST ACCOMPANY YOUR MANUSCRIPT AND THE REST OF YOUR SUBMISSION MATERIALS**

**Subject Categories**

The ProQuest Dissertations & Theses (PQDT) database and the ProQuest citation indices are arranged by subject categories. Please select the one category below that best describes your field of research or creative work. You may add one or two additional categories on your submission form that will also be associated with your work as secondary subjects.

**Arts, Business, Education, Humanities, and Social Sciences**

**AREA, ETHNIC, AND GENDER STUDIES**

African American studies	0296
African studies	0293
American studies	0323
Asian American studies	0343
Asian studies	0342
Baltic studies	0361
Black studies	0325
Canadian studies	0385
Caribbean studies	0432
Classical studies	0434
East European studies	0437
Ethnic studies	0631
European studies	0440
French Canadian culture	0482
Gender studies	0733
GLBT studies	0492
Hispanic American studies	0737

Holocaust studies	0507
Islamic culture	0512
Judaic studies	0751
Latin American studies	0550
Middle Eastern studies	0555
Native American studies	0740
Near Eastern studies	0559
North African studies	0560
Pacific Rim studies	0561
Regional studies	0604
Scandinavian studies	0613
Slavic studies	0614
South African studies	0654
South Asian studies	0638
Sub Saharan Africa studies	0639
Women's studies	0453

**BUSINESS**

Accounting	0272
Arts management	0424
Banking	0770
Business	0310
Entrepreneurship	0429
Finance	0508
Management	0454
Marketing	0338
Sports management	0430

**COMMUNICATIONS AND INFORMATION SCIENCES**

Communication	0459
Information science	0723
Journalism	0391
Library science	0399
Mass communication	0708
Technical communication	0643